AN ABSTRACT OF THE THESIS OF

Susan L. Howard for the degree of Master of Science in Oceanography presented on October 14, 1997. Title: Tide-Related Mixing in the Eastern Arctic Ocean.

Redacted for privacy

Abstract approved: _____ _____

Laurence Padman

Several recent studies support the hypothesis that mixing associated with tidal currents plays an important role in affecting the mean circulation and hydrographic properties over the continental shelves and slope of the eastern Arctic Ocean [*Polyakov*, 1995; *Parsons*, 1995]. Tidal currents increase mixing in the ocean by increasing stress at both the seabed and the ice-ocean interface, and by the generation of internal tides. This study uses a combination of model output and observational data to examine the spatial distribution of tidal mixing in this region, and establish the need to include or parameterize this process in basin scale general circulation models.

The major fluxes of heat and salt into the Arctic Ocean occur through horizontal advection in the eastern Arctic, where Atlantic Water first enters the Arctic Basin. The eastern Arctic is also a region of strong tides, shallow water, seasonally-varying ice cover, and steep topography. This region was therefore chosen as the area of focus due to the potential for tidal-related mixing to significantly modify the fate of the incoming transports of heat and salt.

First, the Simpson-Hunter parameter, calculated from output from the barotropic tidal model of *Kowalik and Proshutinsky* [1994], is used to determine the spatial variations in the effectiveness of tidal currents to mix the water column through boundary stresses. The northern Barents shelf break is a region of strong stress-driven

tidal mixing, stronger even than mixing on the broad shallow shelf. The next part of this study applies the analytical models of *Sjöberg and Stigebrandt* [1992] and *Baines* [1982] to output from the same barotropic tidal model to examine the spatial variability of internal tide generation and the associated mixing. Estimated energy fluxes from the barotropic S_2 and M_2 tides into internal tides of 5×10^{-4} W m^{-2} (with rotation) and 1×10^{-2} W m^{-2} (without rotation) are common along the upper slopes of the Northern Barents Sea and Yermak Plateau. The baroclinic model of *Parsons* [1995] is also used to examine the spatial distribution of internal tides. In the model, strong bottom-generated internal waves at the M_2 tidal frequency exist on the northern Barents shelf break region. Models are consistent with the few observations of internal tides in this region.

Diffusivities and heat fluxes were estimated from both the analytical models and Parsons' numerical model. The models show large variations in diffusivities across the shelf break region and are in qualitative agreement with observations. In a simple modeling exercise, geostrophic velocities of 8 cm s^{-1} can be created as a result of typical variations in vertical diffusivities across the slope. From observations, the typical mean flow along the northern Barents shelf break region is about 10 cm s^{-1}. The *Häkkinen and Mellor* [1992] model, which does not include tides, produces only ~1-2 cm s^{-1} currents along the shelf break region, i.e. it is unable to reproduce the strong boundary current seen in observations. Energy flux calculations show that tidal mixing provides a vertical heat flux of ~ 10 Wm^{-2}, enough to melt 0.35 cm per day of ice.

TIDE-RELATED MIXING IN THE EASTERN ARCTIC OCEAN

by

Susan L. Howard

A THESIS

submitted to

Oregon State University

in partial fulfillment of
the requirements for the
degree of

Master of Science

Presented October 14, 1997
Commencement June 1998

Master of Science thesis of Susan L. Howard presented on October 14, 1997

APPROVED:

Redacted for privacy

Major Professor, representing Oceanography

Redacted for privacy

Dean of College of Oceanic and Atmospheric Sciences

Redacted for privacy

Dean of Graduate School

I understand that my thesis will become part of the permanent collection of Oregon State University libraries. My signature below authorizes release of my thesis to any reader upon request.

Redacted for privacy

Susan L. Howard, Author

ACKNOWLEDGEMENTS

This research was made possible by the generosity of researchers who contributed model output and data sets. I would like to thank NSIDC for providing satellite data, A. Parsons and W. Maslowski for providing model output, Z. Kowalik and A. Proshutinsky for also making their model output available, and A. Plueddemann for providing observational data.

I would also like to thank the many people who supported me over the past four years. First, and foremost, I would like to thank my advisor, Laurie Padman, for his constant support, encouragement, and guidance. I am indebted to Murray Levine for providing feedback on my thesis as well as serving on my committee. I would also like to thank my friends, classmates, and officemates who made life enjoyable. Finally, I would like to thank my parents for their loving support.

Funding for this study was provided by the National Aeronautics and Space Administration Space Grant Fellowship and the Office of Naval Research ASSERT award programs.

TABLE OF CONTENTS

TABLE OF CONTENTS (continued)

LIST OF FIGURES

LIST OF FIGURES (Continued)

LIST OF FIGURES (Continued)

LIST OF FIGURES (Continued)

LIST OF TABLES

TIDE-RELATED MIXING IN THE EASTERN ARCTIC OCEAN

1. INTRODUCTION

Recent interest in Arctic oceanography has been driven by two principal factors: increased awareness of the Arctic's role in global climate variability; and concern over the dispersal of radionuclide contaminants released in the northern Russian shelf seas. In order to understand these aspects of the Arctic Ocean, scientists have used both *in situ* studies and numerical modeling. Despite the new observational programs, however, data remains sparse over much of this region, leading to a reliance on the models to provide an overall picture of the structure and circulation of the Arctic Ocean.

The effectiveness of numerical models depends on both the inclusion of all relevant physics, and the model's ability to resolve the space and time scales of important processes. Computational limitations require that, rather than explicitly trying modeling all important processes, some processes be modeled by simple parameterizations or even be ignored. Determining how to best parameterize significant processes that are presently excluded from models is, therefore, a necessary step towards improving our ability to understand the Arctic and its connection to the global ocean.

Tide-related mixing is often neglected or poorly parameterized in models. Until recently, tides were often neglected from large-scale Arctic general circulation models. However, the few small-scale process studies that have been made in the eastern Arctic Ocean [*Padman and Dillon*, 1991; *Plueddemann*, 1992; *D'Asaro and Morison,* 1992] strongly suggest that tides play an important role in altering water mass properties, ocean heat fluxes, and ice dynamics and thermodynamics in the region. These process studies have demonstrated a relationship between tidal currents and strong mixing events, which have been shown to increase diapycnal heat fluxes. However, the data were very limited in spatial extent, focusing on the Yermak Plateau. Not much is known about the potential for tides to affect water mass properties in other parts of the eastern Arctic Ocean, even

though the major entry for heat and salt into the Arctic occurs along the northern edge of the Barents Sea and across the sea itself.

The sparseness of the data prevents a spatial estimation of the general influence of tides in this region solely through observations. Therefore, this study examines the spatial extent of tidal mixing through the use of models. Both analytical models and output from numerical models will be used to establish the significance of tides in the eastern Arctic. We acknowledge the limitations of the models but maintain their importance as the only way at present to examine tidal mixing over regions critical to the Arctic heat budget. The realism of the models will be evaluated by comparing their output to observations in selected areas. The purpose of this study is not to get exact values, but to get a general picture of the spatial variability and magnitude of tide-induced mixing and to investigate how this mixing might affect the Arctic environment.

In the following section, the physical and hydrographical setting of the eastern Arctic Ocean is described. A general description of tidal mixing and the development of analytical methods for estimating it is then given. Section 3 describes the data sets used in this study. The results of this study are given in Section 4. In section 5, a comparison of the model results versus observational data is given, as well as a discussion of the effect of tidal mixing on heat fluxes, sea ice, and circulation. Conclusions are given in section 6.

2. BACKGROUND

2.1 Overview of the Hydrography, Ice Cover, and Currents in the Eastern Arctic Ocean

2.1.1 *Circulation*

The major flux of heat and salt into the Arctic Ocean occurs in the eastern Arctic where the relatively warm and salty Atlantic Water (AW) first enters the Arctic Basin [*Aagaard and Greisman*, 1975]. Due to the shallow and complex topography of the Kara and Barents Seas (figure 2.1), AW has the potential of being significantly modified by mixing processes that we predict will be energetic in these regions. The topography of this region is important for both its ability to steer AW and its role in establishing the oceanic conditions that lead to the generation of turbulence.

Northward-flowing AW bifurcates south of Bear Island and enters the Arctic Ocean via the Fram Strait branch and the Barents Sea branch (figure 2.2). The two branches, which each supply about 2 Sv of water to the Arctic Ocean [*Rudels et al.*, 1994], must cross either the Barents and Kara Seas (Barents Sea branch) or flow along the Northern Barents Sea shelf break (Fram Strait branch). Each branch is modified according to the processes it encounters along its path.

As the AW flows along both branches, it meets southward flowing, ice-bearing surface waters, part of the Transpolar Drift (figure 2.3). The AW cools slightly due to both atmospheric fluxes and interaction with sea ice, but retains much of its salt and heat properties. As it cools, it sinks below the cold, fresh surface waters to a depth of 100-200 m, and continues on its path as Atlantic Intermediate Water (AIW). In the Barents Sea, the Polar Sea Front represents the confluence of the cold, southward-flowing water and warm, northward-flowing water. Guided by the troughs and banks of the Barents Sea [*Pfirman et al.*, 1994], Barents Sea-derived AIW enters the Kara Sea between Novaya Zemlya and Franz Josef Land where it then flows down the St. Anna Trough and into the

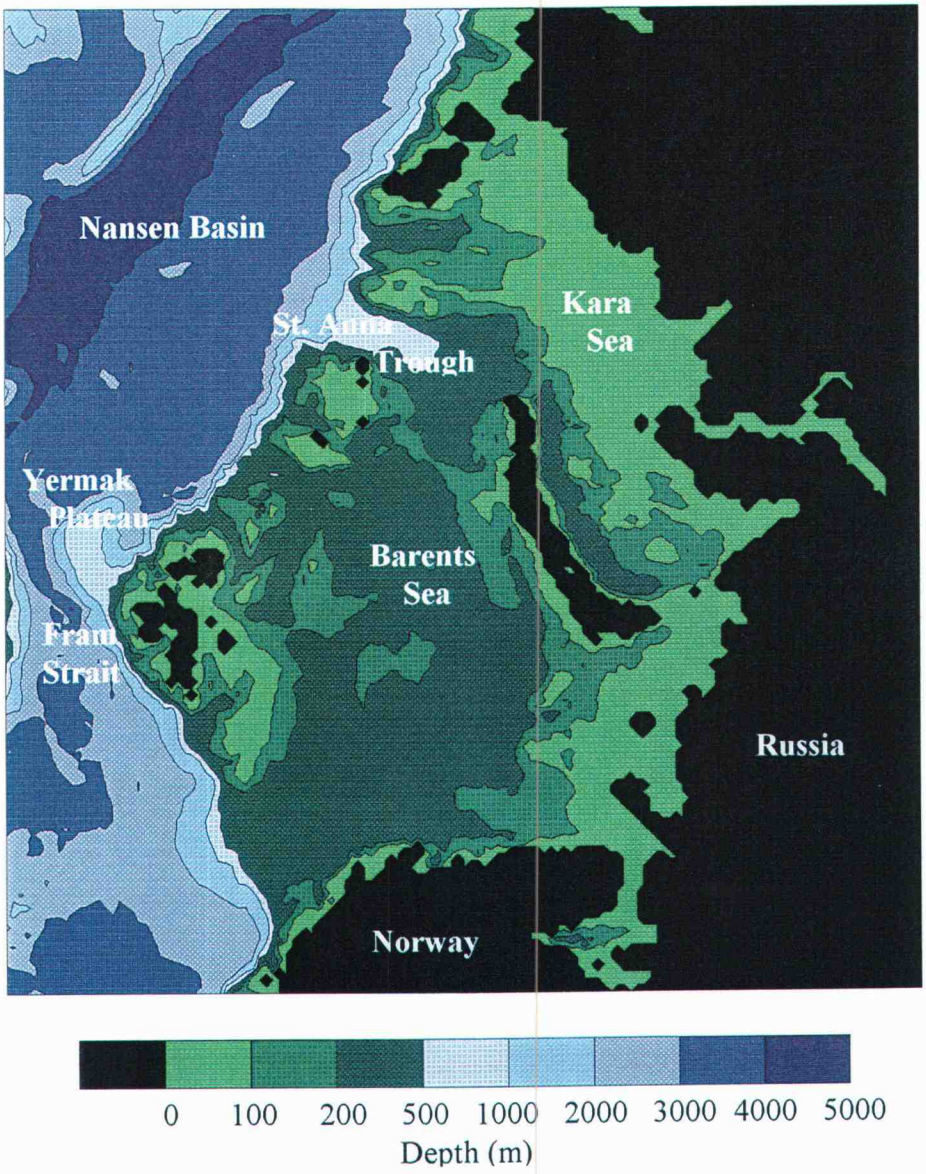

Figure 2.1. A bathymetric map of the eastern Arctic Ocean.

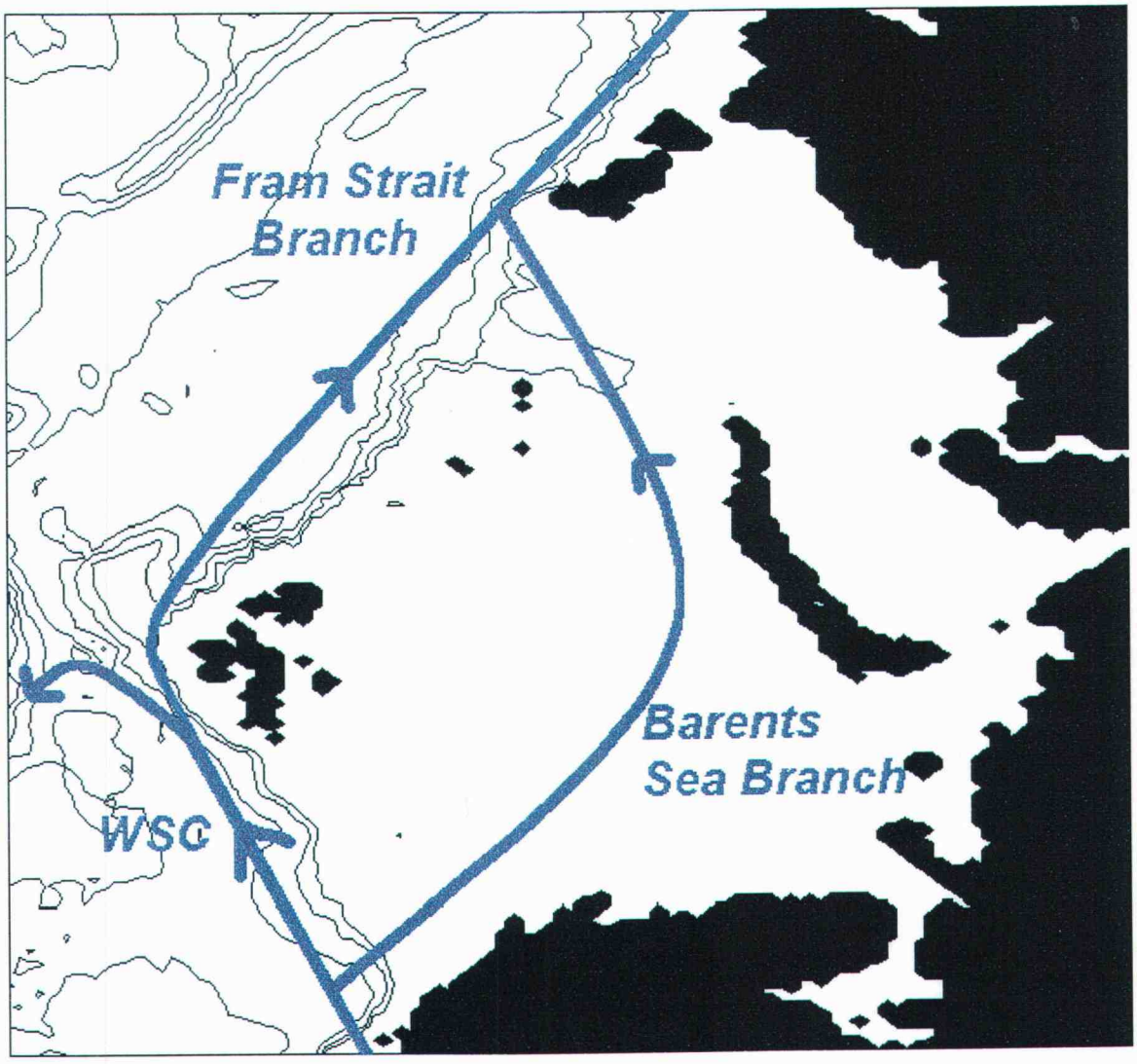

Figure 2.2. A map of the Eastern Arctic Ocean. The main pathways of Atlantic Water are illustrated by the blue arrows (after *Rudels et al.* [1994]).

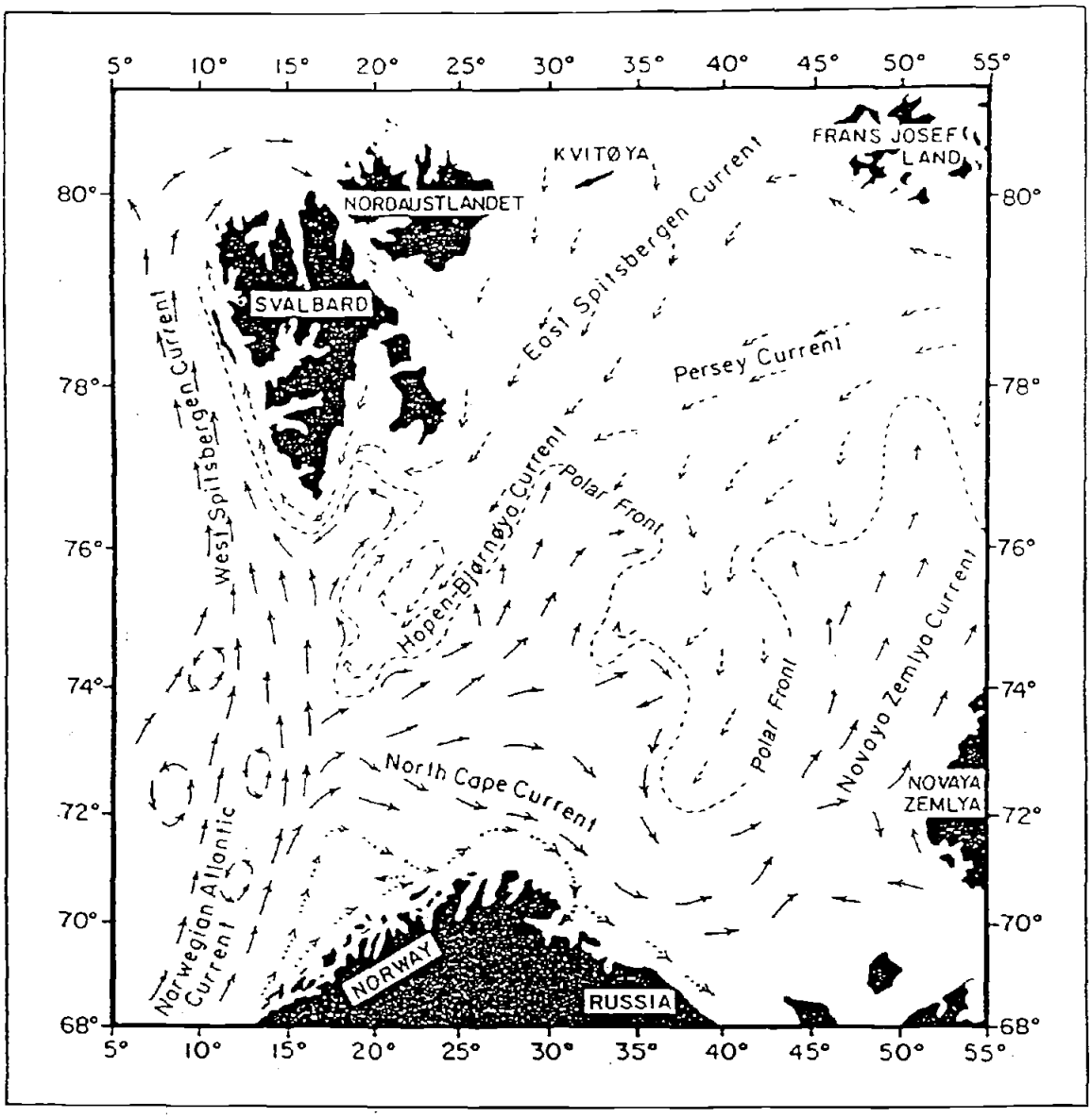

Figure 2.3 The surface circulation in the Barents Sea. Dashed arrows indicate cold currents (Arctic water); solid arrows indicate warm currents(Atlantic water). The dashed line indicates the position of the Polar Front (from *Pfirman et al.* [1994], after *Tantsiura* [1959]; *Novitsky* [1961]; and *Midttun and Loeng* [1987]).

Arctic Ocean [*Rudels et al.*, 1994]. Along this path, the shallow, variable topography in the Kara and Barents Seas provides many opportunities for the generation of turbulence. The water depth in these seas is generally less than 500 m (with the exception of the St. Anna Trough) and often less than 200 m. In the shallowest regions, sea-bed and sea-surface turbulent (or frictional) boundary layers may extend far enough to encompass the entire water column.

The Fram Strait branch, originating as the West Spitsbergen Current (WSC), loses its surface AW signal around 79° N [*Manley*, 1995]. Near Fram Strait, the northward flowing AW/AIW again splits into several branches, controlled by topography [*Manley*, 1995; *Gascard et al.*, 1995; *Muench et al.*, 1992]. The Svalbard Branch depicted in figure 2.2 is the primary pathway by which AW carried by the WSC enters the Arctic Ocean. As both branches (Fram and Barents) reach the slope of the northern Barents and Kara Seas, the warm (AIW) has a temperature of about 1°C and a salinity of 35 psu. A typical profile for this region is shown in figure 2.4. AIW represents a huge potential heat reservoir for the Arctic Ocean. As indicated in figure 2.4, the cold halocline lies between the warm Atlantic Layer water and the cold surface layer. Cold, weakly-stratified Arctic Deep Water resides beneath the Atlantic Layer and extends down to the sea bed.

Not only are the Kara and Barents Seas an important area for incoming heat and salt fluxes, they also receive a large amount of fresh water (from river discharge) which could be critical to the maintenance of the Arctic halocline [*Aagaard and Coachman*, 1975]. The cold halocline is essential for the stability of this water structure because it acts as a barrier, preventing heat transfer upwards. The Kara Sea receives more than 1/3 of the total freshwater discharged into the Arctic Ocean [*Hanzlick and Aagaard*, 1980]. The combined mean input of freshwater from the Ob and Yenesei Rivers is 35 x 10^3 m^3 s^{-1} and is directed by the bathymetry of the Kara Sea [*Antonov*, 1960; *Hanzlick and Aagaard*, 1980]. However, the effect of the river outflow on the halocline is highly seasonal since over half of this fresh water input occurs between May and July. Ice melt in the Marginal Ice Zone (MIZ) also supplies a large amount of fresh water into the Kara and Barents Seas. Halocline water can form from ice melt when southward flowing ice meets with surface AW in the MIZ [*Steele et al.*, 1995]. *Aagaard et al.* [1981] have identified two

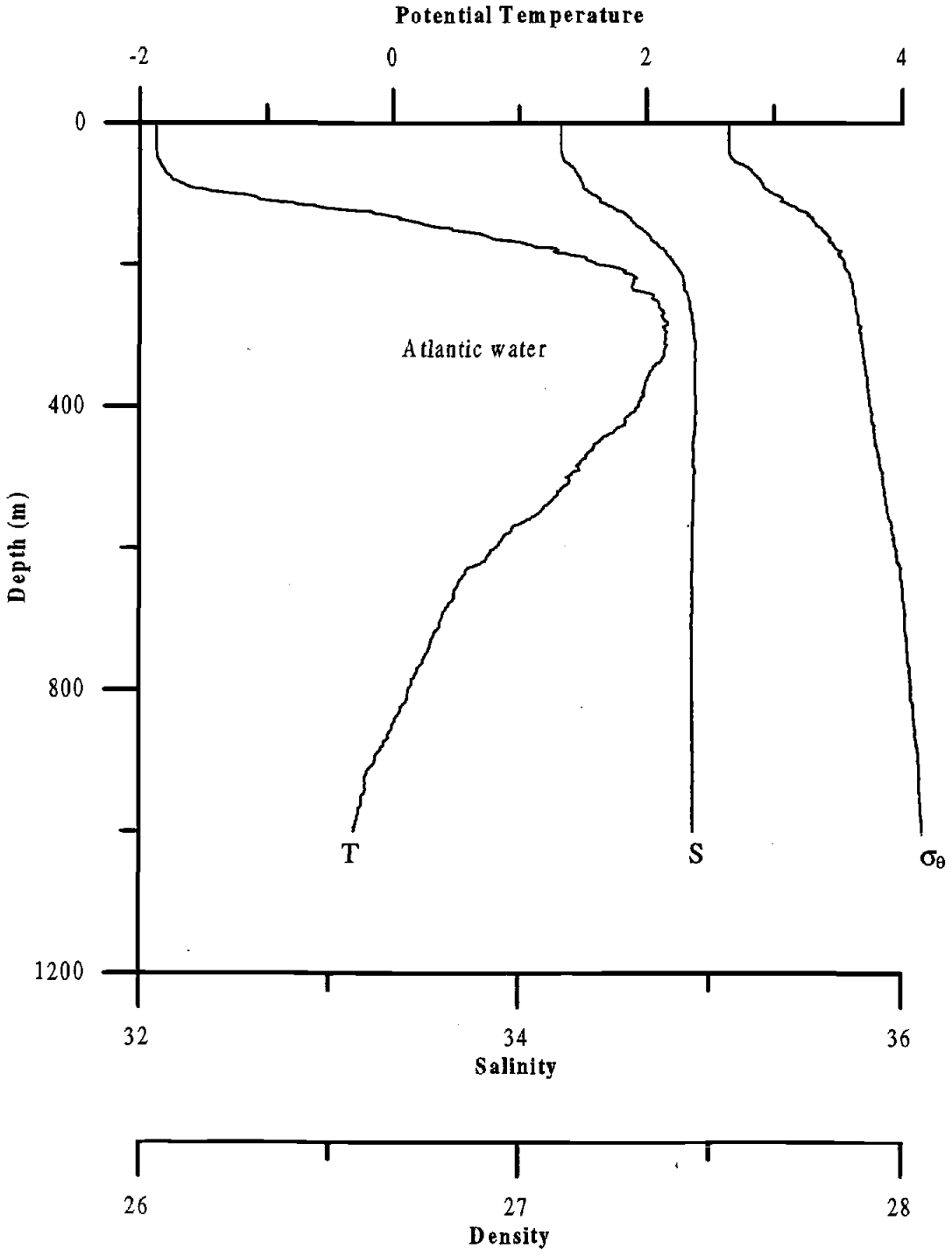

Figure 2.4. Characteristic profiles of potential temperature (T), salinity (S), and density (σ_θ) in the shelf break region of the Eastern Arctic Ocean (EUBEX drop 517).

other halocline formation mechanisms: salinization of cold surface water during ice formation on the shelf, particularly due to coastal polynyas; and mixing of upwelled AIW with cold, fresh summer shelf waters in places like the St. Anna Trough.

2.1.2 *Distribution of Ice Cover*

One of the most important features of the Arctic climate system is the ice cover. In winter, ice cover is an effective insulator, restricting heat fluxes from the relatively warm ocean to the cold atmosphere. Heat transfer from open water can be two orders of magnitude greater than from adjacent thick ice areas [*Maykut*, 1978]. In summer, the high surface albedo (~80%) of snow-covered sea ice greatly reduces the amount of incoming solar radiation that the oceans absorb. Ice-free ocean albedos are generally around 10-15% [*Lamb*, 1982; *Gloerson et al.*, 1993]. Ice cover also affects the hydrographic properties of a region through brine rejection in regions of ice formation or through fresh water input in regions of melting ice. Analysis of ice and processes affecting ice is therefore critical to understanding the hydrographic structure and heat balance of a region.

The ice cover in the eastern Arctic exhibits a significant amount of seasonal variability. Over the entire Arctic, ice extent ranges from approximately 7×10^6 km^2 in summer to $14\text{-}16 \times 10^6$ km^2 in winter [*Walsh and Johnson*, 1979; *Parkinson et al.*, 1987; *Gow and Tucker*, 1990]. Figures 2.5a and 2.5b (derived from Special Sensor Microwave Imager (SSMI) data) illustrate the typical ice cover for summer and winter, respectively. The eastern Arctic shelf seas are almost entirely ice free in the summer (figures 2.5a). In the winter, the ice edge extends into the Barents Sea (figure 2.5b).

The annual mean patterns of sea ice drift and ice residence time (calculated from drifting buoys) are shown in figure 2.6 (figure was obtained from the internet - see appendix A). The map illustrates the presence of two dominant features: the Beaufort Sea Gyre and the Transpolar Drift Stream. Historically, the Beaufort Sea Gyre was thought to be an anticyclonic circulation pattern of ice in the western Arctic Ocean. However, new

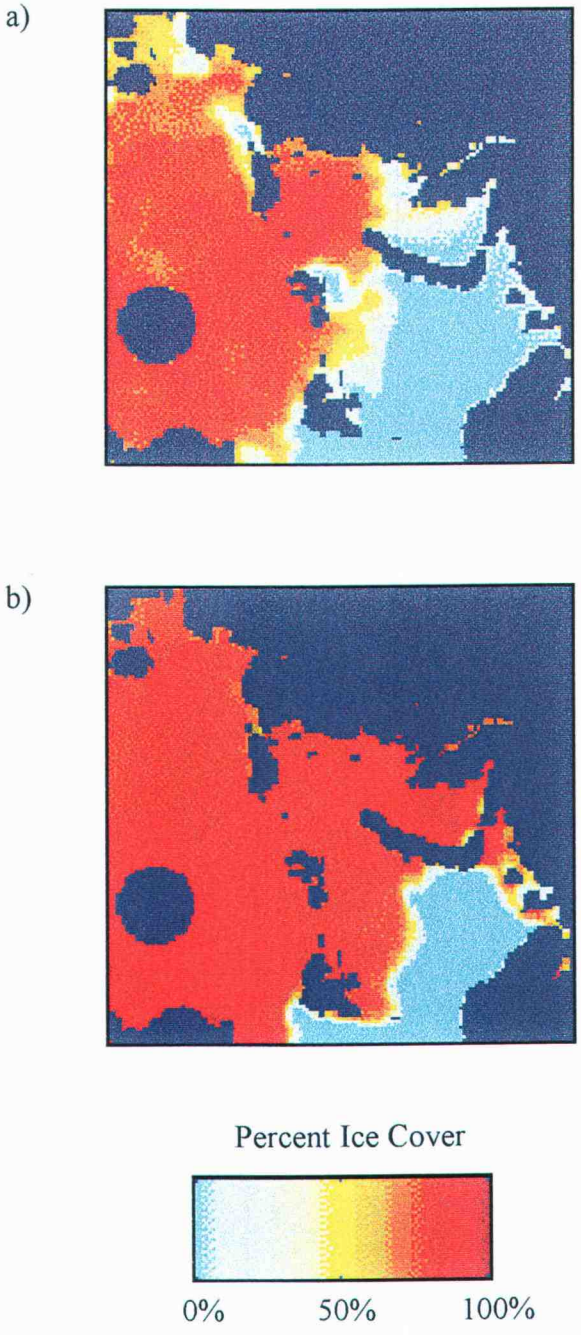

Figure 2.5. Percent ice cover from weekly averaged SSMI data for (a) the first week of March 1989 and (b) the fourth week in July 1989.

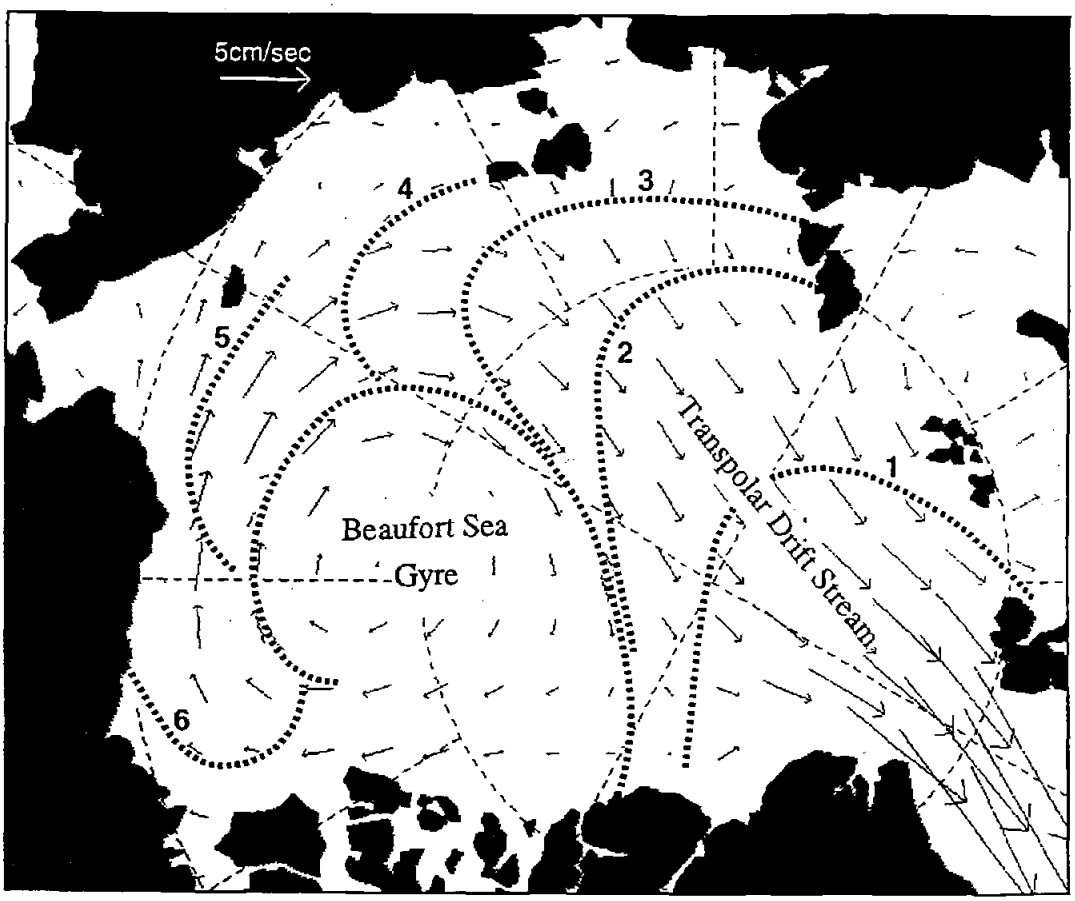

Figure 2.6. Annual mean ice motion in the Arctic based on 1979-1990 buoy data. The superimposed lines indicate the number of years until ice exits the Arctic basin through the Fram Strait (from http:\\www.iabp.apl.washington.edu\isochrone.gif).

evidence [*Proshutinsky and Johnson*, 1997] suggests that it is an alternating clockwise/anti-clockwise circulation pattern which reverses every 5 to 7 years, driven by interannual variations in atmospheric circulation. The Transpolar Drift Stream is a basinwide feature that moves ice from the western Arctic toward the east [*Gow and Tucker*, 1990]. The Fram Strait, which exports approximately 2970 km^3 yr^{-1} of sea ice, is the main pathway through which ice exits the Arctic Ocean [*Aagaard and Carmack*, 1989]. In the eastern Arctic, ice makes its way toward the Greenland Sea by flowing south-westward at a rate of about 2-3 cm s^{-1} over the slopes of the eastern Arctic shelf seas. Ice which has originated in the Kara Sea flows northward until it is entrained in the south-westward flow.

2.1.3 *Tides*

The tidal constituents with which we are concerned have periods of approximately one day ("diurnal") and one-half day ("semi-diurnal"). Using a form ratio, *F*, we can classify the tides according to which type of tidal signal dominates. The form ratio is defined in *Pond and Pickard* [1983] as the ratio of the surface elevation amplitudes of the main diurnal tidal constituents (K_1 and O_1) to the amplitudes of the main semidiurnal tidal constituents (M_2 and S_2). We are primarily interested in which type of tidal constituent dominates the velocity field. Therefore, instead of using surface elevation amplitudes, we calculated the form ratio for the entire Arctic Ocean (figure 2.7) using the rms value for tidal current amplitudes from the Kowalik and Proshutinsky [1994] barotropic tidal model (see section 3.2), i.e.,

$$F = [\mathrm{rms}(K_1) + \mathrm{rms}(O_1)] \,/\, [\mathrm{rms}(M_2) + \mathrm{rms}(S_2)]. \qquad 2.1$$

The rms value for each constituent was obtained using $[\frac{1}{2} (u^2 + v^2)]^{1/2}$ where u and v are the east-west and north-south velocity amplitudes, respectively. As seen in figure 2.7, the semidiurnal tidal currents are the dominant tidal constituents in the eastern Arctic.

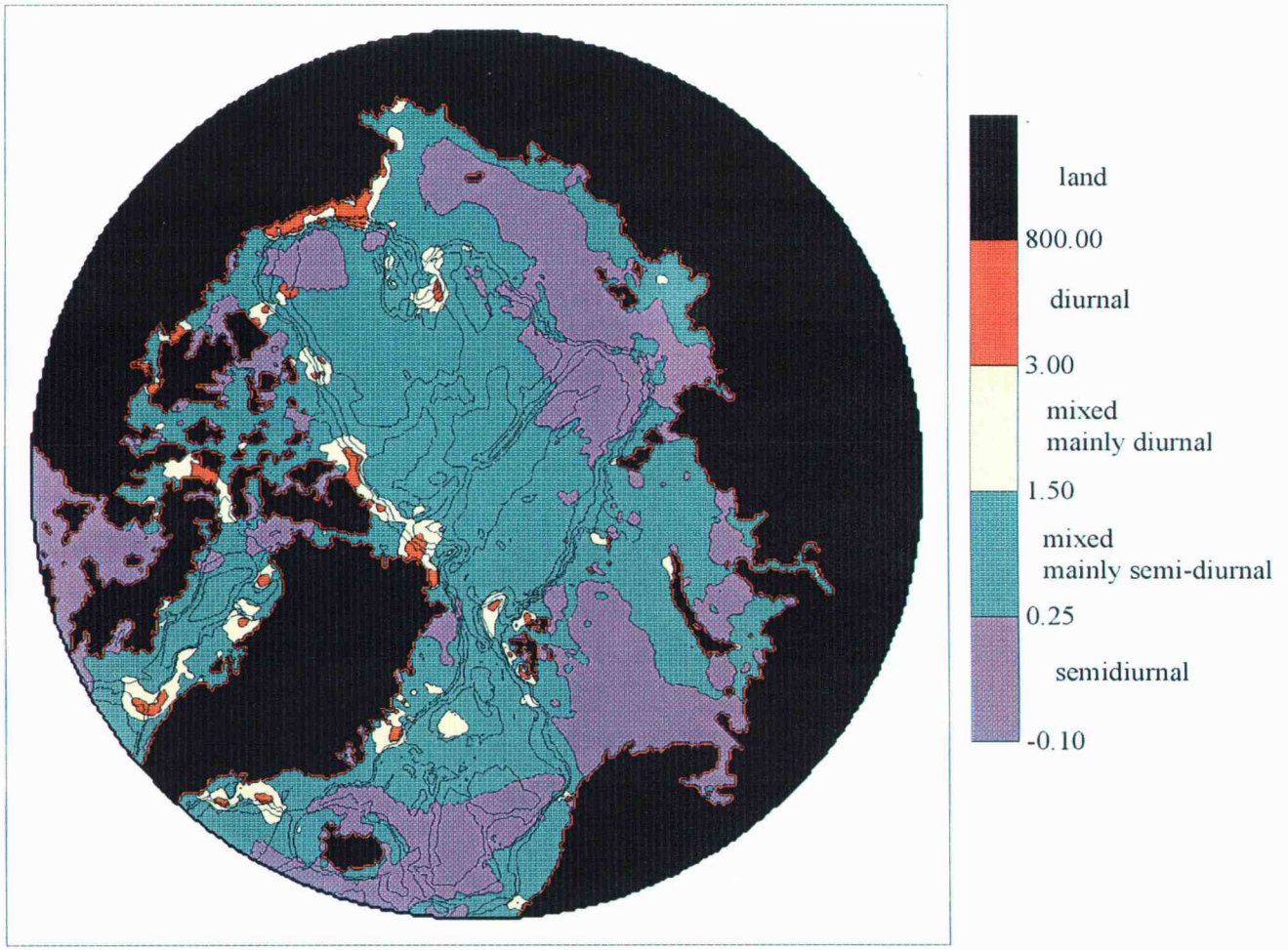

Figure 2.7. The form ratio calculated from velocity amplitudes.

However, over the Yermak Plateau, diurnal tidal currents dominate the tidal signal. The dominance of the diurnal component over the Yermak Plateau has been seen in previous observational studies [*Hunkins*, 1986; *Plueddemann*, 1992; *Padman et al.*, 1992].

The magnitudes of tidal currents in the Arctic Ocean display a significant amount of spatial variability. The tidal currents in the deep basins are generally weak, with magnitudes less than 1 cm s^{-1}. Tidal currents in and near the shelf seas can, however, be very energetic. Figure 2.8 illustrates the maximum velocity of the tidal current, calculated from model output from *Kowalik and Proshutinsky* [1994]. The model velocity shown in figure 2.8 includes contributions from the 4 principal tidal constituents: K_1, O_1, M_2, S_2. As shown in figure 2.8, the tidal currents in the Eastern Arctic are much stronger than the tidal currents in the deeper Arctic basin. On the Northern slopes of the Barents Sea, tidal currents can exceed 75 cm s^{-1}, mainly due to the M_2 tide. These currents are large compared with mean background currents, which are typically only 1-2 cm s^{-1} [*Mellor and Häkkinen*, 1994]. The strength of the tides, combined with their spatial variability, provide a means for altering the water properties of a region due to their influence on mixing rates.

2.2 Mixing By Tides

Ultimately, heat and salt are transferred between water parcels through molecular processes characterized by the following equations

$$\partial S/\partial t = \kappa_s \nabla^2 S + \boldsymbol{u}\cdot\nabla S, \qquad 2.2a$$

and

$$\partial T/\partial t = \kappa_t \nabla^2 T + \boldsymbol{u}\cdot\nabla T, \qquad 2.2b$$

where S is salinity, T is potential temperature, $\boldsymbol{u}$ is the three-dimensional velocity vector (m s^{-1}), and κ_s and κ_t are the molecular diffusivities (m^2 s^{-1}) for salt and heat, respectively. The first term on the right hand side of (2.2) represents molecular diffusion where the

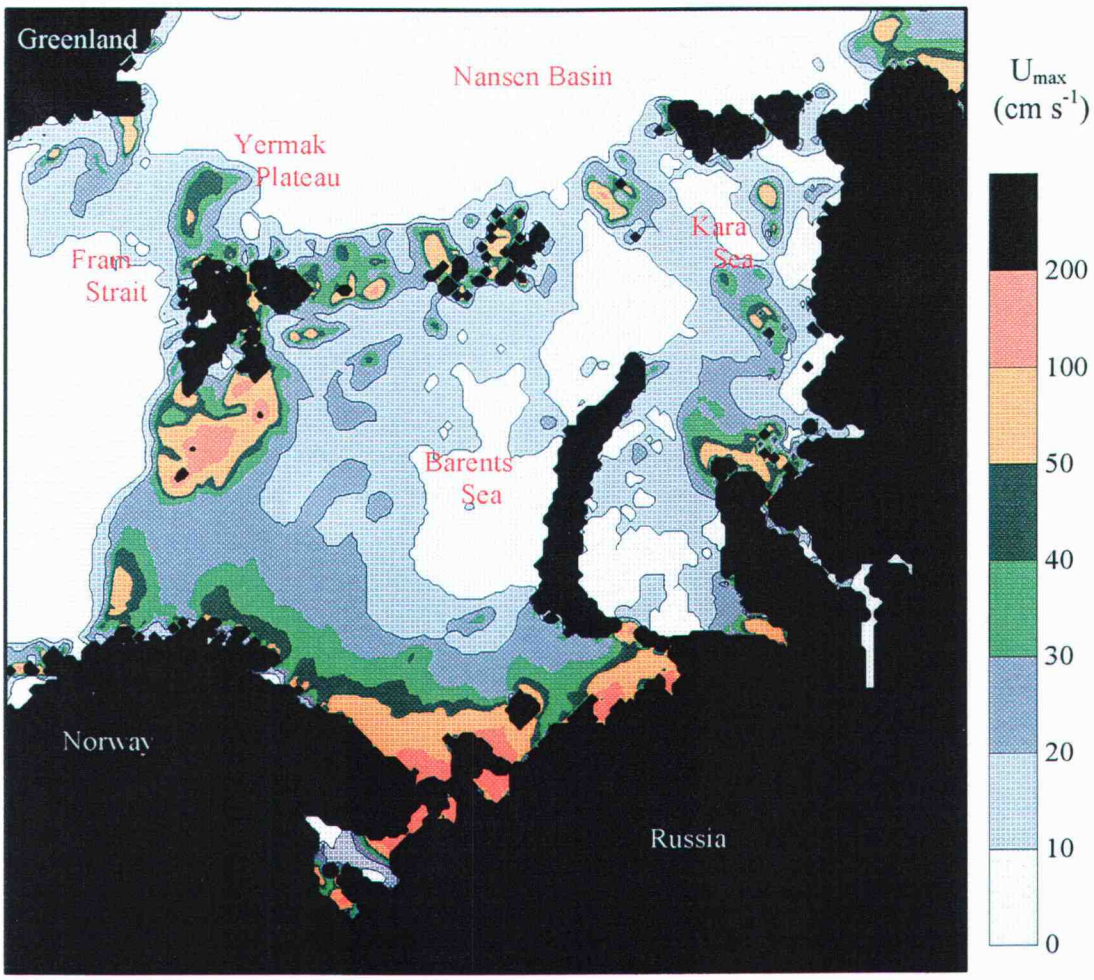

Figure 2.8. Maximum value of tidal current based on the sum of the 8 principal tidal constituents (K_1, O_1, Q_1, P_1, M_2, S_2, K_2, N_2) calculated from the model of *Kowalik and Proshutinsky* [1994] (from *Padman* [1995]).

diffusion coefficients are assumed to vary slowly enough over the spatial scales characteristic of these processes that they can be considered constant, i.e., $\nabla(\kappa_c \nabla C) \equiv \kappa_c \nabla^2 C$. The second term on the right hand side of (2.2) represents advection. Local sources or sinks of heat have been neglected. Transfer by molecular diffusion occurs on scales of about 10^{-3} - 10^{-1} m [*Tennekes and Lumley*, 1995]. Turbulent mixing processes accomplish "diffusion" on larger scales through eddies. The much coarser resolution (order ~ 10's of meters vertically: 10 - 100 km horizontally) of general circulation models prevents either molecular or turbulent processes from being simulated directly. Eddy diffusivities, K, are therefore introduced as practical representations of grid-scale fluid property transfer due to mixing processes that occur on scales smaller than the grid size. The diffusivity K can be thought of as a way to parameterize all the small-scale processes that ultimately contribute to molecular diffusion within some averaging space and time. Unlike the molecular diffusivities, eddy diffusivities are usually assumed to be the same for both heat and salt [*Cushman-Roisin*, 1994] for turbulent mixing in non-double-diffusive environments, although K may be anisotropic. *Altman and Gargett* [1987] showed, however, that this assumption, i.e., $K_s = K_t$, might not always be valid. *Gargett and Holloway* [1992] suggested that the ratio K_s/K_t was more important in determining thermohaline circulation and the T and S properties of intermediate and deep water than the actual values of K_s and K_t. More recent studies [*Merryfield*, pers. comm. 1996] suggest that simply allowing K_s/K_t to vary realistically in double-diffusive regions solves many global-scale model inconsistencies.

Using the same eddy diffusivity parameterization for both heat and salt, assuming horizontal isotropy, and neglecting advection, the diffusion equations become

$$\partial S/\partial t = K_h \left(\langle \partial^2 S/\partial x^2 \rangle + \langle \partial^2 S/\partial y^2 \rangle \right) + K_v \langle \partial^2 S/\partial z^2 \rangle, \qquad 2.3a$$

and

$$\partial T/\partial t = K_h \left(\langle \partial^2 T/\partial x^2 \rangle + \langle \partial^2 T/\partial y^2 \rangle \right) + K_v \langle \partial^2 T/\partial z^2 \rangle, \qquad 2.3b$$

where K_h and K_v are the horizontal and vertical eddy (or effective) diffusivities, and the angle brackets denote spatial and temporal averaging. In the ocean, isopycnals are

frequently inclined relative to the local horizontal plane. Water parcels can be mixed along an isopycnal more easily than across isopycnals because the exchange of the water parcels along isopycnals involves only small changes in potential energy. It is therefore more natural to define diffusion in terms of these two physically distinct processes: isopycnal mixing and diapycnal mixing. Hence, a more meaningful way to describe the directionality of eddy diffusivities is by using a diapycnal/isopycnal coordinate system and corresponding diffusivities, K_d and K_i [*Gregg*, 1987]. In this system, the vertical or horizontal flux would be regarded as being composed of the portion that diffuses across an isopycnal surface plus the portion that diffuses along the isopycnal surface. The turbulent flux of a scalar C is related to the eddy diffusivities by

$$F_r = K_r \langle \partial C/\partial z_r \rangle, \tag{2.4}$$

where r denotes the direction, F_r is the flux and z is the distance in that direction, and K_r is the effective diffusivity ($m^2\ s^{-1}$) [*Padman,* 1995]. Using diapycnal/isopycnal coordinates, shown in figure 2.9, the flux of a scalar in the local vertical direction, F_v, can be calculated as

$$F_v \approx \phi F_i + F_d, \tag{2.5}$$

$$F_v \approx \phi\, K_i \langle \partial C/\partial z_i \rangle + K_d \langle \partial C/\partial z_d \rangle, \tag{2.6}$$

where F_i and F_d are scalar fluxes in the isopycnal and diapycnal direction, respectively, and ϕ denotes the angle the isopycnal line makes with respect to the horizontal, assumed to be small [*Gregg*, 1987]. In a region where the isopycnals are horizontal, (2.6) reduces to

$$F_v = K_d \langle \partial C/\partial z \rangle, \tag{2.7}$$

where $K_d = K_v$. Assuming that the scalar of interest is temperature, vertical heat fluxes can be determined from

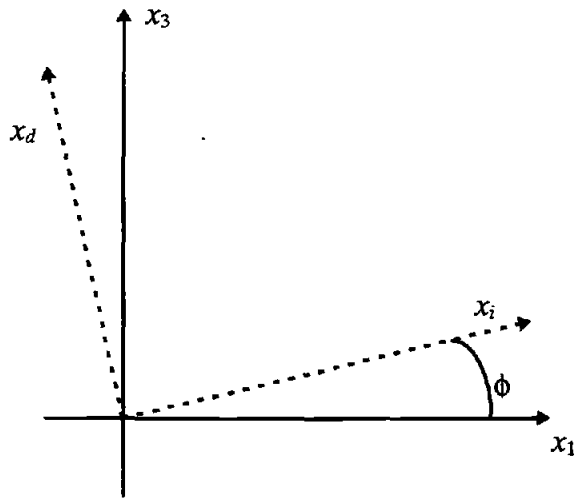

Figure 2.9. Coordinate transformation from horizontal/vertical system (x_1/x_3) to isopycnal/diapycnal system (x_i/x_d).

$$F_H = \rho\, c_p\, K_v\, \langle \partial T/\partial z \rangle, \qquad 2.8$$

where ρ is the density of the seawater (kg m^{-3}) and c_p is the specific heat capacity of seawater (J kg^{-1} K^{-1}).

Eddy diffusivities are expected to be higher in regions with strong mixing than in regions with little turbulence. In the main thermocline, typical values of K_v are about 1×10^{-5} m^2s^{-1} [*Gregg*, 1989]. *Padman and Dillon* [1991] found that K_v in the Arctic permanent pycnocline was about 2×10^{-5} m^2s^{-1} over the relatively featureless Nansen Basin but increased to near 2.5×10^{-4} m^2s^{-1} on the slope of the Yermak Plateau. Values of K_v can exceed 1×10^{-2} m^2s^{-1} in the under-ice, stress-driven mixing layer [*McPhee and Martinson*, 1994]. A higher K_v implies a faster transfer of salt and heat, i.e., water properties are modified more rapidly.

In the Eastern Arctic shelf seas, the interaction of strong tidal currents, rough topography, and ice cover may generate enough turbulence to have a significant influence on the water properties and general circulation of the Arctic Ocean. Examining the Barents Sea, *Parsons* [1995] found that mixing associated with the addition of the M_2 tide to an annually forced Arctic Ocean general circulation model (see section 3.2) caused significant changes in both temperature and salinity throughout the Barents Sea. The maximum differences in the temperature fields between the tidal forcing experiment and the annual forcing experiment found in the water column between 0-2000 m were typically 0.5° C (with maximum differences reaching up to 3° C). Likewise, the salinity differences were typically 0.2 psu but some were as large as 0.8 psu. Recent observational studies have also associated tides with strong mixing in the eastern Arctic Ocean [*D'Asaro and Morison*, 1992; *Padman and Dillon*, 1991; *Padman*, 1995]. Near the Yermak Plateau, *Padman and Dillon* [1991] found that an increase in tidal current strength was able to elevate the surface mixed-layer water temperature by 0.03 °C. The temperature elevation was enough to increase the mean heat flux from the ocean surface mixed layer to the ice from about 3 to 12 W m^{-2}. This study demonstrated that tides are able to generate enough turbulence to mix heat from the Atlantic Layer up to the sea-ice interface.

Tides increase mixing within a water column by increasing stress at the seabed, by increasing stress at the ocean-ice interface, or by generating internal waves which can then break in the pycnocline [*Padman et al.*, 1992; *Padman*, 1995]. These three processes, along with methods for estimating the spatial extent and magnitude of the mixing, are described below.

2.2.1 *Boundary Stress Influence on Water Column Stability*

Stress created at the seabed by bottom currents can significantly affect the stratification of the water column. The turbulent stress due to bottom currents can be approximated by a quadratic stress "law",

$$\tau = \rho\, C_b\, u_b^2, \qquad 2.9$$

where C_b is the bottom drag coefficient and u_b is the velocity of the current near the seabed [*Simpson and Hunter*, 1974]. In shallow seas where tides produce strong bottom currents, the turbulence associated with the bottom stress can be strong enough to mix the entire water column [*Simpson and Hunter*, 1974; *Pingree and Griffiths*, 1978]. The distribution of these vertically well-mixed regions is dependent on both the strength of the current and the depth of the water. The stratification of the water column can therefore change over short spatial scales due to topographic and tidal variations. Boundaries associated with tidal mixing between the highly stratified and well-mixed water are identified as coastal tidal fronts.

Simpson and Hunter [1974] developed a method to identify coastal tidal front areas by using an energy balance argument. It was later extended by *Simpson et al.* [1978] to included wind mixing. To indicate the level of stratification, they used a measurement of the potential energy of the system relative to its fully mixed state (potential energy anomaly ($J\ m^{-3}$)) defined by

$$\Phi = \frac{g}{h}\int_{-h}^{0}[\,(\rho(z)-\bar{\rho})]\,z\,dz, \qquad 2.10$$

where $\bar{\rho}$ is the mean density of the water column, $\rho(z)$ is the water density profile, and g is the acceleration due to gravity [*Simpson and Bowers*, 1981; *Argote et al.*, 1995]. In this model, $\Phi = 0$ for a vertically homogeneous region and Φ becomes more negative for increasingly stratified regimes. Therefore, Φ is also referred to as the stratification parameter.

In general, the potential energy anomaly is determined by three processes: the surface buoyancy flux, tidal mixing, and wind mixing. In the shallow seas studied by *Simpson and Hunter* [1974] and *Simpson et al.* [1978], the surface heat flux is the only significant buoyancy flux term. Surface heating acts to stratify the water column (Φ becomes more negative), while tidal and wind mixing bring about positive Φ changes. The change in Φ due to these effects can be written as

$$\partial\Phi/\partial t = -\alpha_t\, g\, Q\, h\, /2c_p + \varepsilon\, C_b\, \rho\, U_b^3 + \delta\, \gamma\, C_{10}\, \rho_a\, \langle W_{10}^3 \rangle, \qquad 2.11$$

where Q is the rate of heat input (W m^{-2}), α_t is the thermal expansion coefficient (K^{-1}), c_p is the specific heat capacity of seawater (J kg^{-1} K^{-1}), C_b and C_{10} are the bottom and wind drag coefficients, U_b is the tidal amplitude near the seabed (often taken as the vertically integrated amplitude), W_{10} is the wind speed measured 10 m above the surface, ρ_a is the density of air (kg m^{-3}), ε and δ are the flux Richardson numbers for tidal and wind mixing, and γ is the slippage factor [*Argote et al.*, 1995]. The slippage factor is the ratio of the wind-induced surface current to the wind speed [*Simpson and Bowers*, 1981]. The angle brackets denotes the mean value over a tidal cycle [*Simpson and Bowers*, 1981]. Horizontal advection is assumed to be a negligible source or sink of potential energy.

This formulation can be used to locate positions of fronts in shelf seas [*Simpson and Hunter*, 1974; *Pingree and Griffiths*, 1978; *Simpson and Bowers*, 1981]. At a frontal boundary, there must exist a balance between the stratification forces and the mixing forces, i.e., $\partial\Phi/\partial t = 0$. Although wind mixing does affect the value of Φ, wind is not as

important as tides in determining the position of the front because the wind field is more spatially homogenous [*Simpson et al.*, 1978; *Simpson and Bowers*, 1981]. Therefore, wind mixing is often neglected in equation (2.11). At the frontal boundary, we are left with the balance,

$$\alpha_t \, g \, Q \, h / 2c_p \; = \varepsilon \, C_b \, \rho \, U_b^3, \tag{2.12}$$

which can be rewritten as

$$h / (C_b \, U_b^3) \; = \varepsilon \; \rho \, 2c_p / \; \alpha_t \, g \, Q \, . \tag{2.13}$$

The critical value, λ_{crit}, necessary for the occurrence of a well-mixed region is defined as the value of $h / (C_b \, U_b^3)$ at which this balance occurs, i.e.,

$$\lambda_{crit} = (\varepsilon \, \rho \, 2c_p) / (\alpha_t \, g \, Q). \tag{2.14}$$

Assuming all variables other than h and U_b are spatially uniform, the critical value will therefore lie along an h / U_b^3 contour [*Argote et al.*, 1995]. The ratio of the stratification source term to the mixing terms is therefore a convenient measure of stratification of a water column. This ratio

$$R = (\alpha_t \, g \, Q \, h / 2c_p) / (\varepsilon \, C_b \, \rho \, U_b^3), \tag{2.15}$$

i.e.,

$$R \propto h / U_b^3, \tag{2.16}$$

implies that changes in the stratification of the water column will take place across h / U_b^3 contours (assuming that the other terms in the equation are constant).

Although the theoretical formulation is quite useful in understanding the reasons for the tidal and topographic control of the fronts, it is not useful for determining the critical value. Even when wind mixing and other buoyancy source terms can be neglected,

$\lambda_{crit} = (\varepsilon \rho 2c_p) / (\alpha_t g Q)$ is hard to calculate accurately due to many uncertainties and variations in Q, and ε as well as in C_b. To accurately calculate λ_{crit} in an observational study, all sources and sinks of potential energy must be included, which makes the above approach difficult and an inaccurate way to find the critical value. Other approaches have therefore been taken to determine λ_{crit}.

Pingree and Griffiths [1978] define the Simpson-Hunter parameter, S (in cgs units), as

$$S = \log_{10} [h / (C_b U_b^3)]. \qquad 2.17$$

The logarithmic scale is used to reduce the numerical range of the values. To identify the critical Simpson-Hunter parameter for the British Isles, *Pingree and Griffiths* [1978] used a numerical model to derive the Simpson-Hunter parameter and then compared the position of fronts observed from infrared satellite images to maps of S. They found S_{crit} to be about 1.5. The Simpson-Hunter parameter was also used by *Kowalik and Proshutinsky* [1995] to identify the location of the tidal front around Bear Island. They used the critical value of $S = 1.5$ from *Pingree et al.* [1978]. Many studies [e.g., *Garrett et al.*, 1978; *Bowman et al.*, 1980; *Schumacher et al.*, 1979] have investigated the critical value by comparing the location of the coastal tidal front, obtained from both hydrographic observations and models, to contours of S':

$$S' = \log_{10} [h / U_b^3]. \qquad 2.18$$

From hydrographic data, *Schumacher et al.* [1979] showed that a front observed in the Bering Sea was parallel to the $S' \approx 3.5$ contour (now defined in MKS units). *Argote et al.* [1995] defined the critical values of S' in the Gulf of California by examining the potential energy from the model. *Argote et al.* [1995] defined the front as the region where $\Phi \cong -10$ J m^{-3}. After comparing this contour with a contour map of S', *Argote et al.* [1995] found that the front lies along the critical contour value between 2.75 and 3.0 (MKS units). *Bowers and Simpson* [1987] found the critical value of S' to be 2.4 (MKS) around

the European shelf seas. These studies confirmed that the position of coastal tidal fronts parallel h/U_b^3 contours.

In the Arctic, the Simpson-Hunter parameter might not adequately represent changes in stratification due to the simple formulation of the buoyancy term and the absence of ice effects. Freezing and melting as well as runoff can be more important buoyancy source terms than heating in high latitudes [*Schumacher et al.*, 1979]. Therefore, to determine what effects other buoyancy terms have, we can reformulate the theoretical development of *Simpson and Hunter* [1974] by including surface buoyancy flux terms which account for the effects of salt fluxes as well as heat.

The effects of heating, evaporation, and precipitation on buoyancy ($-g\,\rho$) are expressed as the buoyancy flux B, defined by *Gill* [1982] as

$$B = \alpha_t\, g\, Q / c_p \;+\; \beta\, g\, (E - P)\, S_o, \qquad 2.19$$

where β is the expansion coefficient for salinity, E and P represent the rates of evaporation and precipitation, respectively, and S_o is the surface salinity. To use the same notation as *Simpson and Hunter* [1974], we will define Q to be positive downward. Runoff and melting ice would increase the buoyancy of the water column and therefore can be added to B as

$$B = -\alpha_t\, g\, Q / c_p \;+\; \beta\, g\, (E - P)\, S_o \;-\; \beta\, g\, R\, S_o \;-\; \beta\, g\, I_m\, S_o, \qquad 2.20$$

where R is the rate of fresh water addition from runoff and I_m is the rate of fresh water input from ice melt (a negative I_m would indicate freezing, which would decrease buoyancy by raising the salinity of the water column). The change in potential energy due to surface buoyancy fluxes can therefore be written as

$$d\Phi/dt = \tfrac{1}{2}\{-\alpha_t\, g\, Q\, h / c_p \;+\beta\, g\, (E - P - R - I_m)\, S_o\, h\}. \qquad 2.21$$

As well as affecting the buoyancy flux term, ice in the Kara and Barents Seas could also play an important role in the mixing term through stress at the ice-ocean interface (see the following section. The surface stress at the ice-ocean interface, τ_s, can be approximated by

$$\tau_s = \rho\, C_s\, u^2_{rel}. \qquad 2.22$$

where C_s is a drag coefficient and u_{rel} is the velocity of the current with respect to the ice. The rate of work done from the tidal motion is

$$dE/dt \approx \tau_{surf}\, u_{rel} = \rho\, C_s\, u^3_{rel}. \qquad 2.23$$

A fraction, δ_{ice}, of this energy is available to raise the potential energy of the water column (most is used for turbulent kinetic energy production and is dissipated without changing the potential energy). Therefore, the change in potential energy related to the presence of ice cover is

$$d\Phi/dt = \delta_{ice}\, \rho\, C_s\, U^3, \qquad 2.24$$

where $\varepsilon \le \delta_{ice} \le \delta$ and δ_{ice} accounts for the relative motion of the ice with respect to the underlying water. The amplitude of the tidal current, U, is used.

By including all the sources and sinks of potential energy, with the exception of advection, the change in the potential energy due to the both buoyancy flux and mixing can be written as

$$\partial\Phi/\partial t = \tfrac{1}{2}\, h\, g\{-\alpha_t\, Q/c_p + \beta\,(E - P - R - I_m)S_o\} + \varepsilon\, C_b\, \rho\, U_b^3 + \delta\, \gamma\, C_{10}\, \rho_a\, \langle W_{10}^3 \rangle + \delta_{ice}\, \rho\, C_s\, U^3. \qquad 2.25$$

Following the argument of *Simpson and Hunter* [1974], the tidal front exists where $\partial\Phi/\partial t = 0$, or

$$\tfrac{1}{2} h g\{\alpha_t Q / c_p - \beta(E - P - R - I_m)S_o\} = \varepsilon C_b \rho U_b^3 + \delta \gamma C_{10} \rho_a \langle W_{10}^3 \rangle + \delta_{ice} \rho C_s U^3. \quad 2.26$$

To examine the effects that ice could have on the frontal position, we can first look at a simple model that excludes wind mixing, precipitation, and evaporation due to their spatial homogeneity. Runoff effects will be highly seasonal and if we avoid these for now, we are left with

$$\tfrac{1}{2} h g \{ \alpha_t Q/c_p + \beta I_m S_o \} = \varepsilon C_b \rho U_b^3 + \delta_{ice} \rho C_s U^3. \quad 2.27$$

Assuming that U_b is equal to U (both are the vertically integrated tidal velocity amplitudes), we find that the ratio of stratification to mixing terms is

$$\begin{aligned} R' &= \tfrac{1}{2} h g [\alpha_t Q/c_p + \beta I_m S_o] / [\varepsilon C_b \rho U_b^3 + \delta_{ice} \rho C_s U^3], \quad 2.28 \\ &= \tfrac{1}{2} h g [\alpha_t Q/c_p + \beta I_m S_o] / [U^3 \rho (\varepsilon C_b + \delta_{ice} C_s)], \\ &\propto h / U^3, \end{aligned}$$

and changes in stratification will again take place along the h/U^3 contours. However, with the inclusion of ice effects, the critical value will be different, i.e.

$$S'_{crit} = \log_{10}[h /U^3] = \log_{10}[2 \rho (\varepsilon C_b + \delta_{ice} C_s) / \{g (\alpha Q/c_p + \beta I_m S_o)\}]. \quad 2.29$$

Examining the h/U^3 contours will therefore still be useful in examining mixing induced by tidal stress in the Arctic Ocean.

2.2.2 *Ice-Ocean Interaction*

Over the open ocean, wind exerts stress on the ocean surface and produces turbulent mixing in the surface layer. Although the presence of ice reduces the mixing generated directly by wind stress, ice motion relative to the upper ocean provides a new source of stress and therefore another source of mixing. For certain ice conditions, this stress can be magnified substantially by tidal currents [*Padman et al.*, 1992], and can result in increased vertical fluxes through the upper ocean to the ice-ocean interface.

As mentioned above in section 2.2.1, the surface stress at the ice-ocean interface can be approximated by equation 2.22. Measurements of U_{rel} and C_s are typically taken at 1 m below the ice base. Values of C_s range from 0.001 for smooth first year ice to about 0.006 for multiyear ice [*Padman,* 1995]. In large scale models, boundary layers are frequently not resolved, and so U_{rel} is taken to be the velocity difference between the ice velocity and the velocity of the underlying "free stream" layer. *Kowalik and Proshutinsky* [1994] use $C_s = 0.0055$ as the drag coefficient of the ice base in their Arctic tidal model. The stress, τ_s, generates mixing in the surface boundary layer. The friction velocity (ms^{-1}), which is defined as

$$u_* = (\tau_s / \rho)^{1/2} = (C_s)^{1/2} U_{rel}, \qquad 2.30$$

characterizes the turbulent kinetic energy by representing the characteristic velocity scale of turbulent eddies. Large values of u_* indicate energetic mixing. Friction velocity is also an important term when calculating the heat flux from the surface mixed layer to the ice ($F_{H,I}$). This heat flux, measured in W m^{-2}, can be estimated empirically, following *McPhee* [1992], as

$$F_{H,I} = \rho \, c_p \, c_h \, u_* \, (T_{ML} - T_{freeze}), \qquad 2.31$$

where c_h is a "heat exchange" coefficient, T_{ML} is the temperature (°C) of the surface mixed layer, and T_{freeze} is the freezing temperature (°C) of the surface mixed layer for the

measured salinity. Increases in either u_* or $(T_{ML} - T_{freeze})$ increase the heat flux from the ocean to the overlying ice. Tidal currents can modify both of these variables and therefore alter the oceanic heat reaching the ice cover.

Tidal currents can increase u_* (equation 2.30) either by increasing U_{rel} or by increasing C_s. The ability of the tides to increase either variable depends not only on the strength of the tides but also on the characteristics of the ice itself. In the Kara and Barents Sea, ice can range from land-fast ice to pancake ice. Each ice type responds differently to stresses applied by the tidal currents.

Land-fast ice remains firmly attached to land, i.e., by definition it does not move in response to underlying currents. Therefore, any increase in the current velocity will cause an equal increase in U_{rel} and hence increase u_* [*Padman*, 1995]. Tidal currents can often be an order of magnitude greater than the background ocean currents and therefore could substantially affect $F_{H,I}$. In the presence of strong tides, the stress from the bottom boundary layer plus the stress at the surface boundary layer from the land-fast ice would cause significant turbulence, possibly throughout the water column.

Other types of ice do not exhibit the same behavior as land-fast ice. At the opposite end of the ice scale, pancake-ice motion closely mimics the motion of the underlying current field. Increases in tidal currents result in increases in ice motion as well. The relative velocity between the ice sheet and ocean therefore remains relatively small. As a result, tidal velocities do not lead to any significant changes in u_*.

Most ice responds to tidal currents in a way that lies somewhere between the lack of response of rigid land-fast ice and the highly-coupled response of pancake ice. The response of an ice sheet depends on the relationship between the horizontal length scale over which the ice sheet is effectively rigid, L_i, and the spatial scale of the variations of tidal current velocities, L_t. If the ice sheet is effectively rigid over larger scales than the tidal currents, i.e., $L_i > L_t$, then the ice sheet will be only weakly coupled to the local underlying current. *Padman et al.* [1992] found that diurnal ice motion over the Yermak Plateau in winter was an order of magnitude lower than the oceanic tidal currents. Winter ice tends to be more compact and has larger L_i values than less rigid summer ice. The weak coupling implies that the underlying current accelerates without a corresponding

increase in the velocity of the ice sheet, thus increasing U_{rel}. If L_i is much smaller than L_t, the ice motion is able to more easily respond to the motion of the underlying current field. Strong diurnal ice motion is often observed in summer when ice is less compact and is more easily coupled to the local tidal motion [*Hoffman*, 1990; *Prazuck*, 1991]. Satellite-tracked ice buoys in "free ice" over the Yermak Plateau in summer often exhibit an elliptical pattern corresponding to diurnal tidal motion [*Prazuck*, 1991]. Increases in tidal currents therefore result in increases in ice motion and thus may not increase U_{rel} substantially.

The drag coefficent, C_s, can be affected by tidal currents as well. As mentioned in section 2.1, the strength of tidal currents in the Kara and Barents Sea can vary over small spatial scales associated with variations in topography. These variations apply stresses (shear and strain) to the base of the ice sheet. If sufficiently large, the internal stresses in the ice sheet created by the tidal currents can break the ice apart into smaller floes. Newly formed ice, such as pancake ice, has many weak areas and therefore is more likely to respond to the shear and strain by breaking apart than compact multi-year ice. If the tidal field is also significantly divergent or convergent, the motion of the small ice floes responding to tidal motion will create either leads due to an expansion in the ice field, or ridges from colliding ice floes. Continuous ridging and lead formation substantially deform the ice and therefore increases the effective drag coefficient of the ice.

As seen from equation (2.31), the heat flux from the mixed layer to the ice is not only affected by the friction velocity but also the temperature of the surface mixed layer. To increase T_{ML} in the absence of incoming solar radiation, heat must be supplied to the base of the surface mixed layer from the Atlantic Layer. This process also requires energetic mixing. The following section will discuss the processes responsible for mixing within the pycnocline below the surface mixed layer.

2.2.3 *Pycnocline Response to Tides*

Internal waves are a ubiquitous feature throughout the stratified interior of the world's oceans. Instabilities in the internal wave field are thought to be one of the main mechanisms for mixing in the pycnocline. When internal waves become unstable, they break and produce turbulence (see *Gregg* [1987] and *Munk* [1981] for useful reviews). One way to analyze the stability of the water column is to examine the ratio of buoyancy (which act to stabilize the fluid) to shear (which tends to destroy stability). This ratio is called the gradient Richardson number, *Ri*, and is defined as

$$Ri = N^2 / (\partial U/\partial z)^2, \qquad 2.32$$

where N is the buoyancy frequency and U is the horizontal component of velocity. When the shear in the flow is sufficiently large and/or the density gradient is sufficiently small, the flow can become dynamically unstable and produce turbulence. A value of *Ri* of approximately 1 is needed to produce advective instabilities in a finite amplitude wave field [*Orlanski and Bryan*, 1969; *Munk*, 1981]. A necessary condition for Kelvin-Helmholtz (or shear) instabilities is that *Ri* is less than 0.25 [*Turner*, 1973; *Munk*, 1981].

One method that has proven to be quite significant in the generation of internal waves is the interaction of the barotropic tides with topography. This process produces internal waves at tidal frequencies (internal tides) [e.g., *Wunsch*,1975; *Huthnance*, 1989; *New and Pingree*, 1990]. In general, the dominant internal tides occur at frequencies corresponding the dominant semidiurnal (M_2 and S_2) and diurnal (K_1 and O_1) tidal constituents [*Wunsch*, 1975]. Near the continental slope, however, higher harmonics (e.g., M_3, M_4) are also observed [*Huthnance*, 1989]. The frequency, ω, of an internal wave is bounded by the effective coriolis frequency (the coriolis parameter, f, plus ½ the mean relative vorticity, ζ) and N, i.e., $(f + \frac{1}{2}\zeta) < \omega < N$ [*Kunze*, 1985]. In most flows, ζ is negligible compared with f. Therefore, the frequency of an internal wave is generally said to be bounded by $f < \omega < N$. At high latitudes, the diurnal internal tidal frequency is much smaller than f. Therefore, in the Arctic Ocean, free internal tides at the diurnal

Tidal constituent	Period (h)†	Frequency (cph)	Critical latitude (degrees)
Principal diurnal			
Q_1	26.868	0.0372	26.4499
O_1	25.819	0.0387	27.6140
P_1	24.066	0.0416	29.8199
K_1	23.935	0.0418	29.9998
Principal semi-diurnal			
N_2	12.658	0.0790	70.9868
M_2	12.421	0.0805	74.4685
S_2	12.000	0.0833	85.7773
K_2	11.967	0.0836	90.0000

† from Apel [1987]

Table 2.1. The period, frequency, and critical latitude for the eight principal tidal constituents (four diurnal, four semi-diurnal).

frequency do not exist. Table 2.1 gives a list of critical latitudes (latitude at which $\omega = f$) for the eight main tidal constituents. Recent studies in the eastern Arctic indicate that there might be a significant amount of energy entering the semi-diurnal internal wave field. Over the Yermak Plateau, *Padman et al.* [1991] found significant shear near the semidiurnal tidal frequency, even though diurnal tides dominate the barotropic currents. *D'Asaro and Morison* [1992] proposed that the interaction of the barotropic M_2 tide with topography could be one mechanism responsible for the spectral peak near f, found over the Yermak Plateau. *Plueddemann* [1992] also found evidence for bottom generation of semi-diurnal internal waves around the Yermak plateau from the Arctic Environmental Drifting Buoy (AEDB) measurements (see section 5). Measurements such as these suggest that the Eastern Arctic could be strongly influenced by mixing associated with topographically generated semi-diurnal internal tides. Although measurements provide evidence for this occurrence, they do not provide adequate spatial coverage of this region. Analytical models provide a way to investigate the spatial variability of energy fluxes into the internal wave field, and therefore into possible turbulence, over a large region.

Several methods have been developed to model the generation of internal tides and to calculate the energy flux into the internal wave field from topography [*Rattray*, 1960; *Baines*, 1973; *Bell*, 1975; *Sjöberg and Stigebrandt*, 1992]. Two complementary approaches, the mode approach of *Sjöberg and Stigebrandt* [1992] and the composite ray theory approach of *Baines* [1982], will be used in this paper to investigate internal tide generation over the eastern Arctic shelf seas. Both methods are described below.

2.2.3.1 Sjöberg and Stigebrandt [1992]

Sjöberg and Stigebrandt [1992] (hereafter referred to as SS92) developed a simple model, assuming step-like topography, to explain the generation process in terms of modes, extending the analytical model of *Stigebrandt* [1980] to include a non-constant, but analytically defined, buoyancy frequency and multiple steps. SS92 used this model to

calculate the energy flux into baroclinic modes at steps in topography. The following summarizes the basic development of this model, following SS92.

The coordinate system employed by SS92 is shown in figure 2.10. In this coordinate system, $z = 0$ at the bottom and $z = H$ at the ocean's surface. A step of height d (at $z = d$) is assumed to occur in the topography at $x = 0$.

To calculate the energy flux into internal tides, first the normal mode solution for the horizontal velocity is found from the equations of motion without friction or rotation. Assume that density varies with depth as

$$\rho\,(z) = a - b/[1 - (H\text{-}z)/\delta], \tag{2.33}$$

where a and b are coefficients such that $\rho\,(H) = \rho_1$ and $\rho\,(0) = \rho_2$ $(\rho_1 < \rho_2)$ and δ is a parameter used to scale the thermocline thickness. The buoyancy frequency, N^2, can then be written as

$$N^2 = N_o^2\,(1 + H/\delta) / [1 + (H\text{-}z)/\delta]^2, \tag{2.34}$$

where

$$N_o^2 = g\,(\rho_2 - \rho_1) / (\rho_o H). \tag{2.35}$$

In equation 2.35, ρ_o is a reference density chosen from observations to be an average value. By using the method of separation of variables, we can write

$$u = \Sigma\, u_n(x,y,t)\, U_n(z),$$
$$v = \Sigma\, v_n(x,y,t)\, U_n(z),$$

where $u_n(x,y,t)$ and $v_n(x,y,t)$ describe the horizontal nature of mode "n" and $U_n(z)$ describes the vertical structure [*Kundu*, 1990]. Considering only free baroclinic waves, the normal mode solution for the vertical structure of the horizontal velocity is found to be

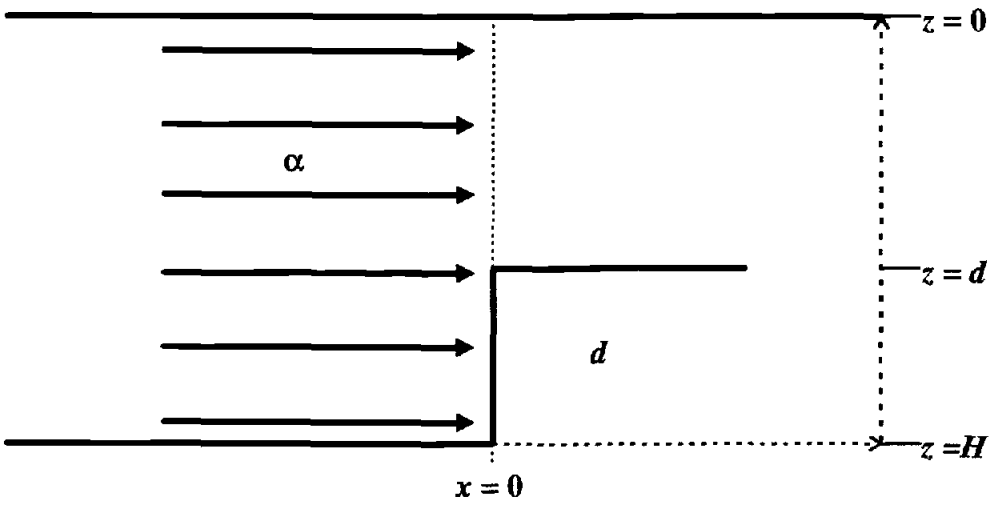

Figure 2.10. SS92 model illustration. A barotropic tidal current with amplitude α encounters a step of height d at $x = 0$. The total depth of the water column is H.

$$U_n(z) = (1+(H-z)/\delta)^{-1/2} (\sin\{\upsilon_n \ln[1 + (H-z)/\delta]\}/2 + \upsilon_n \cos\{\upsilon_n \ln[1 + (H-z)/\delta]\}), \quad 2.36$$

where

$$\upsilon_n = n\,\pi / \ln(1 + H/\delta) \quad 2.37$$

and

$$k_n^2 = (\upsilon_n^2 + 0.25)\, \omega^2 N_o^{-2} (1 + H/\delta)^{-1} \delta^{-2}. \quad 2.38$$

In these equations, k_n is the horizontal wave number for the given mode "n", and ω is the tidal frequency. $U_n(z)$ is normalized so that $\int_0^H U_n^2(z)\, dz = H$.

Assume that the problem is two-dimensional, i.e., $v_n = 0$ and no y-dependence. Furthermore, assume that $u_n(x,t)$ has a solution of the form $u_n(x,t) = a_n e^{kx-i\omega t}$. We can then solve for u_n by imposing boundary conditions at the step ($x = 0$). When a barotropic tide encounters a step in topography, a baroclinic component of the flow is required to satisfy the boundary condition at the step. This can be seen by looking at the velocity profile where the step occurs. At $x = 0$, the velocity profile, $f(z)$, above the step is known and the normal velocity below the top of the step ($z < d$) must vanish ($\boldsymbol{u} \cdot \boldsymbol{n} = 0$). In the absence of the step, the barotropic velocity is given by $\alpha\, e^{-i\omega t}$, where α is the tidal current amplitude. Therefore, to satisfy the boundary condition at $x = 0$, the barotropic and baroclinic modes are added,

$$\alpha\, e^{-i\omega t} + \sum a_n U_n(z)\, e^{-i\omega t} = \begin{cases} f(z)\, e^{-i\omega t} & \text{for } d < z < H \\ 0 & \text{for } z < d. \end{cases} \quad 2.39$$

We can then rewrite $f(z)$ as

$$f(z) = [\alpha H / (H - d)]\, g(z), \quad 2.40$$

where

$$\int_d^H g(z)\,dz = (H\text{-}d). \qquad 2.41$$

The assumption leading to (2.41) is that the depth-integrated mass transport must be the same with or without the step.

The coefficients, a_n, can be found by multiplying (2.39) by U_m (all modes are mutually orthogonal), integrating over the entire depth, and using the fact that for baroclinic modes, $\int_0^H U_n(z) = 0$. The coefficients are found to be

$$a_n = \alpha\,(\mathrm{H\text{-}d})^{-1} \int_d^H g(z)\,U_n(z)\,dz. \qquad 2.42$$

The coefficients can be further simplified by assuming that $g(z)$ is a step function, i.e., g=1 for $d < z < H$, and 0 for $z < d$, and by using (2.34) for $U_n(z)$,

$$a_n = \alpha\,\delta\,(H\text{-}d)^{-1}\,\{2H / [\delta \ln(1 + H/\delta)(0.25 + \upsilon_n^2)]\}^{1/2} \qquad 2.43$$
$$\times\,[1 + (H\text{-}d)/\delta]^{1/2}\,\sin\{\upsilon_n \ln[1 + (H\text{-}d)/\delta]\}.$$

The horizontal velocity component can therefore be written as

$$u = \Sigma\, a_n\, e^{i(kx-wt)}\, U_n(z), \qquad 2.44$$

where a_n is described by (2.43) and $U_n(z)$ is described in (2.34).

Following *LeBlond and Mysak* [1978], the horizontal energy flux, F [W m^{-1}], through a vertical section is calculated using

$$F = \tfrac{1}{4} \int (p\,u^* + p^*\,u)\,dz, \qquad 2.45$$

where u was defined in (2.44), $p = \rho\,\omega\,\Sigma\,a_n\,U_n(z)/k_n\,e^{i(kx-\omega t)}$, and * indicates the complex conjugate. By averaging F over t and x, the energy flux at a step can be rewritten as

$$F = \Sigma F_n, \qquad 2.46$$

where F_n is the energy flux of each mode at a step, written as

$$F_n = \tfrac{1}{2} \rho \omega (a_n)^2 H / k_n, \qquad 2.47$$

$$F_n = \frac{\alpha^2 \rho N_o \delta^2 [1+(H-d)/\delta] [1+ H/\delta]^{1/2} \sin^2\{\upsilon_n \ln(1+(H-d)/\delta)\}}{(1-d/H)^2 \ln(1+H/\delta) (1/4 +\upsilon_n^2)^{3/2}} . \qquad 2.48$$

The development of F_n did not take the effects of rotation into account. *Sjöberg and Stigebrandt* [1992] did find that the inclusion of f, when $\omega > f$, acts to disperse the waves, and that the energy flux therefore decreases by a factor of $(\omega^2 - f^2) / \omega^2$. The energy flux for mode "n" at a step is then

$$F_n = \frac{\alpha^2 \rho N_o \delta^2 [1+(H-d)/\delta] [1+ H/\delta]^{1/2} \sin^2\{\upsilon_n \ln(1+(H-d)/\delta)\} (\omega^2 - f^2)^{1/2}}{(1-d/H)^2 \ln(1+H/\delta) (1/4 +\upsilon_n^2)^{3/2} \omega} . \qquad 2.49$$

SS92 used (2.49) in combination with gridded databases of bathymetry, vertical density stratification, and barotropic tides to estimate the horizontal variation in the global energy flux into internal tides. They were mainly concerned with the deep ocean and only looked at depths greater than 1000 m. Their results showed that most of the energy flux, about 40-50%, occurred in regions where the depth was between 1000 m and 2000 m. This corresponded to areas where the slope was usually the steepest, the barotropic velocities the largest, and stratification the strongest [SS92]. They also found that most of the energy flux is concentrated in the first baroclinic mode. The sum of the energy fluxes in modes 2-10 typically contribute only half of the energy that occurs in mode 1.

2.2.3.2 Baines Method

Baines [1973] developed a ray-integral method which is based on the theory of wave characteristics for examining internal tide generation. This procedure is useful in solving the internal wave field for continuously stratified fluids where topography varies in the x-direction [*Baines*, 1982]. Once the equations are solved, energy fluxes into internal tides can be found. *Baines* [1982] extended the ray-integral method into a composite model that also allowed for excitement of the interfacial mode when appropriate conditions exist. Below is a summary of the composite ray-theory model according to *Baines* [1982].

To formulate an equation of motion for an internal tide, we begin with the linear governing equations for a rotating stratified inviscid fluid (with static case subtracted out):

$$\rho_o (\partial \boldsymbol{u}/\partial t) + \rho_o \boldsymbol{f} \times \boldsymbol{u} + \nabla p + \rho g \hat{z} = 0, \qquad 2.50$$

$$\partial \rho/\partial t + w(d\rho_o/dz) = 0, \qquad 2.51$$

$$\nabla \cdot \boldsymbol{u} = 0, \qquad 2.52$$

where $p_o(z)$ and $\rho_o(z)$ are the vertical profiles of pressure and density in static equilibrium and p and ρ are the perturbations in pressure and density from this state due to wave motion. The barotropic and baroclinic effects are then separated by letting

$$\boldsymbol{u} = \boldsymbol{u}_1 + \boldsymbol{u}_i , \qquad p = p_1 + p_i , \qquad 2.53$$

where the subscript '1' denotes a field corresponding to an unstratified ocean of density $\langle \rho_o \rangle$ (the mean vertical value of $\rho_o(z)$) which constitutes the motion of the barotropic tide. The 'i' subscript denotes the internal (or baroclinic) fields. The governing equations for the internal tides can then be written as

$$\langle \rho_o \rangle (\partial \boldsymbol{u}_i/\partial t) + \langle \rho_o \rangle \boldsymbol{f} \times \boldsymbol{u}_i + \nabla p_i + \rho\, g \hat{z} = 0, \qquad 2.54$$

$$\partial\rho/\partial t + w_i(d\rho_o/dz) + w_1(d\rho_o/dz) = 0, \qquad 2.55$$

$$\nabla\cdot\boldsymbol{u}_i = 0. \qquad 2.56$$

Baroclinic motion develops when upslope flow onto the shelf creates horizontal density gradients [*Huthnance*, 1989]. If we express the density as $\rho = \rho_1 + \rho'$ where ρ_1 is the density perturbation caused by barotropic motion, then 2.54 can be rewritten as

$$(\partial\boldsymbol{u}_i/\partial t) + \boldsymbol{f}\times\boldsymbol{u}_i + (1/\langle\rho_o\rangle)\nabla p_i + g\,\rho'/\langle\rho_o\rangle\,\hat{z} = \boldsymbol{F} = -g\,\rho_1/\langle\rho_o\rangle\,\hat{z}. \qquad 2.57$$

This equation shows how internal wave motion is driven by a body force $\boldsymbol{F}$. The body force $\boldsymbol{F}$ was shown by *Baines* [1973] to depend on N^2, the volume flux per meter of shelf length (q), and the topography (h). Assuming that the problem is only two-dimensional, the forcing function can be rewritten as

$$\boldsymbol{F} = (N(z))^2\, z\,[q(x)\,(h^{-2}\,dh/dx)]\;(\sin\omega t)/\omega\,\hat{z}, \qquad 2.58$$

(see *Baines* [1973,1982] for further details).

By defining the stream function ψ for the internal wave field as

$$u_i = -\psi_z, \qquad w_i = \psi_x, \qquad 2.59$$

equations (2.54) - (2.58) become

$$\nabla^2\psi_{tt} + N^2\psi_{xx} + f^2\psi_{zz} = q\,N^2(z)\,z\,(1/h)_{xx}\cos\omega t. \qquad 2.60$$

By looking for solutions with frequency ω, i.e. $\psi = \Psi(x,z)\,e^{-i\omega t}$, (2.60) can be rewritten as

$$\Psi_{xx} - c^2(z)\,\Psi_{zz} = [q\,z\,(1/h)_{xx}]/[1-(\omega^2/N^2)], \qquad 2.61$$

where c is the wave characteristic slope, defined as

$$c = [(\omega^2 - f^2) / (N^2 - \omega^2)]^{1/2}. \qquad 2.62$$

There are two general procedures, depending on the importance of the density interface, that can be taken to solve 2.61. If the interface weak (i.e, the generation region lies within region A of figure 3 of *Baines* [1982]), then the ray theory method can be used (see *Baines* [1973, 1982] for description. If the interface is important (i.e, the generation region lies within region B of figure 3 of *Baines* [1982]), the first mode is calculated separately and then the ray theory method is used for the remainder. This method is known as the composite model (see *Baines* [1982]). Variations in the problem exist depending on whether the slope, μ, is 'flat' ($\mu/c < 1$) [*Baines*, 1973] or 'steep' ($\mu/c > 1$) [*Baines*, 1982].

The shallow thermocline is modeled in the composite model by using a density interface described by the following N^2 profile

$$N^2 = 0, \qquad -d < z < 0, \qquad 2.63a$$

$$N^2 = N_o^2 + g' \delta(z+d), \qquad -h < z \leq -d, \qquad 2.63b$$

where d indicates the depth of interface, δ denotes the dirac delta function, $g' = g \Delta\rho_o / \rho_o$, and N_o is assumed to be constant. In the composite model, waves can be generated both on the interface and in the continuum below.

Baines [1982] used his composite model to estimate energy fluxes into the global oceans from continental shelf-slope regions. In general, the energy produced near a shelf-break region propagates away in both the shoreward and seaward directions on both the interface and the deep continuum [*Baines*, 1982] (figure 2.11). Assuming a 'steep' slope, the shoreward energy flux for continuous stratification is generally negligible. The continental shelf-break can most often be classified as a 'steep' slope. However, a 'flat' slope, when they are encountered, generally produces small energy fluxes in both the seaward and shoreward directions. Therefore, the equations that summarize energy fluxes

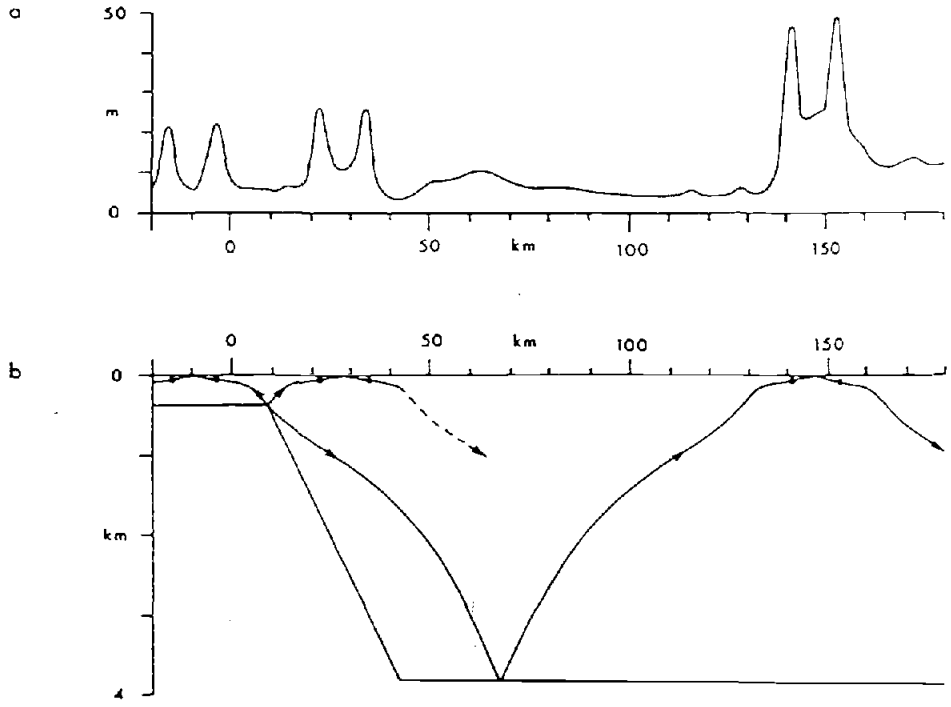

Figure 2.11. (a) Internal tidal amplitudes at a depth of 50 m as predicted by the numerical model of *New* [1988]. Horizontal distance represents km into the deep ocean from the 200 m contour. (b) Model topography and characteristic ray paths showing the propagation of internal tidal energy. The intersections of the rays with the 50 m depth are indicated by black dots, and correspond to regions of large amplitude in figure (a).

(Wm^{-1}) from continental shelf-break regions (based on Appendix B from *Baines* [1982]) are

$$F_{interfacial} = K_1 \rho_o q^2 (g'/d)^{1/2} (1-f^2/\omega^2) \text{ , interfacial shorewards;} \quad 2.64$$

$$F_{interfacial} = K_2 \rho_o q^2 (g'/d)^{1/2} (1-f^2/\omega^2) \text{ , interfacial seawards; and} \quad 2.65$$

$$F_{continous} = K_3 \rho_o q^2 N_o (1-f^2/\omega^2) \mid 1-\Phi(0)\mid^2 \text{, continuous seawards for } \mu/c > 1, \quad 2.66$$

where K_1 and K_2 depend on the ratio of the interface depth to the shelf depth (d / h_L) and K_3 is assumed to be a constant (0.072). In equation 2.66, N_o is a representative value of N in the generation region. The factor $\mid 1-\Phi(0)\mid$ represents the effect of the interfacial motion on the forcing for generation in the stratified continuum [*Baines*, 1982]. Complete descriptions of variables are given in Appendix B of *Baines* [1982].

3. DATA AND MODELS

To examine the generation of internal tides and tide-induced mixing in the eastern Arctic Ocean, this study uses a combination of satellite data, analytical models (described in the previous chapter), output from numerical models, and *in situ* observations. The specific data sets and numerical models used in this study are described below.

3.1 Special Sensor Microwave Imager (SSMI)

Special Sensor Microwave Imager (SSMI) data, which provides daily ice concentration data for both the northern and southern hemispheres from 1987-1994, was obtained from the National Snow and Ice Data Center (NSIDC), University of Colorado for web sites and ftp sites, see appendix). The SSMI sensor is a seven-channel, four-frequency, passive microwave radiometer which measures brightness temperatures at 19.35, 22.235, 37.0, and 85.5 GHz. All frequencies are measured for both vertical and horizontal polarizations with the exception of the 22.235 GHz channel, which is measured for vertical polarization only [*Steffen and Schweiger*, 1991]. SSMIs were flown aboard the sun-synchronous F-8 and F-11 satellites launched by the Defense Meteorological Satellite Program (DMSP). The SSMI aboard the F-8 satellite collected daily brightness temperature data from 6/18/87 - 12/31/91. The sensor aboard the F-11 satellite collected data from 11/28/91 to the present. Data collected from the SSMI sensors can be also used to distinguish between first year and multi-year ice, as well as detecting areas of open water.

For this study, SSMI data was obtained from NSIDC in the form of daily sea ice concentration data which had been gridded in polar stereographic coordinates at a resolution of 25 x 25 km. For F-8 data, two different ice concentration data sets are available. One set is calculated from brightness temperatures using the "NASA Team" algorithm [*Cavalieri et al.*, 1984] and the other using the "Bootstrap" algorithm [*Comiso*, 1986]. Weather filters were included in both these algorithms. F-11 ice concentration

data grids were only processed using the NASA Team algorithm, which included a weather filter. Comparisons of these two algorithms have been discussed by *Steffen and Schweiger* [1991], *Steffen et al.* [1992], and *Emery et al.* [1994]. Based on results from *Steffen et al.* [1992], the NASA Team algorithm showed better results than the Bootstrap algorithm in a dynamic ice zone dominated by continuously forming open water areas and thick ice, while the Bootstrap algorithm performed better in areas with substantial amounts of thin ice. In the Central Arctic, *Steffen et al.* [1992] found that both algorithms agree to within a few percent. Since this study will be interested the variations within the dynamic ice zone, data derived from the NASA Team algorithm will be used to examine sea ice extent in the Barents Sea.

3.2 Kowalik and Proshutinsky Arctic Tidal Model

Output from the Arctic tidal model by *Kowalik and Proshutinsky* [1994] was used to analyze tides in the Arctic Ocean. The model solves the two-dimensional equations of motion and continuity for both water and ice on a stereographic map projection (see *Kowalik and Proshutinsky* [1994] for a complete description). The model is barotropic (1 layer) with varying bottom depth. The first order non-linear shallow water equations include tidal forcing, horizontal friction, friction at the ice-water interface, and friction at the sea-bed. The nonlinear equations of motion for ice include friction at the ice-ocean interface as well as a constitutive law proposed by *Rothrock* [1975] to describe the internal ice forces. The constitutive law assumes ice is a viscous medium and also assumes that tensile stress in the ice is negligible when compared to compressive stress. The tidal forcing terms include tide-generating potential along with various corrections due to earth tide and ocean loading. Amplitudes and phases for every constituent are specified along open boundaries using a combination of satellite data [*Cartwright et al.*, 1991] and model data [*Schwiderski*, 1979, 1981, a, b, c; *Zahel*, 1977]. The model domain is 440 by 440 grid points with a spatial resolution of 14 km and covers the Arctic Ocean, Nordic Seas, Baffin Bay, and Hudson Bay.

The inclusion of ice dynamics in the *Kowalik and Proshutinsky* [1994] tidal model had a minor impact on the overall propagation of tides in the Arctic Ocean. Based on model experiments [*Kowalik and Proshutinsky*, 1994], the ice cover had a weak damping effect, decreasing the amplitude of sea level oscillations by 3% and producing a phase lag between 4.5° and 5°. The tides, however, had a significant impact on the motion of the ice.

The results from the Arctic tidal model [*Kowalik and Proshutinsky*, 1994] were acquired via ftp. Files containing information on sea level amplitude and phase, U (zonal component) amplitude and phase, and V(meridional component) amplitude and phase were obtained for the K_1, O_1, Q_1, P_1, M_2, S_2, K_2, and N_2 tidal constituents. These files were obtained in a 10 x 10 minute spherical grid format which had been interpolated from the stereographic model projection. Arctic bathymetry data was also obtained in the above format from the same site. Further information on the web sites and ftp sites used in the acquisition of this data can be found in the Appendix. For the purpose of this study, the data were reformatted from the polar grid into a 335 by 335 *x-y* array with a spatial resolution of approximately 20 km.

3.3 Arctic Ocean General Circulation Model

A high resolution, *z*-coordinate Arctic Ocean general circulation model (GCM) was developed by *Parsons* [1995]. The model is based on the Semtner-Chervin GCM with a free surface [*Semtner*, 1974; *Semtner and Chervin*, 1988; *Killworth et al.*, 1989], which allows the model to generate both barotropic and baroclinic components of motion. *Parsons* [1995] developed several versions of the model: the annual forcing model, the tidal forcing model, and the seasonal forcing model. This study uses output from the tidal forcing model, which includes the M_2 tide as well as forcing from temperature and salinity fluxes and annual mean wind stress.

The tidal forcing model uses a backward-forward Euler scheme to solve the primitive equations: the *u* and *v* momentum equations (including tidal forcing), the

hydrostatic equation, the continuity equation, the conservation equations for heat and salt, and the *Bryan and Cox* [1972] equation of state for density. The equations were solved on a spherical coordinate system. When using spherical coordinates, the convergence of meridians to a singularity at the North Pole causes numerical problems. Therefore, the model domain was mapped onto a grid system centered over the equator to avoid the singularity. The model grid was 60 degrees by 50 degrees (361 by 301 grid points), and the resulting resolution was approximately 18 km. Information on the original latitude for each grid point was retained to determine the correct coriolis parameter. The model has 30 vertical levels ranging in thickness from 20 m to 200 m. The thickness of each level is shown in table 3.1. Gridded bathymetric data compiled from several sources (ETOPO-5 and hand-gridded data sets from W. Maslowski, A. Proshutinsky, R. Parsons, and N. Cherkis) were used to define the bottom boundary.

The model imposes a no-slip, no-normal flow, boundary condition ($u = v = 0$) at the lateral walls. Salt and heat cannot be transported through the lateral or bottom boundaries. At the bottom, the flow is required to follow the slope of the bathymetry.

The *Parsons* [1995] model was initialized with annual mean temperature and salinity data from the *Levitus and Boyer* [1994] and the *Levitus et al.* [1994] climatological atlases. The annual mean data sets, which have a horizontal resolution of 1° and 33 vertical levels, were interpolated to fit the model grid.

The surface fluxes of heat and salt were prescribed by restoring the surface layer to these mean values every 30 days. Within 3° of the model boundary in the North Atlantic and North Sea, the entire vertical grid was restored to annual values every 30 days to better represent the interior flow across the boundary. The model was forced by an annual average of the 1992 wind stress provided by the European Center for Medium Range Weather Forecasting (ECMWF). The tidal model was also forced by the M_2 tide, which included corrections [*Schwiderski*, 1981] for ocean loading and the earth tide.

The quadratic bottom coefficient in the tidal forcing model was set to 2.65×10^{-3}. To represent the effects of lateral turbulent mixing, the model uses a biharmonic form of friction [*Böning and Budich*,1992], given by

Model Level	Layer Thickness (m)	Bottom Depth (m)	Mid-Depth of Layer (m)
1	20	20	10
2	25	45	32.5
3	25	70	57.5
4	30	100	85
5	40	140	120
6	40	180	160
7	40	220	200
8	60	280	250
9	80	360	320
10	80	440	400
11	120	560	500
12	140	700	630
13-30	200	900-4300	

Table 3.1. The thickness and depth of the layers in the Arctic baroclinic model of *Parsons* [1995].

$$F(\boldsymbol{u})_h = A_h \nabla^4_h (\boldsymbol{u}), \tag{3.1}$$

and

$$F(C)_h = K_h \nabla^4_h (C), \tag{3.2}$$

where A_h is the horizontal biharmonic viscosity coefficient, K_h is the diffusion coefficient, and C is either temperature or salinity. In the *Parsons* [1995] model, biharmonic coefficients for horizontal viscosity and diffusion were set to -4×10^{11} m^4s^{-1}. The vertical viscosity and diffusion coefficients were defined using a Richardson-number-based vertical mixing scheme. Using this scheme requires first the calculation of the Richardson number, *Ri*,

$$Ri = N^2 / [\langle \partial u/\partial z \rangle^2 + \langle \partial v/\partial z \rangle^2], \tag{3.3}$$

where $\langle \partial u/\partial z \rangle$ and $\langle \partial v/\partial z \rangle$ represent the vertically averaged vertical shear in the horizontal velocity components. The vertical viscosity (A_v) and diffusion (K_v) coefficients are then calculated following *Munk and Anderson* [1948], with modifications made by *Endoch et al.* [1981] and *Brooks* [1994],

$$A_v = A_{vo} / (1 + 10\, Ri)^{1/2}, \tag{3.4}$$

and

$$K_v = K_{vo} / (1 + 3.3\, Ri)^{3/2}, \tag{3.5}$$

where A_{vo} and K_{vo} are chosen in this model to be 1×10^{-2} m^2s^{-1} and 5×10^{-3} m^2s^{-1}, respectively. The dependence of A_v and K_v on *Ri* is shown in figure 3.1. Further details of the model are described by *Parsons* [1995].

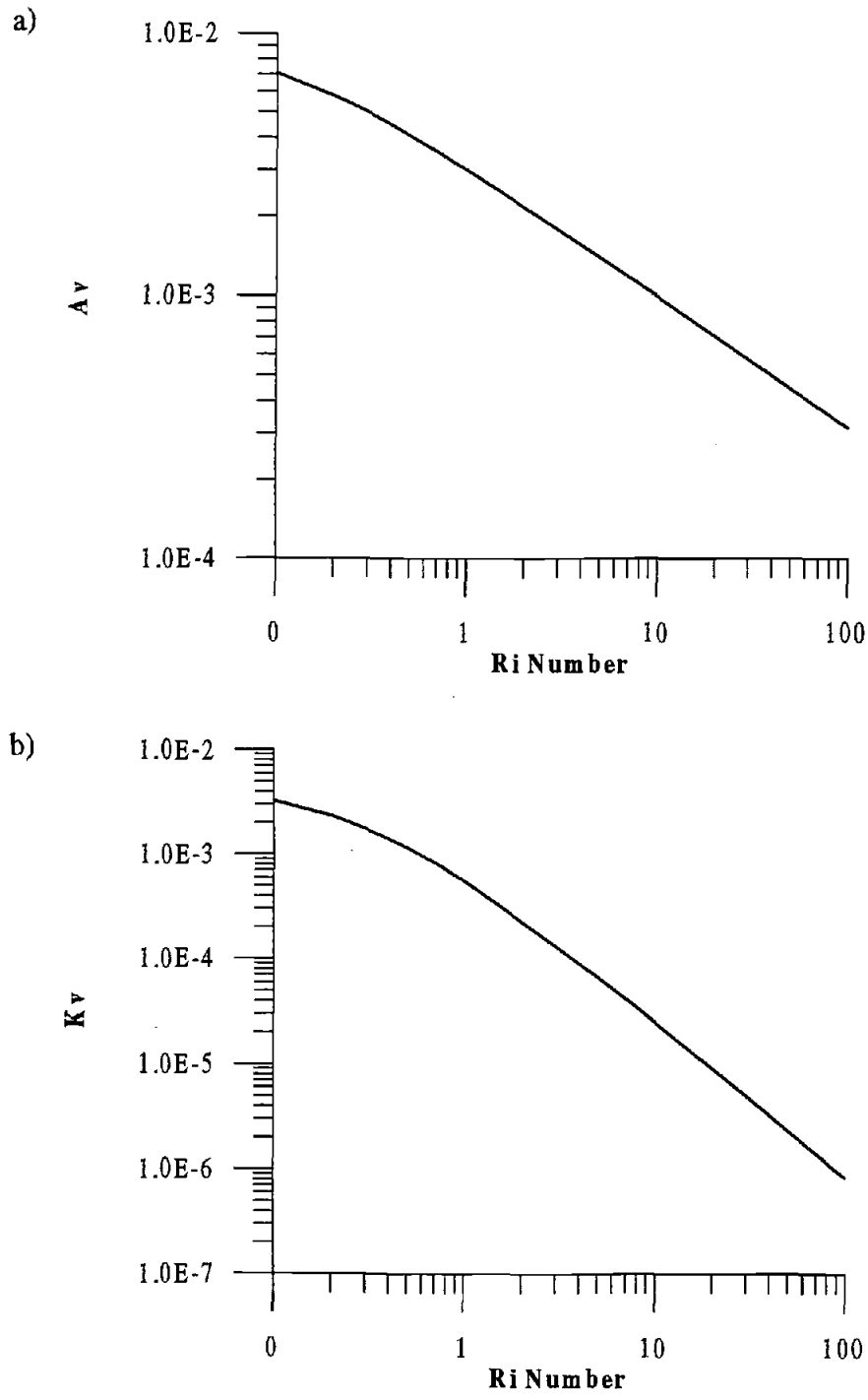

Figure 3.1. The relationship between Richardson number and (a) vertical viscosity, A_v (m^2s^{-1}), and (b) vertical diffusivity, K_v (m^2s^{-1}), calculated from equations 3.4 and 3.5, respectively.

3.4 Observational Studies

Results from several observational studies are used to examine the hydrographic structure of the eastern Arctic and validate model results. Many of the analyses of these data sets has been performed by others. In general, their results will be used in section 5 for comparison with model results. However, some of the data sets were obtained from the principal investigators so that further analyses could be performed on them.

EUBEX data, covering the region from Svalbard to 84° 40' N between 0° and 32°E [*Perkins and Lewis*,1984], was obtained from the Eastern Arctic CD-ROM. These data were used to define characteristic profiles for the eastern Arctic slope region. The data consisted of 28 temperature and salinity profiles, extending down to1 km in 2 meter increments. Drop 517, whose location is shown in figure 3.2, was taken as a characteristic profile for this region. The profile itself is shown in figure 2.4.

To validate model results, we use several small-scale process studies described by *Padman and Dillon* [1991], *Plueddemann* [1992], *D'Asaro and Morison* [1992], and *Padman* [1995]. The Arctic Environmental Drifting Buoy (AEDB) data set was kindly provided by A. J. Plueddemann.

As part of the Coordinated Eastern Arctic Experiment (CEAREX), *Padman and Dillon* [1991] recorded 1500 profiles of temperature, salinity, and velocity microstructure at the CEAREX "O" ice camp. The ice camp drifted from the deep Nansen Basin to the Yermak Plateau during March and April of 1989. A map of the drift track is shown in figure 3.3 (from *Padman and Dillon* [1991]). *Padman and Dillon* [1991] used these measurements to calculate dissipation rates, and so estimate vertical diffusivities and heat fluxes.

Plueddemann [1992] used AEDB measurements to analyze internal waves in the eastern Arctic. The 150 kHz acoustic Doppler current profiler (ADCP) on the buoy collected velocity profiles at half-hour intervals for 216 days. The drift track is shown in figure 3.4. Velocity data were obtained between 35 and 327 m with 15 m resolution. Data were processed and put into forty 7.5 m depth cells of hourly averaged data (see *Plueddemann* [1992] for processing details). Depth bins are shown in table 3.2.

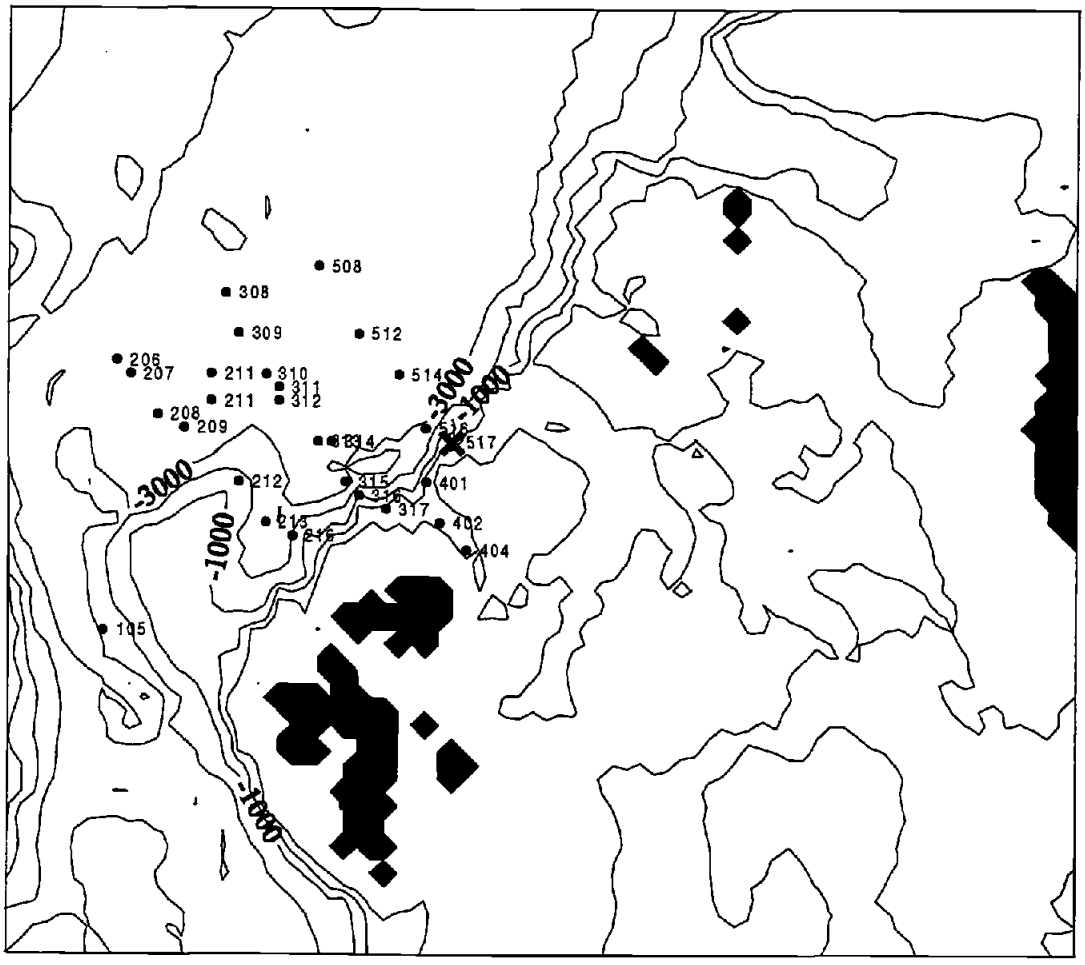

Figure 3.2 Position of EUBEX profiles, with drop numbers indicated. Drop 517 is indicated by (**x**).

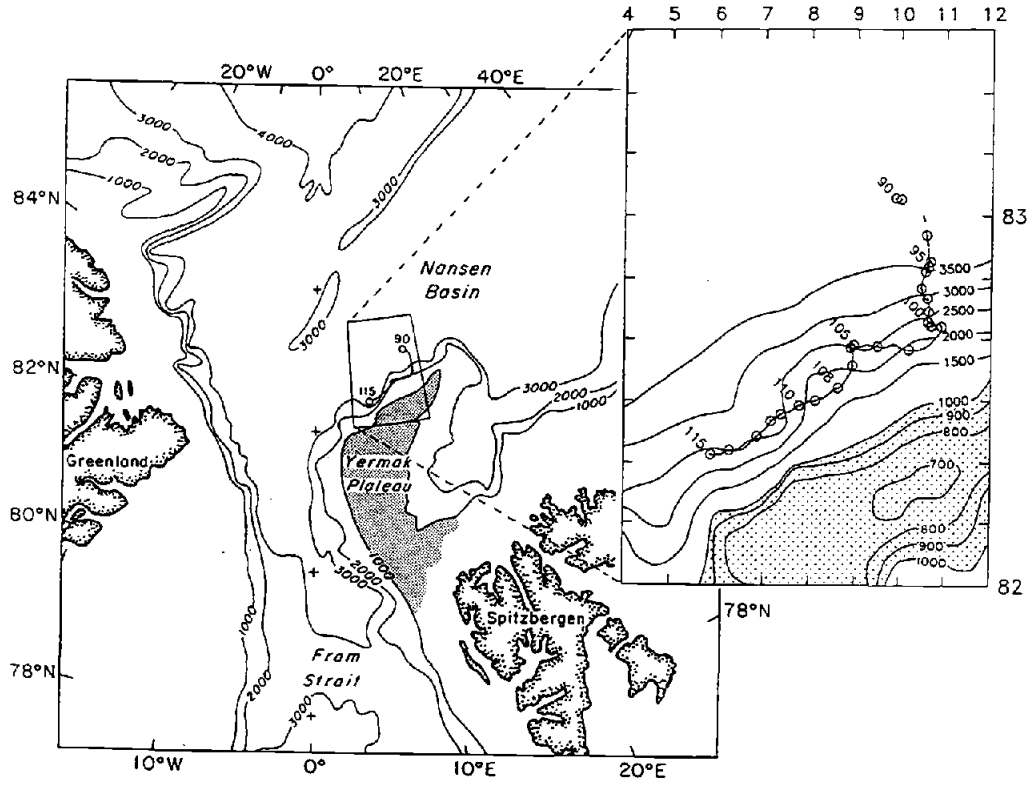

Figure 3.3 Drift track of CEAREX "O" camp from March 31 (day 90) to April 25 (day115), 1989. Depth contours are in meters: time along drift track is in day of year, with one day between adjacent symbols (from *Padman and Dillon* [1991]).

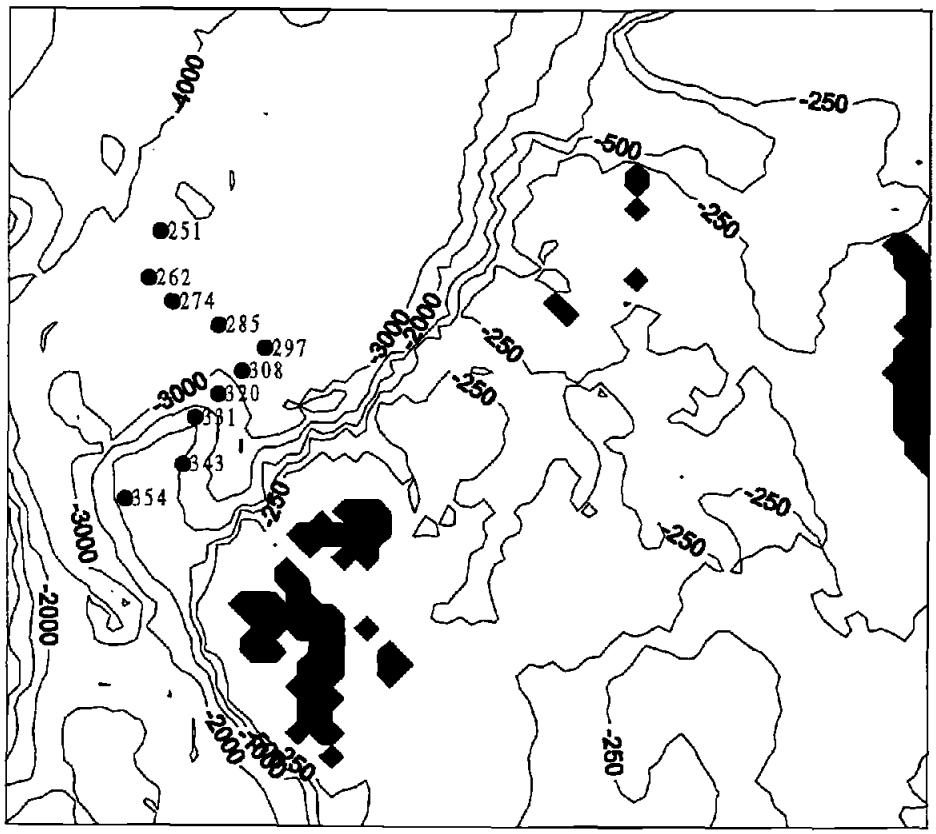

Figure 3.4. AEDB drift track between days 251 and 354. Numbers indicate day of year.

Bin number	Depth(m)
3	51.4
4	59.2
5	67.1
6	75.0
7	82.8
8	90.7
9	98.5
10	106.4
11	114.3
12	122.1
13	130.0
14	137.8
15	145.7
16	153.6
17	161.4
18	169.3
19	177.1
20	185.0
21	192.9
22	200.7
23	208.6
24	216.4
25	224.3
26	232.2
27	240.0
28	247.9
29	255.7
30	263.6

Table 3.2. Bin number and depths (m) for AEDB data.

D'Asaro and Morison [1992] used expendable velocity profilers and CTD data to examine the variability of the internal wave field and associated shears in the Eastern Arctic. The data were obtained as part of the MIZEX 83 and *Polarstern* Arktis IV/3 programs. Figure 3.5 (from *D'Asaro and Morison* [1992]) gives the geographical location of the data. Diapycnal diffusivities were estimated from velocity shears by applying the parameterization of *Gregg* [1989].

As evident in the spatial maps of the data sets, most of these small-scale measurements have been made near the Yermak Plateau. Small-scale process studies are absent over the northern Barents shelf break region. However, as a main pathway for Atlantic Water, the Barents shelf break region may have a large impact on the heat balance, water properties, and ice formation in the Arctic Ocean. It is necessary to determine, with available data, the potential impact of tides in this region and determine the need for further process studies and more sophisticated models of this region. Therefore, we combine the analytical models presented in section 2 with the 2-D and 3-D models discussed in this chapter to examine the spatial variability of tide induced mixing and the importance of the Barents shelf break region in this process. Due to the similarity in both the topographic and hydrographic structure, the mixing processes affecting the Yermak Plateau and Barents shelf break region should be similar. Therefore, the above observations will be used to validate the models.

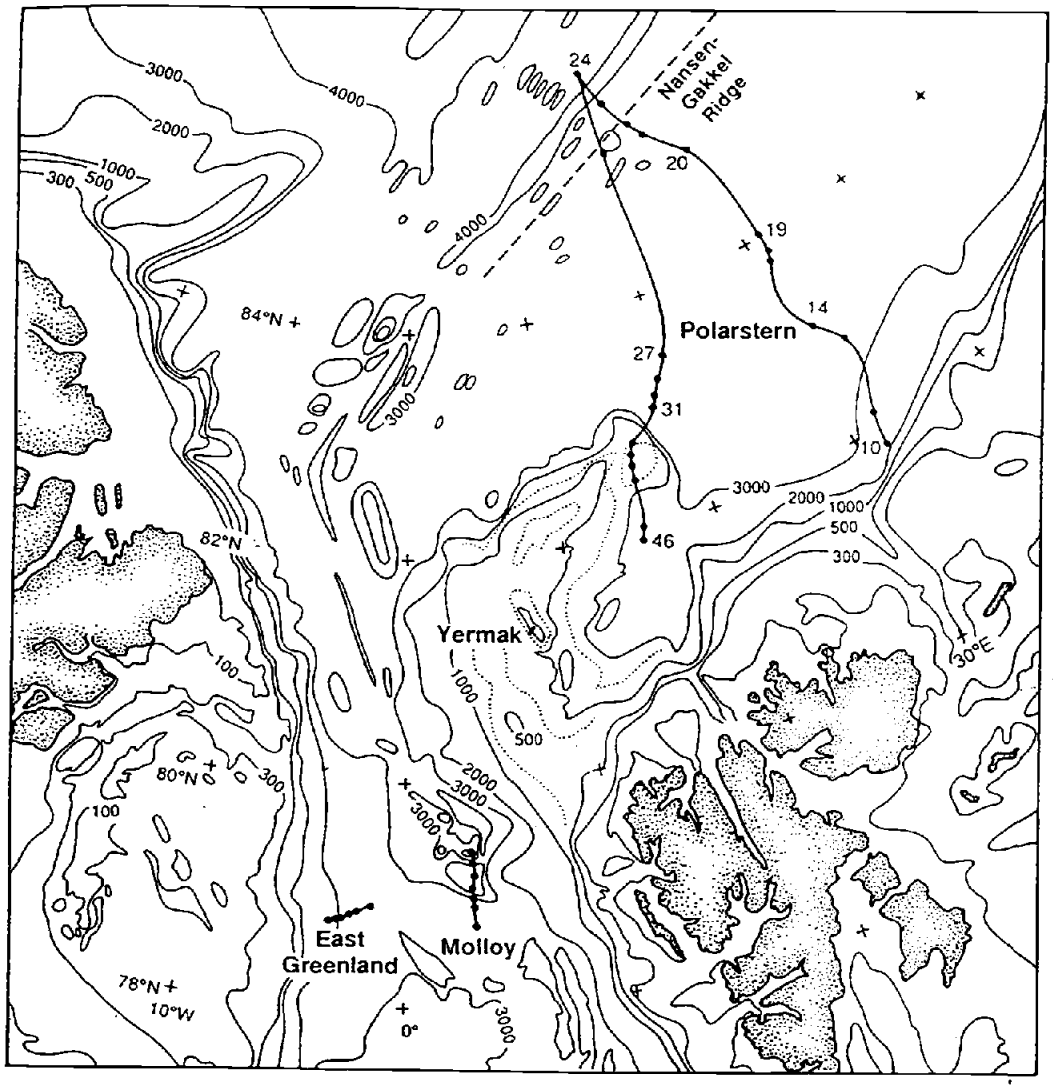

Figure 3.5. The geographical location of the XCP profiles used by *D'Asaro and Morison* [1992]. Depth contours are in meters (from *D'Asaro and Morison* [1992]).

4. RESULTS

4.1 Seabed

To examine spatial variability in tide-generated bottom stress, the Simpson-Hunter parameter, S, defined by equation 2.17 was calculated for the eastern Arctic. For this calculation, both the bathymetry and velocity values were obtained from *Kowalik and Proshutinsky's* [1994] Arctic barotropic tidal model. Since we are using barotropic velocities, the bottom velocity is the same as the velocity of the rest of the water column, $U_b = U$. A characteristic value of U was obtained by taking the square root of the sum of squares of the velocity current amplitudes of the 4 major tidal constituents, i.e.,

$$U = [\ amp_u(M_2)^2 + amp_v(M_2)^2 + amp_u(S_2)^2 + amp_v(S_2)^2 + amp_u(K_1)^2 + amp_v(K_1)^2 + amp_u(O_1)^2 + amp_v(O_1)^2\ ]^{1/2}. \quad (4.1)$$

Following the calculations of *Pingree and Griffiths* [1978], a constant value of 0.0025 was used for C_b. *Kowalik and Proshutinsky* [1994] use a C_b value of 0.0026 in their model. A map of S for the eastern Arctic is shown in figure 4.1. The ratio of buoyancy production to energy dissipation falls across contours of h / U^3. Lower S values indicate that the water column is more likely to be well-mixed due to bottom tidal stresses. The lowest values of S occur in the White Sea and around Bear Island but low values also occurs along the northern Barents shelf break. Higher S values occur in the deeper basins where the depth of the water column and weak currents prevent much mixing. Due to the time limitations of this study as well as complications arising from seasonal variability, we did not seek to find S_{crit}, but simply the spatial variability in the mixing potential. As a guide, *Kowalik and Proshutinsky* [1995] identified the location of the tidal front around Bear Island and associated it with a critical value of $S = 1.5$ from *Pingree et al.* [1978]. However, in other regions of the Barents and Kara Seas, this critical value may not represent the frontal boundary. The studies discussed in 2.2.1 have indicated that the critical value for transition between well-mixed water is not a set value. Local physical

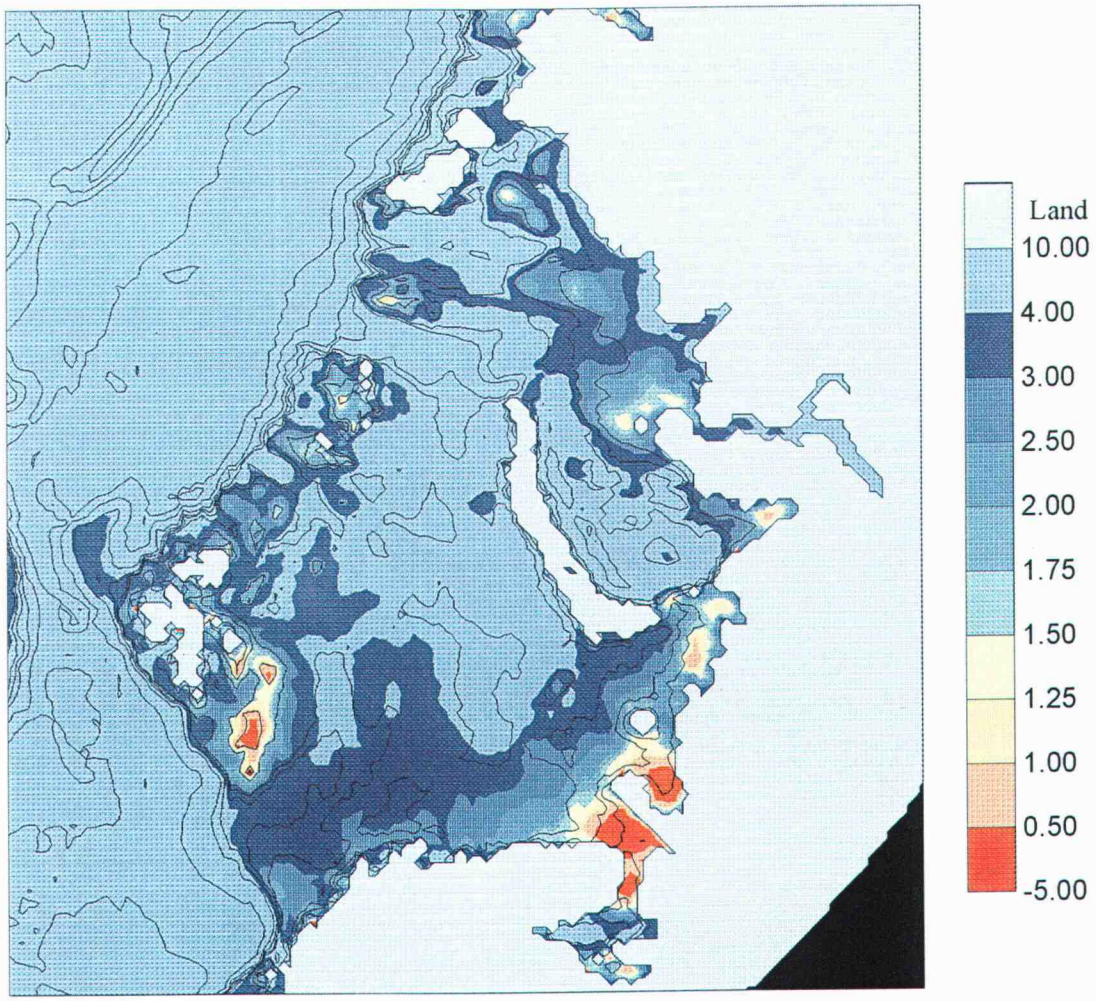

Figure 4.1 Contours of the Simpson-Hunter parameter. Lower values indicate greater mixing.

processes as well as seasonal fluctuations in Q and river runoff must play a key role in determining S_{crit}. *Schumacher et al.* [1979] demonstrated that the fronts in the Bering Sea are similar to those studied around the British Isles; however, there are important differences. In the Bering Sea, the melting and freezing of ice as well river run-off are more important buoyancy source terms than heating. These buoyancy terms will be important in the Kara and Barents Seas as well. The ice may also increase mixing through the addition of stress generated by tidal currents at the ocean-ice. An examination of this process is given in the next section.

4.2 Ice-Ocean Interface

By creating stress at the ice-ocean interface, the interaction between tidal currents and ice in the Kara and Barents Seas can increase the potential for the water column being well-mixed. Instead of stress from one boundary mixing the entire column from the sea-bed to the surface, the addition of ice creates another boundary that can aid in mixing the water column from the surface downward. As shown by equation 2.27, the addition of ice doesn't alter the property that changes in stratification will again take place across the h/U^3 contours. It does, however, increase the value of the critical contour (equation 2.28), expanding the area of well-mixed regions. Therefore, to examine where tidal stresses at the ice-ocean interface may be important, figure 4.1 can again be used to indicate where stratification changes occur. In combination with this, figures 2.5a and 2.5b can be used to determine areas where ice is present in existing areas of strong sea-bed stresses. Large stresses from both the sea-bed and the ice-ocean interface will occur around the shelf break where the tides are strong, assuming that the ice is relatively uncoupled to the underlying ocean.

As explained in section 2.2.2, different types of ice will have different responses to tidal currents. Large tidal currents will not necessarily increase the relative velocity needed to produce the stress a the ice-ocean interface and raise the potential energy of the water column (equations 2.22 and 2.23). In many regions in the eastern Arctic Ocean,

particularly over the continental shelves, ice properties and even ice presence vary seasonally.

As seen in figure 2.5, ice is generally present in the northern Barents shelf break region. In summer, ice tends to be less compact over the northern Barents shelf break and over the Yermak Plateau. In these regions, strong tidal currents during this season might not significantly enhance mixing under the sea ice. In winter, however, the ice is more compact, leading to a larger U_{rel}. The addition of ice would lead to enhanced mixing (raising S_{crit}) in the regions indicated as strong mixing along the northern Barents shelf break.

4.3 Internal Tides

Internal tides are a significant source of diapycnal mixing and possibly one of the main causes of heat transfer from the Atlantic layer to the surface layer, and from there to the ice and atmosphere. Previous small-scale process studies have been unable to determine the significance of this process along the northern Barents Sea shelf break due to limited spatial coverage. In this section, we use analytical and numerical models to examine the spatial distribution of internal tide generation. Mixing and heat fluxes associated with this process are also estimated in order to assess the significance of tides in this region.

4.3.1 *Analytical Models*

As part of our attempt to understand the significance of internal waves in the eastern Arctic, the analytical models of *Sjöberg and Stigebrandt* [1992] (SS92) and *Baines* [1982], described in sections 2.2.3.1 and 2.2.3.2 respectively, were used to examine the spatial variability of internal tide generation. For the SS92 model, the

formulations without and with rotation (referred to as case I and case II, respectively) were examined.

To calculate the energy flux into internal tides due to interaction of barotropic tides with topography, SS92's analytical model was applied to the eastern Arctic using bathymetry and tidal current amplitudes, α, from *Kowalik and Proshutinsky's* [1994] Arctic tidal model. To calculate the energy flux into internal tides using equations 2.14 and 2.16 from section 2.2.3.1, we first defined an N_o following SS92 as

$$N_o^2 = g\,\delta\rho\,(1 - e^{-H/\delta})\,/\,\rho_o H, \qquad 4.2$$

using EUBEX profile 517 (figure 2.4) as a characteristic profile. The characteristic density, ρ_o, was taken to be 1027.5 kg m^{-3}, $\delta\rho = 0.5$, and $\delta = 200$ m.

The energy flux into a grid cell for each mode, '*n*', was estimated by first finding the energy fluxes (in W m^{-1}) at the sides of each grid box (see figure 4.2), using the spherical polar coordinate system of *Kowalik and Proshutinsky's* model output. The energy fluxes in the east-west (x) direction and in the north-south (y) direction were then calculated for each grid cell, converted to W m^{-2} by dividing by the cell length, and then added together to get the grid cell value, i.e.,

$$F_n = \tfrac{1}{2}\,[F_{n,x}(i, j\text{-}1) + F_{n,x}(i, j)]\,/\,\Delta x \;+\; \tfrac{1}{2}\,[F_{n,y}(i\text{-}1, j) + F_{n,y}(i, j)]\,/\,\Delta y. \qquad 4.3$$

For case I, equation 2.48 from section 2.2.3.1 was used to calculate $F_{n,x}$ and $F_{n,y}$, and for case II, equation 2.49 from section 2.2.3.1 was used. In each case, H is taken to be the depth at the lower step, α is taken to be the velocity amplitude at the lower step (normal to the step), and ρ, δ, and N_o are as in equation 4.5 (see figure 2.10 for step illustration). The energy flux values were then converted to a rectilinear grid for plotting purposes.

Sjöberg and Stigebrandt [1992] used the sum of the energy fluxes from the first 10 modes to get a total energy flux. Starting with a barotropic velocity of 0.20 ms^{-1} encountering a step at a depth of 500 m, figure 4.3 demonstrates how well 10 modes mimic the velocity solution at the step (at $x = 0$). The velocity is near zero velocity below

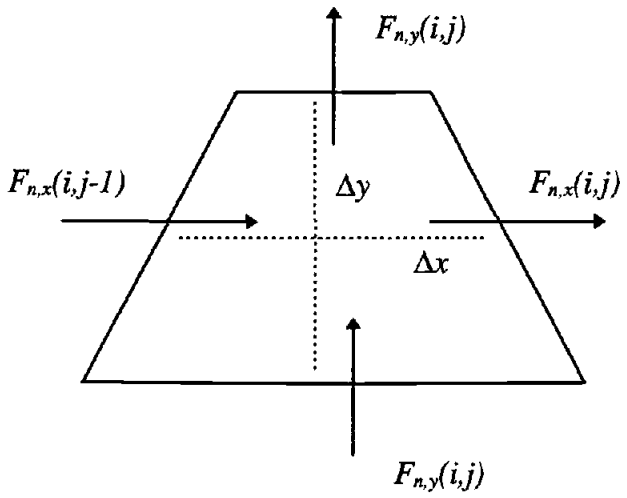

Figure 4.2 Grid for energy flux calculations.

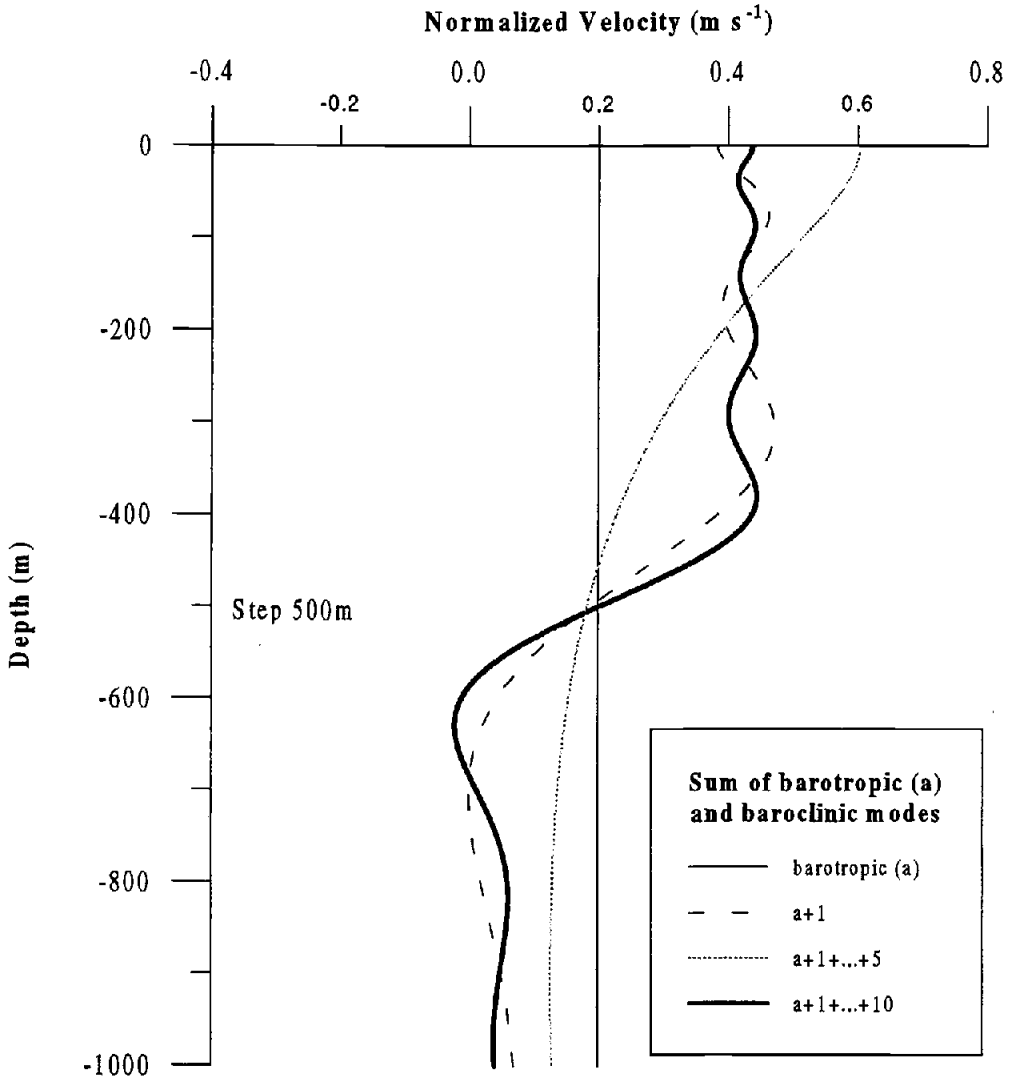

Figure 4.3 Velocity solution at the step ($x = 0$) based on equation 2.36. The velocity has been normalized. The total depth is 1000 m and the top of the step is at 500 m.

the top of step and increases to 0.40 ms^{-1} above $z = 500$. The main properties of the field are explained by the first 10 modes. In energy calculations, modes higher than ten provide negligible energy.

Energy fluxes for the 2 major semidiurnal constituents, M_2 and S_2, were calculated. The energy flux into internal tides from the first ten modes based on the S_2 tide for case I and case II are shown in figures 4.4a and 4.4b, respectively. Similarly, the energy flux based on the M_2 tide is shown in figures 4.5a and 4.5b. In figures 4.4b and 4.5b, the critical latitude for each constituent is indicated. The SS92 model with rotation does not allow for internal tide generation above a constituent's critical latitude (see table 2.1). The total energy flux, a sum of the energy fluxes from the first ten modes of S_2 and the first ten modes of M_2, for case I and case II, are shown in figure 4.6a and 4.6b. The shelf break region along the Barents, Kara, and Laptev Seas stands out as an area of strong internal tide generation. To look at where generation was largest, we divided the Arctic region according into four depth ranges: shelf (0-200 m), upper slope (200-1000 m), lower slope (1000-3000 m), and deep (> 3000 m). Energy fluxes, based on the total energy fluxes shown in figures 4.6a and b, for these different depths ranges above 71° N latitude are given in table 4.1 for both cases. The SS92 model indicates that the upper slope region is the highest generation site. Assuming, like SS92, that most of the internal wave energy is dissipated in or near the grid box in which it is generated, the highest dissipation rates will also most likely occur over the upper slope.

To estimate diapycnal diffusivities in the region, the total energy flux in each grid box was assumed to dissipate within the same grid box over a 100 m thick pycnocline. A dissipation rate (W kg^{-1}) was found using

$$\varepsilon = F_n / (\rho * \text{pycnocline thickness}) . \qquad 4.4$$

The vertical diffusivity at each grid box was then found using

$$K_v = 0.2\, \varepsilon / N^2, \qquad 4.5$$

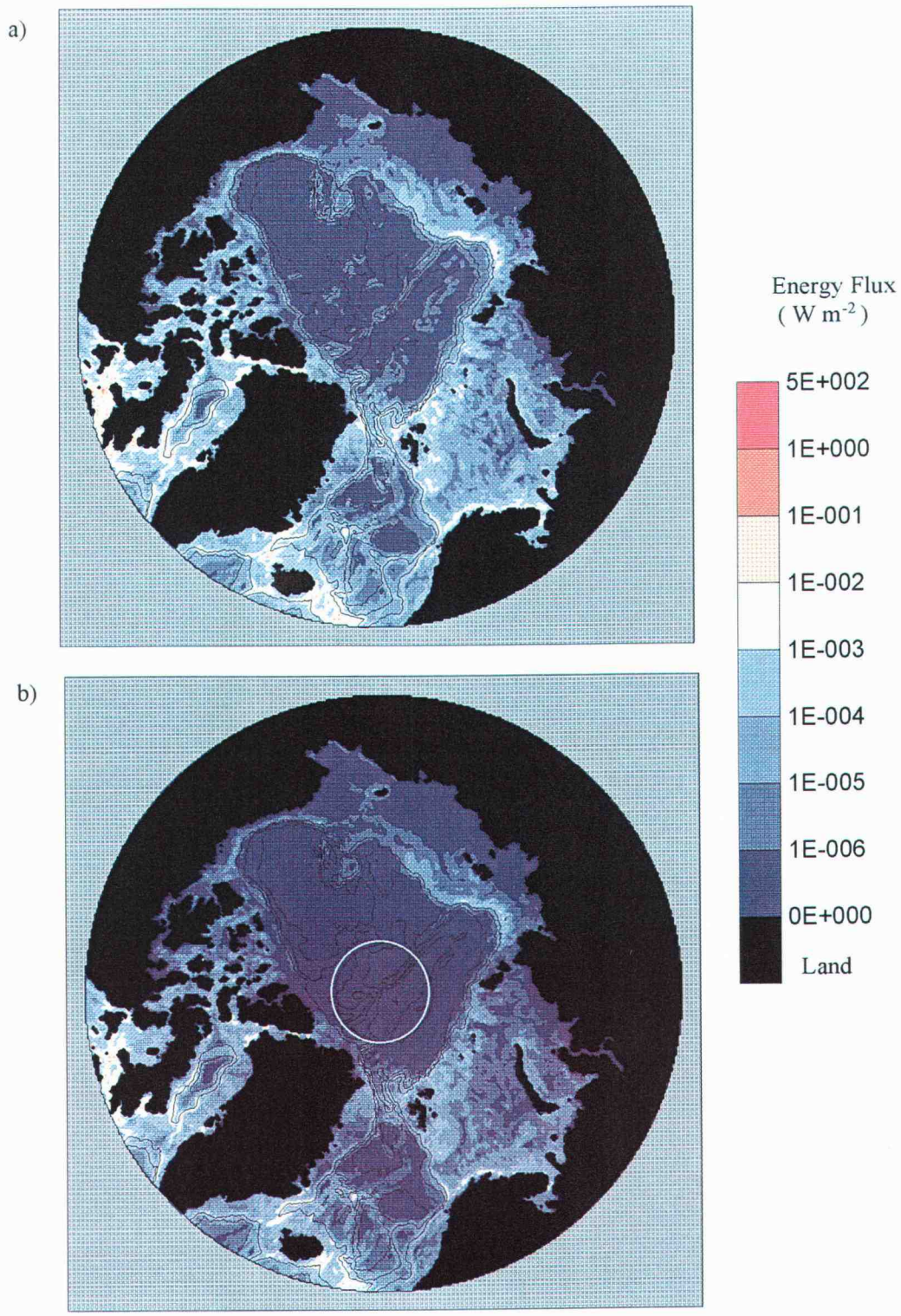

Figure 4.4 The energy flux (W m^{-2}) into internal tides from the S_2 tide based on the first 10 modes for (a) case I (no rotation) and (b) case II (rotation). The white line in figure (b) indicates the critical latitude for the S_2 tide.

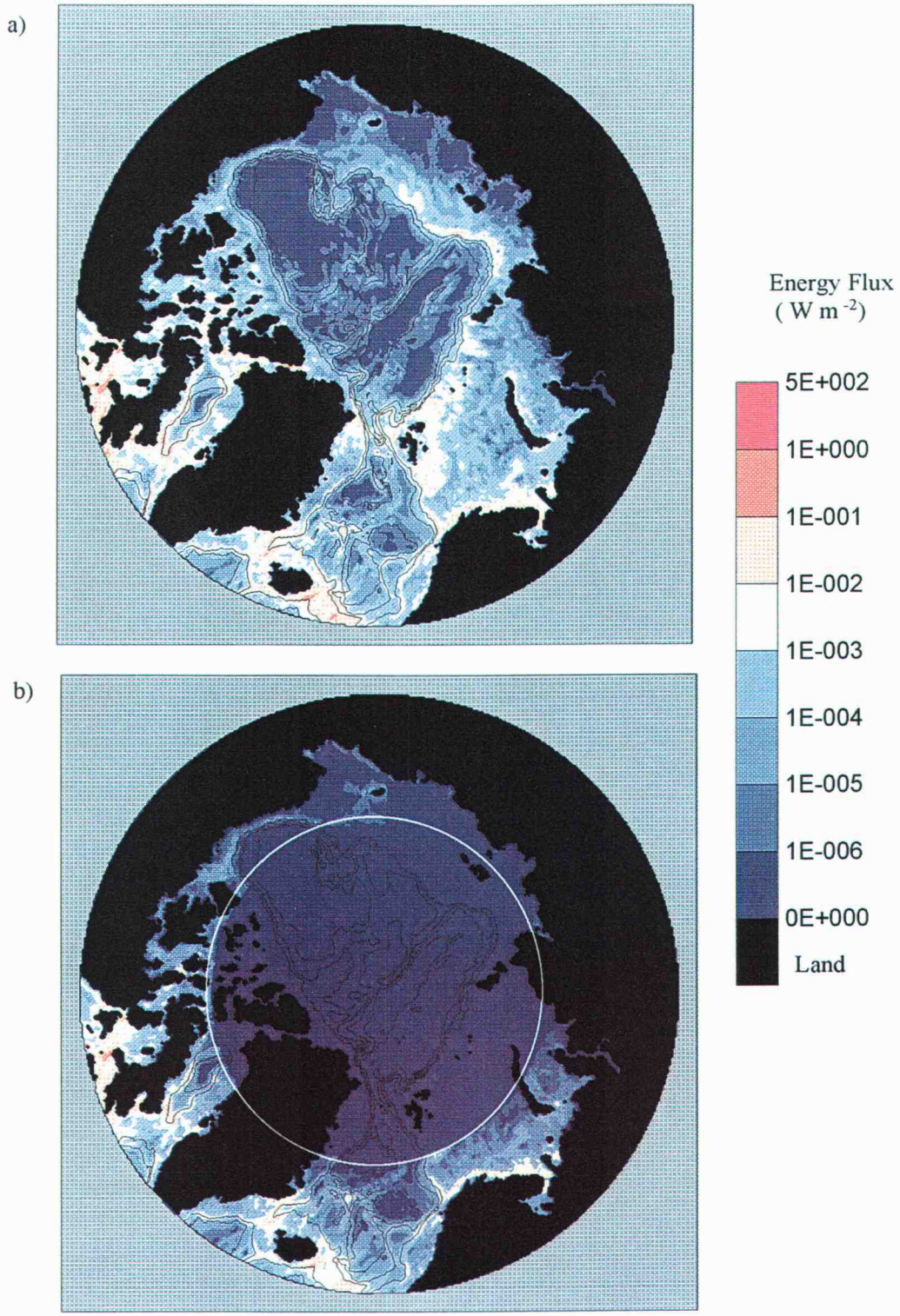

Figure 4.5 The energy flux (W m^{-2}) into internal tides from the M_2 tide based on the first 10 modes for (a) case I (no rotation) and (b) case II (rotation). The white line in figure (b) indicates the critical latitude for the M_2 tide.

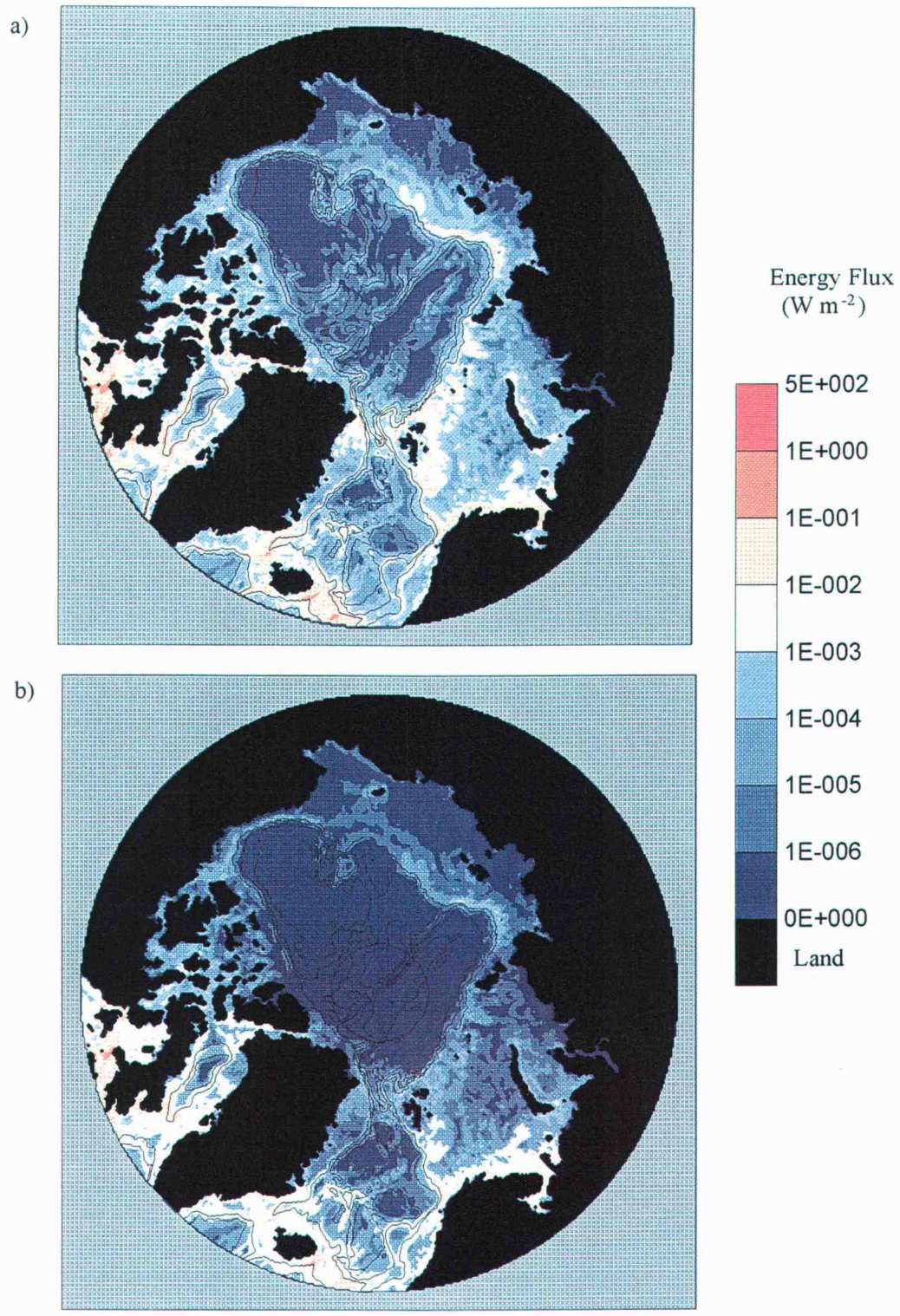

Figure 4.6 The energy flux (W m^{-2}) into internal tides from the sum of the M_2 and S_2 tide based on the first 10 modes for (a) case I (no rotation) and (b) case II (rotation).

Depth Region		Energy Flux (no rotation)	Energy Flux (rotation)
Shelf	(0 -200 m)	1.41×10^{-3}	1.43×10^{-4}
Upper Slope	(200-1000 m)	1.98×10^{-3}	1.48×10^{-4}
Lower Slope	(1000-3000 m)	5.31×10^{-4}	3.36×10^{-5}
Deep	(> 3000 m)	5.25×10^{-4}	9.61×10^{-7}

Table 4.1. Mean energy flux (W m^{-2}) into internal tides from the $S_2 + M_2$ tide (first 10 modes) categorized by the depth of the region for both the case with rotation and without rotation.

where 0.2 is the mixing efficiency parameter [*Osborn*, 1980; *Oakey*, 1982] and N was taken to be 3 cph (5.23 x10^{-3} s^{-1}) based on EUBEX profile 517 (figure 2.4). Maps of K_v for case I and II are shown in figure 4.7. Large variations in K_v across the shelf break region are visible in this figure.

Heat fluxes were estimated from the vertical diffusivities using

$$F_H = \rho_o c_p K_v \, dT/dz, \qquad 4.6$$

where ρ_o =1027.5 kg m^{-3}, c_p = 4.2 x 10^3 J kg^{-1} K^{-1}, and dT/dz was taken to be 0.03 °C m^{-1}. Heat flux maps for the two cases are shown in figure 4.8.

Several cross sections were examined across both the Yermak Plateau and northern Barents shelf breaks. Locations are indicated on figure 4.9. Figure 4.10 shows the cross slope variations of K_v and F_H over the Yermak Plateau (for both cases). Figure 4.11 shows the cross slope variations of K_v and F_H over the northern Barents slope (for both cases). The huge differences between case I and case II are due to the lack of M_2 tide in the rotation case. The barotropic M_2 tide is the largest tidal constituent over the Barents shelf break. Therefore, if the M_2 tide is excluded from being a generating mechanism, the energy flux in a region will be dramatically reduced.

The analytical model of *Baines* [1982] was also applied to this region using equations 2.64-2.66. The formulation of the *Baines* [1982] model prevents grid by grid energy flux calculations like the SS92 model. The entire shelf break region must be treated as one generation area. Therefore, the *Baines* [1982] model was used to examine internal tide generation across the shelf break at transects indicated on figure 4.9. To apply *Baines'* model, the slopes shown in 4.10 and 4.11 were linearized (figure 4.12). Tidal velocities at the top of the shelf were taken from the model of *Kowalik and Proshutinsky* [1994]. Eubex drop 517 was used to determine g', ρ_o, d, and N. The model does not allow for generation due to tidal constituents above their critical latitude, therefore only the S_2 tidal velocity was used. When calculating the energy fluxes in the *Baines* [1982] model, if the ratio of the pycnocline depth (d) to the shelf depth (h_L) is large enough (~1), interfacial modes will be generated. The total energy flux will be a sum of

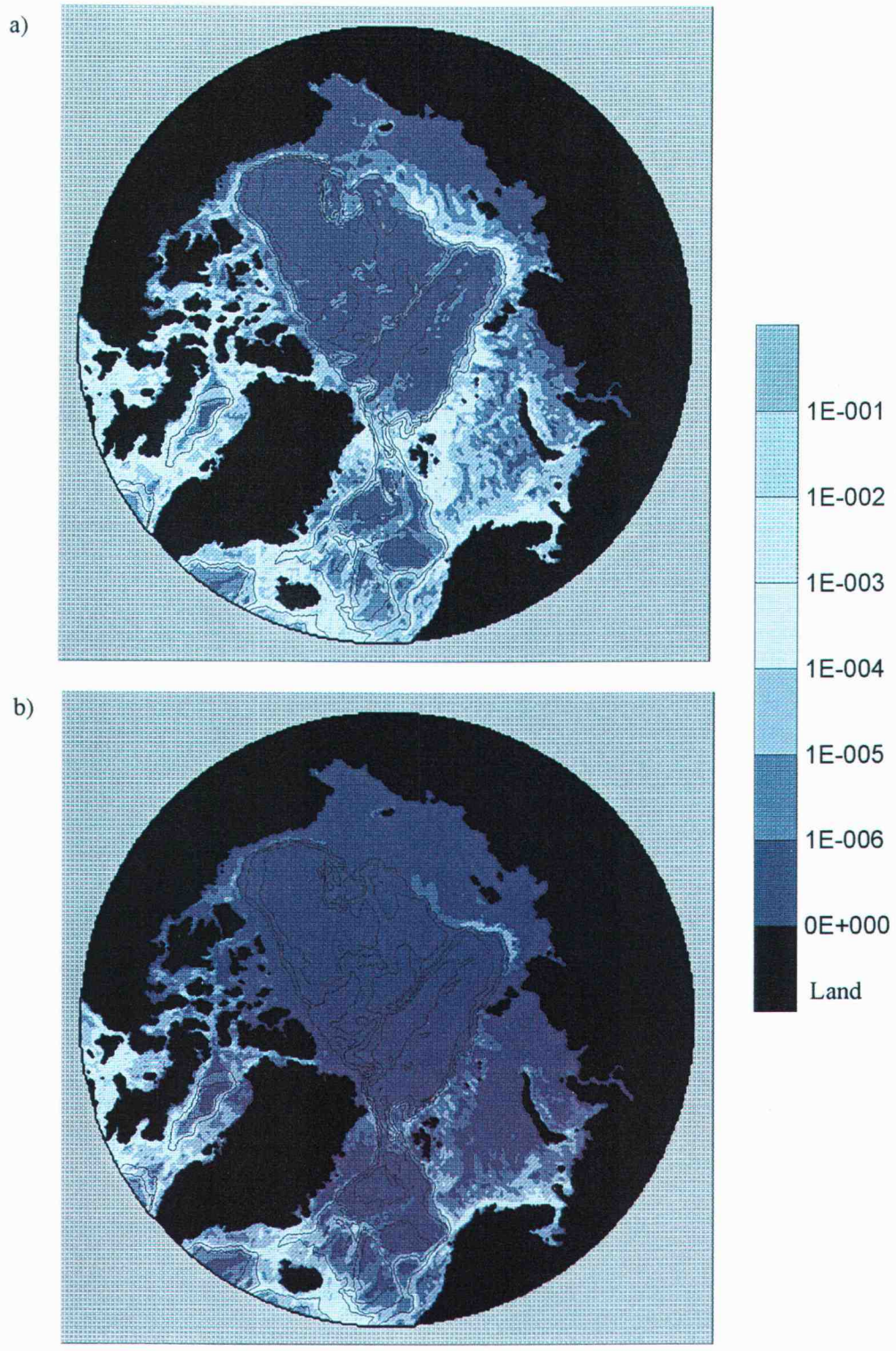

Figure 4.7 Vertical diffusivities (m^2s^{-1}) calculated from energy fluxes (F_n) for (a) case I and (b) case II.

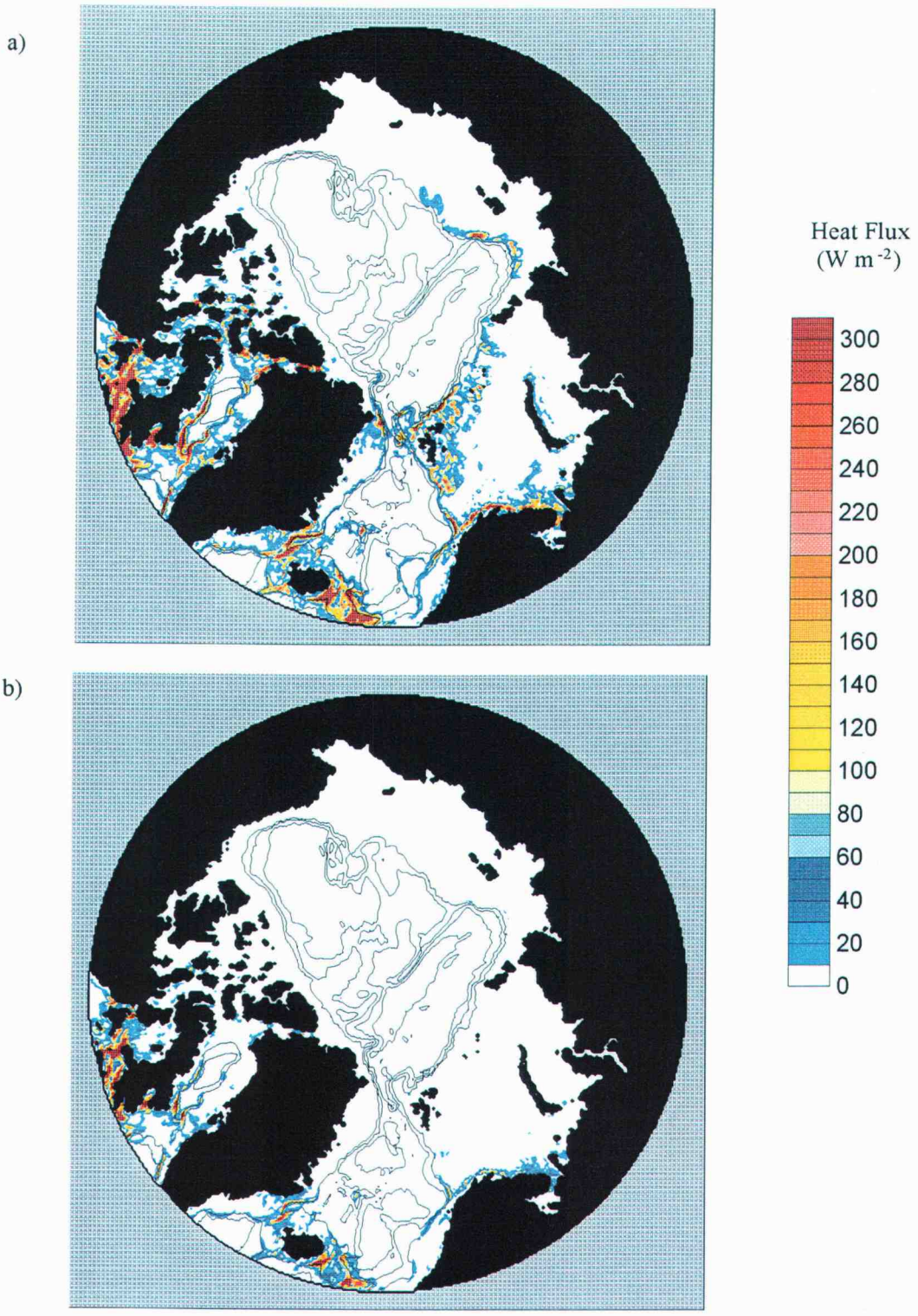

Figure 4.8 Heat fluxes (W m^{-2}) calculated from diffusivities for (a) case I and (b) case II.

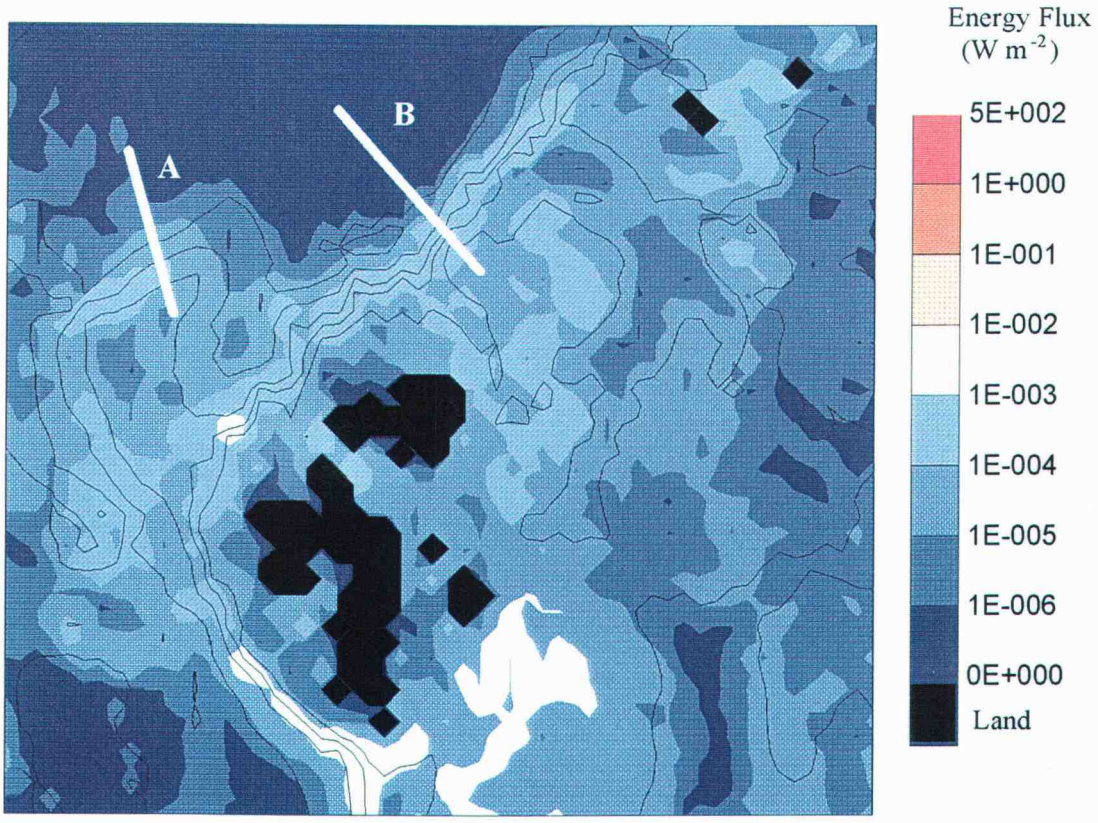

Figure 4.9. Map of the energy flux into internal tides from the sum of the M_2 and S_2 tide based on the first 10 modes for case II showing the location of transects A and B.

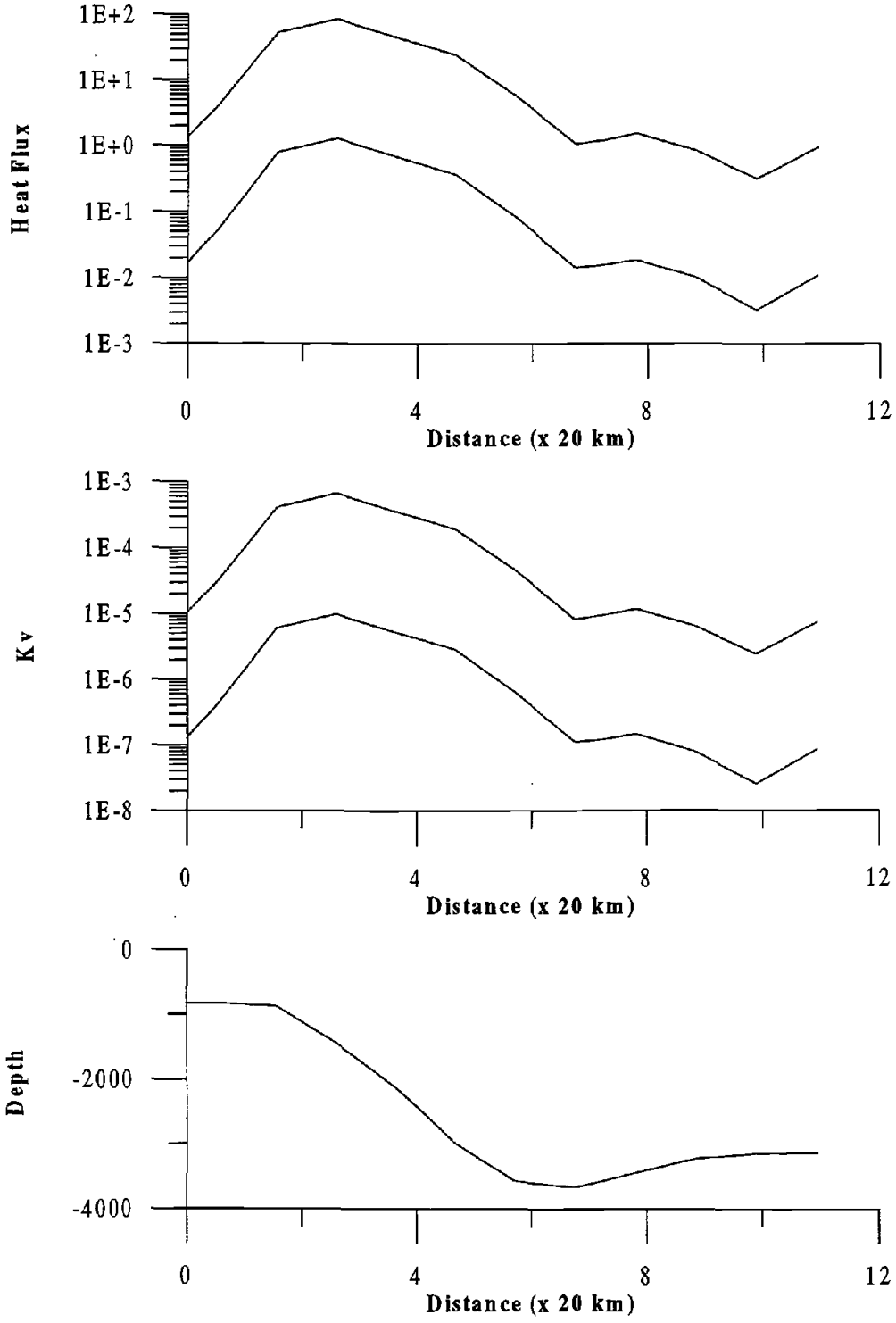

4.10. Plots of (a) heat flux (W m^{-2}), (b) vertical diffusivity (m^2s^{-1}), and (c) bottom depth (m) for transect A.

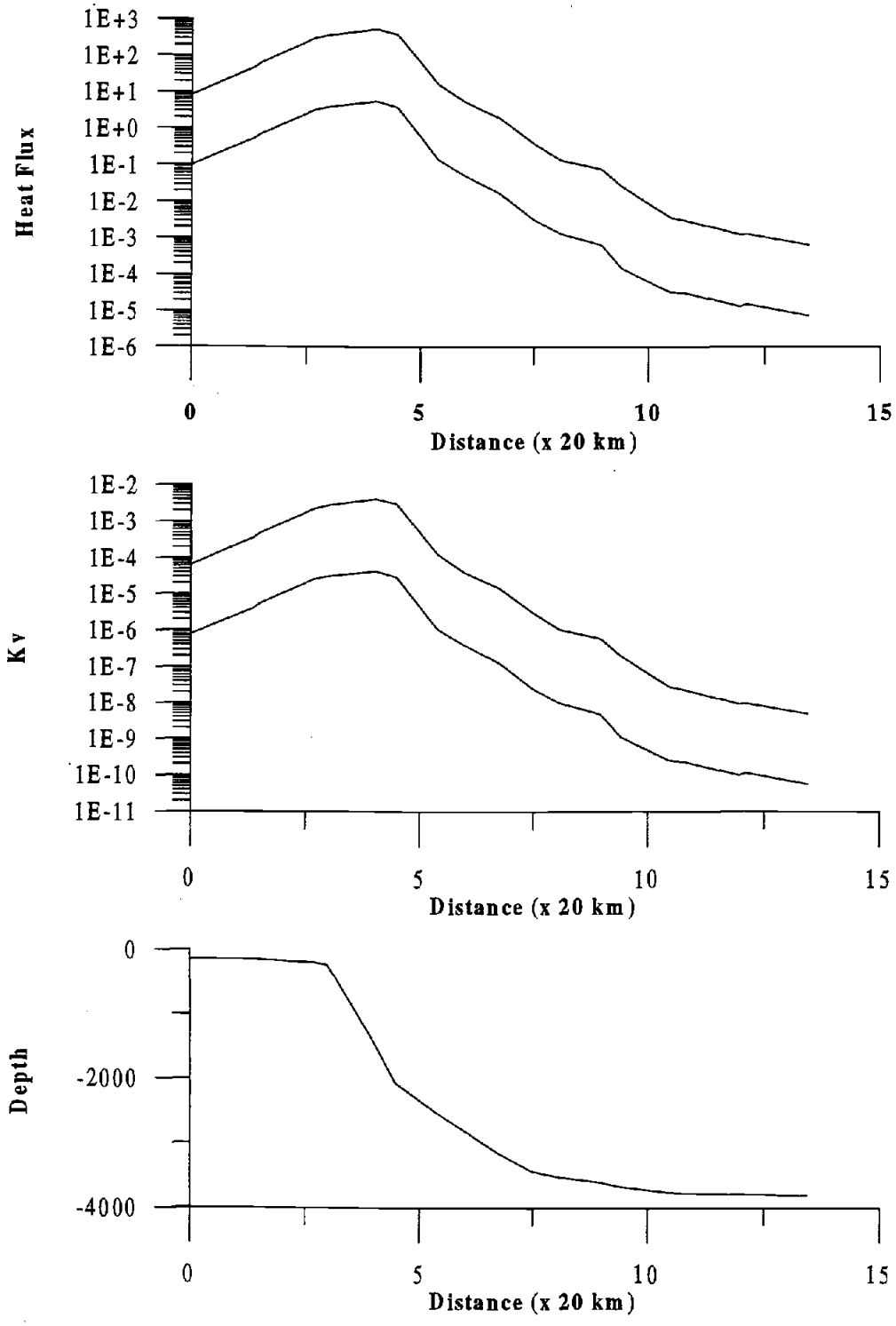

Figure 4.11. Plots of (a) heat flux (W m^{-2}), (b) vertical diffusivity (m^2s^{-1}), and (c) bottom depth (m) for transect B.

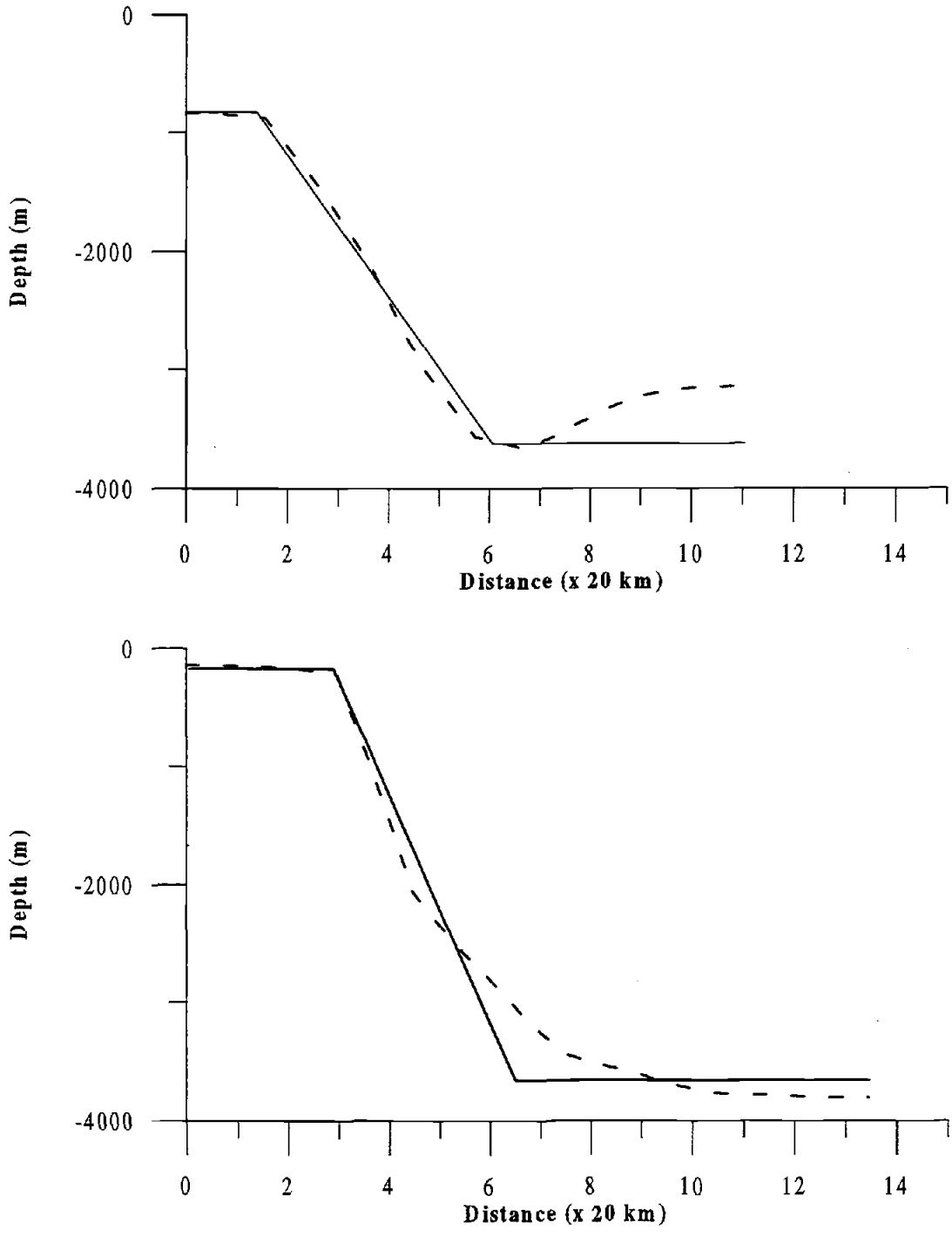

Figure 4.12. Dashed lines indicate bottom topography for (a) transect A and (b) transect B. Solid lines represent linearized slope.

the energy fluxes into the shoreward (equation 2.64) and seaward (equation 2.65) interfacial modes plus the seaward (equation 2.66) energy flux in the continuum modes. Over the Yermak Plateau (cross section A), the deep shelf (800 m) (figure 4.12a) did not excite interfacial waves. Using an S_2 tidal velocity of 0.015 ms^{-1} at the top of the shelf, the energy flux into the continuum was 11.9 W m^{-1} (table 4.2). The same calculations were done for the Barents shelf break region (cross section B in figure 4.9). The S_2 tidal velocity at the top of the slope was 0.063 ms^{-1}. The top of the shelf (150 m) was high enough to excite interfacial modes. The total energy flux (8.8 W m^{-1}) was lower than the energy flux into internal tides seen in cross section A (table 4.2). The different energy fluxes in the two regions is a result primarily of the differences in mass fluxes ($q = h \times u$) since the energy flux is dependent on q^2 (equations 2.64-2.66). Table 4.2 gives the total energy fluxes into internal tides from the S_2 tide for the *Baines* [1982] and SS92 models for both transects. The SS92 total (in W m^{-1}) was obtained by integrating over the slope. The energy fluxes in both regions are lower than most of the global estimates shown in table 2 of *Baines* [1982], however, these values were calculated from the M_2 tide. We expect the M_2 tide to generate a significant amount of internal tide energy even above the critical latitude, although the two analytical models prevent this calculation.

4.3.2 *Parsons Model Results*

As mentioned in section 3.3, the baroclinic model of *Parsons* [1995] contains annually forced winds and the surface temperature and salinity are restored to annual Levitus temperature (T) and salinity (S) fields every 30 days. The model does not contain ice. However, even with these limitations, the inclusion of the M_2 tide in the baroclinic model produced processes associated with tidal mixing that appear to be realistic and oceanographically significant. *Parsons* [1995] found that the inclusion of the M_2 tide increased mixing throughout the Barents Sea and brought the model T and S fields and volume transports closer to observations. In this study, we are primarily interested in the

ENERGY FLUX:	BAINES				SS92
	Interfacial Shoreward	Interfacial Seaward	Continuous Seaward	Total ($W\ m^{-1}$)	Total ($W\ m^{-1}$)
Yermak Plateau	0.0	0.0	11.9	11.9	7.4
Barents Sea	1.7	3.1	4.0	8.8	27.9

Table 4.2. Energy flux ($W\ m^{-1}$) into internal tides calculated using both the *Baines* [1982] and the SS92 method for transects A (Yermak Plateau) and B (Barents Sea) shown in figure 4.9.

spatial distribution of internal tides. Model T, S, and horizontal velocity (u, v) fields were therefore used to examine the baroclinic M_2 wave field and the mixing associated with it.

To examine the shear produced by the M_2 tide in the model, the horizontal shear terms ($\partial u/\partial z$) and ($\partial v/\partial z$) are found from model velocities using

$$\partial u/\partial z = (u_m - u_n)/ (D_m - D_n), \qquad 4.7a$$

and

$$\partial v/\partial z = (v_m - v_n)/ (D_m - D_n), \qquad 4.7b$$

where u and v are the horizontal velocity components D represents the mid-depth of the layers (listed in table 3.1). The shear, S, between model layers n and m, where $m = n + 1$ was then calculated at every grid point and time step using the following equation,

$$S_{nm} = ((\partial u/\partial z)^2 + (\partial v/\partial z)^2)^{1/2}. \qquad 4.8$$

A mean shear value, $\langle S_{nm} \rangle$, was obtained by averaging S_{nm} over 48 time steps (approximately one M_2 tidal cycle). Contour maps of shear between levels are shown in figure 4.13. The highest shears occur around Bear Island, the northern slopes of the Kara and Barents Seas, and near the White Sea. High shear values near the shelf break can been seen as far down as levels (n, m) = (5, 6). A cross section of the northern Barents shelf break, shown in 4.14, exhibits sharp increases in shear from less than $0.001 s^{-1}$ off the shelf to near $0.015\ s^{-1}$ on the shelf between layers 2 and 3 (45 m) and $0.008\ s^{-1}$ between layers 3 and 4 (71 m). The shear, $\langle S_{nm} \rangle$, is composed of both shear due to baroclinic tides as well as shear due to background currents. Background shear was found by first averaging the u and v velocities over the entire record (500 time steps $\approx$ 10 tidal cycles) to get $\overline{u}$ and $\overline{v}$. The shear was then calculated as in 4.7 and 4.8, using $\overline{u}$ and $\overline{v}$ instead of u and v. The background shear is always much smaller than the shear shown in figure 4.13, i.e., most of the model shear is associated with the M_2 baroclinic tide.

To look at the amount of turbulence associated with the model shears, a characteristic gradient Richardson number, Ri^*, was calculated between layers using

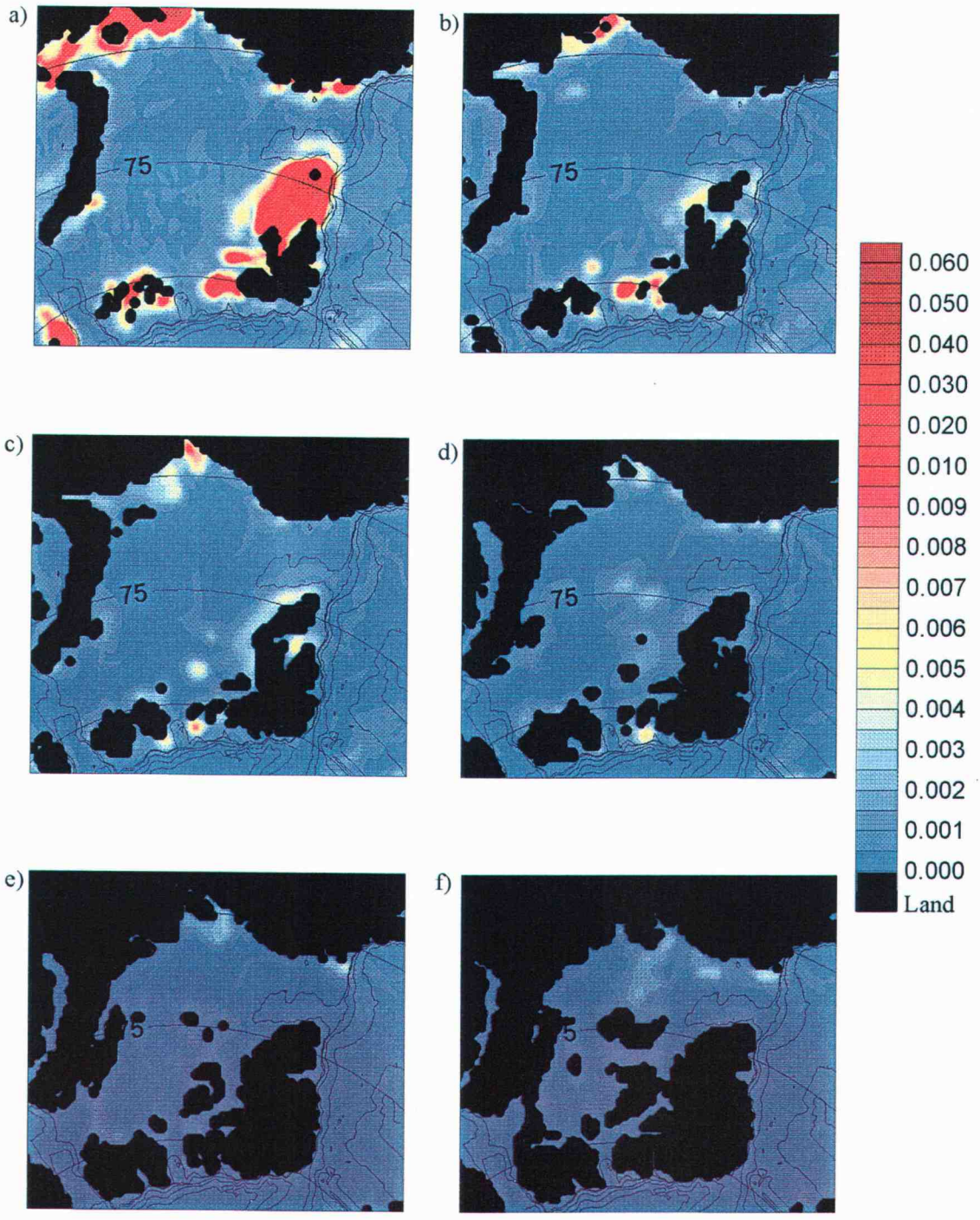

Figure 4.13. Maps of shear (s^{-1}) between layers (a)1 and 2, (b) 2 and 3, (c) 3 and 4, (d) 4 and 5, (e) 5 and 6, and (f) 6 and 7.

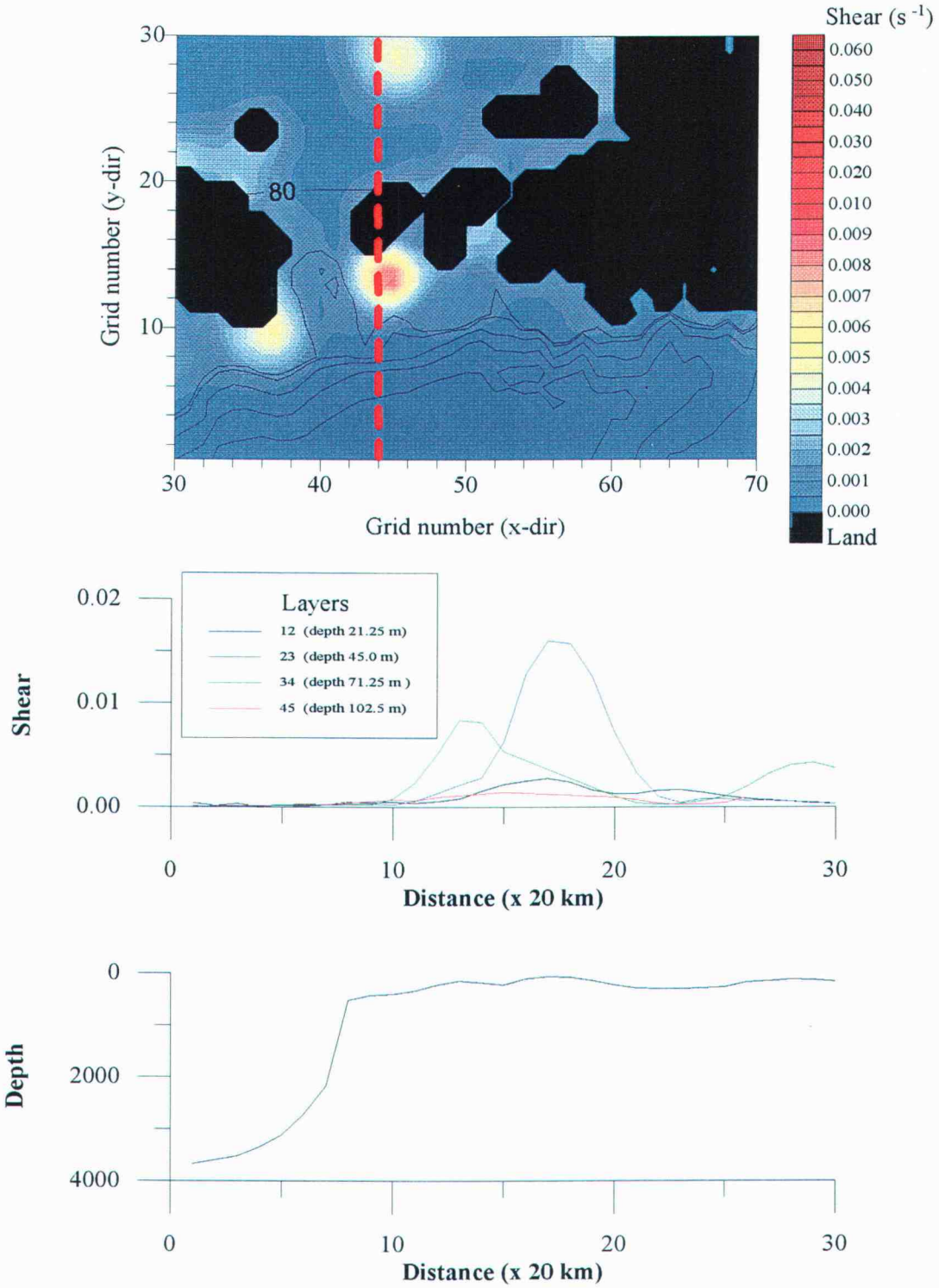

Figure 4.14. (a) Map of shear (s^{-1}) between layers 3 and 4. Red dashed line indicates transect used to show cross slope variation in layer shears in (b). Topography is shown in (c).

$$Ri^*_{nm} = \langle N_{nm} \rangle^2 / \langle S_{nm} \rangle^2, \qquad 4.9$$

where $\langle N_{nm} \rangle$ is the buoyancy frequency calculated from average layer T and S. Maps of Ri^*_{nm} between consecutive layers for $n = 1,\ldots, 6$ are shown in figure 4.15. Richardson numbers are low along the shelf break region. These low Richardson numbers extend down to level Ri_{45}.

To examine the source of low Richardson numbers over the northern slopes of the Barents Sea, time series of velocities between layers were examined. Points both on and off the slope, indicated in figures 4.16a and 4.16b, were investigated. The times series of cross slope velocity (figures 4.17a and 4.18a) near the deeper water (points A and D on figure 4.16) show barotropic signals. Towards the upper slopes, the baroclinicity in the signal increases (figures 4.17b and figure 4.18b). On the upper slopes (points C and F), the velocity time series (figures 4.17c and 4.18c) show downward phase propagation of the internal tide, indicating that the high shear and associated turbulence in this region is due to the bottom generation of the baroclinic M_2 tide. In the model, these waves are dissipated over the slope and are not seen to propagate into the deeper ocean. The change from purely barotropic to clearly baroclinic regimes occurs in a short cross-slope distance, less than 40 km.

The generation of the M_2 baroclinic tide near the shelf break region in the model is a critical finding. The northern Barents Sea shelf break region is north of the M_2 critical latitude (table 2.1). As mentioned previously, the analytical models are not able to calculate energy fluxes into internal tides north of the tidal constituents critical latitude. The finding that large shears related to the M_2 internal tide occur in this region suggest that the analytical models will underestimate the amount of energy input into the internal tides and, therefore, estimates of mixing will also be lower than expected.

As mentioned in section 3.3, a Richardson-number-based vertical mixing scheme, defined by equations (3.4) and (3.5), was used in the model to determine the viscosity and diffusivity coefficients. To examine the model diffusivities, equation (3.5) was calculated between layers, i.e.,

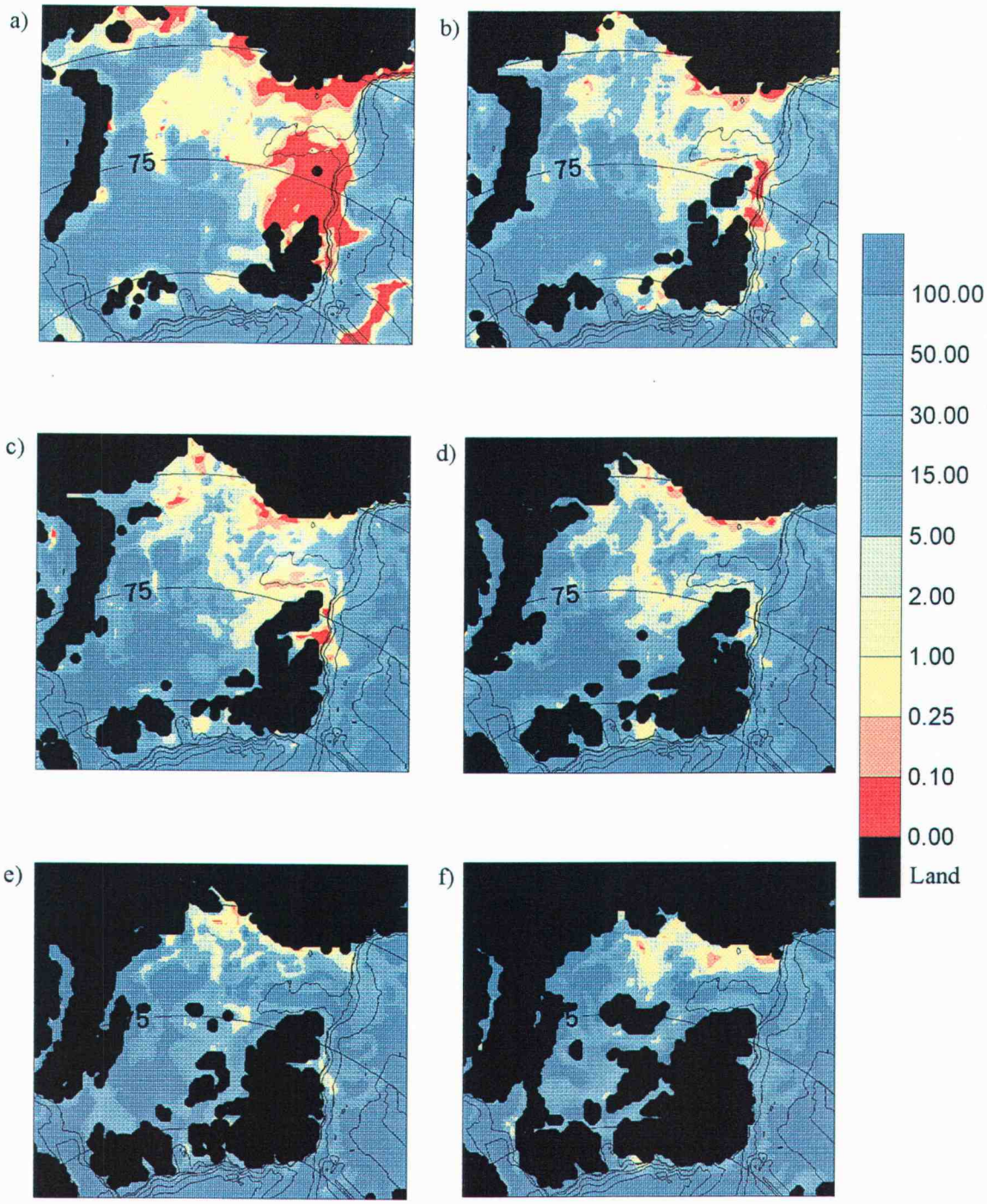

Figure 4.15. Maps of Richardson numbers between layers (a)1 and 2, (b) 2 and 3, (c) 3 and 4, (d) 4 and 5, (e) 5 and 6, and (f) 6 and 7.

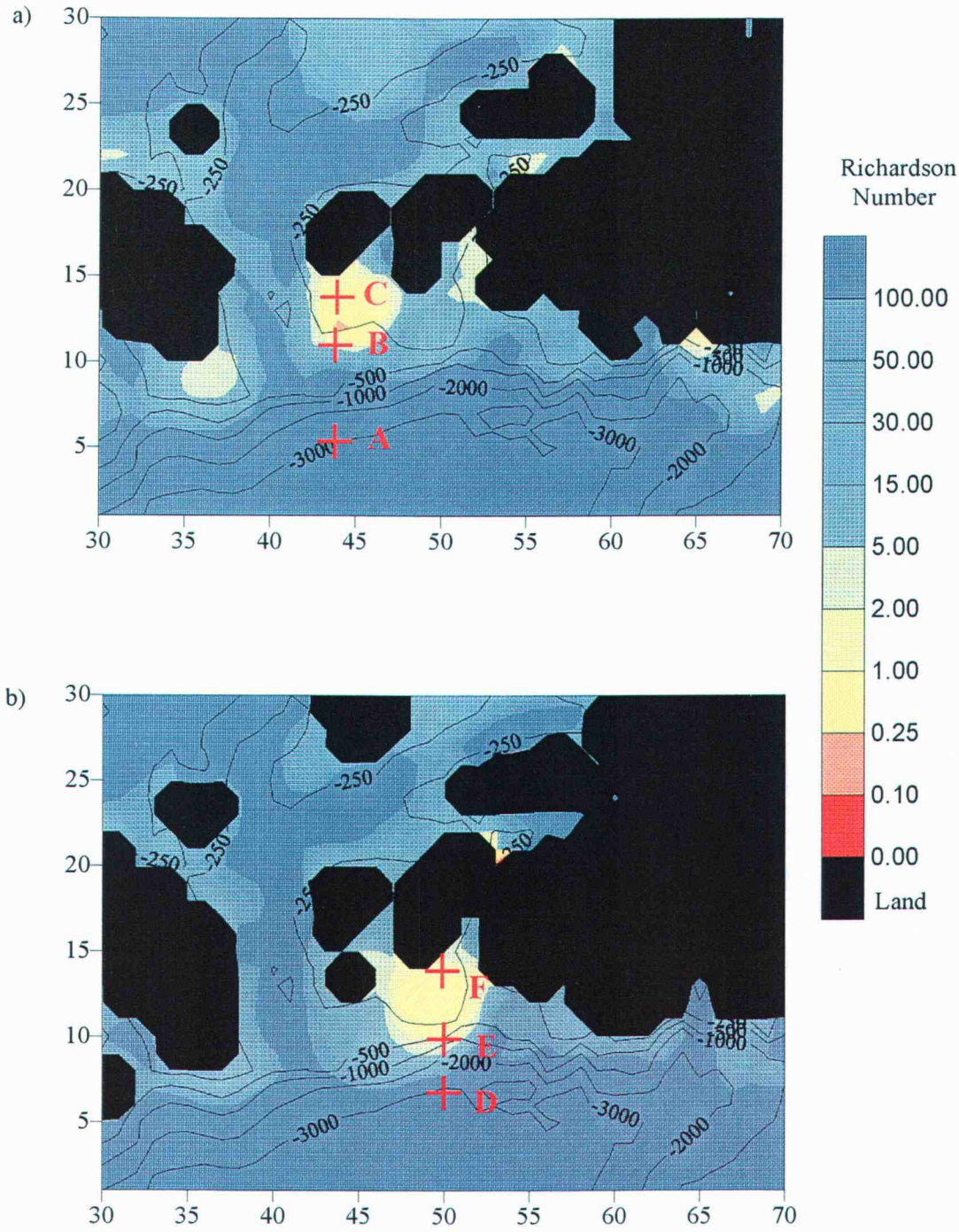

Figure 4.16. Maps of Richardson numbers between layers (a) 3 and 4, (b) 4 and 5.

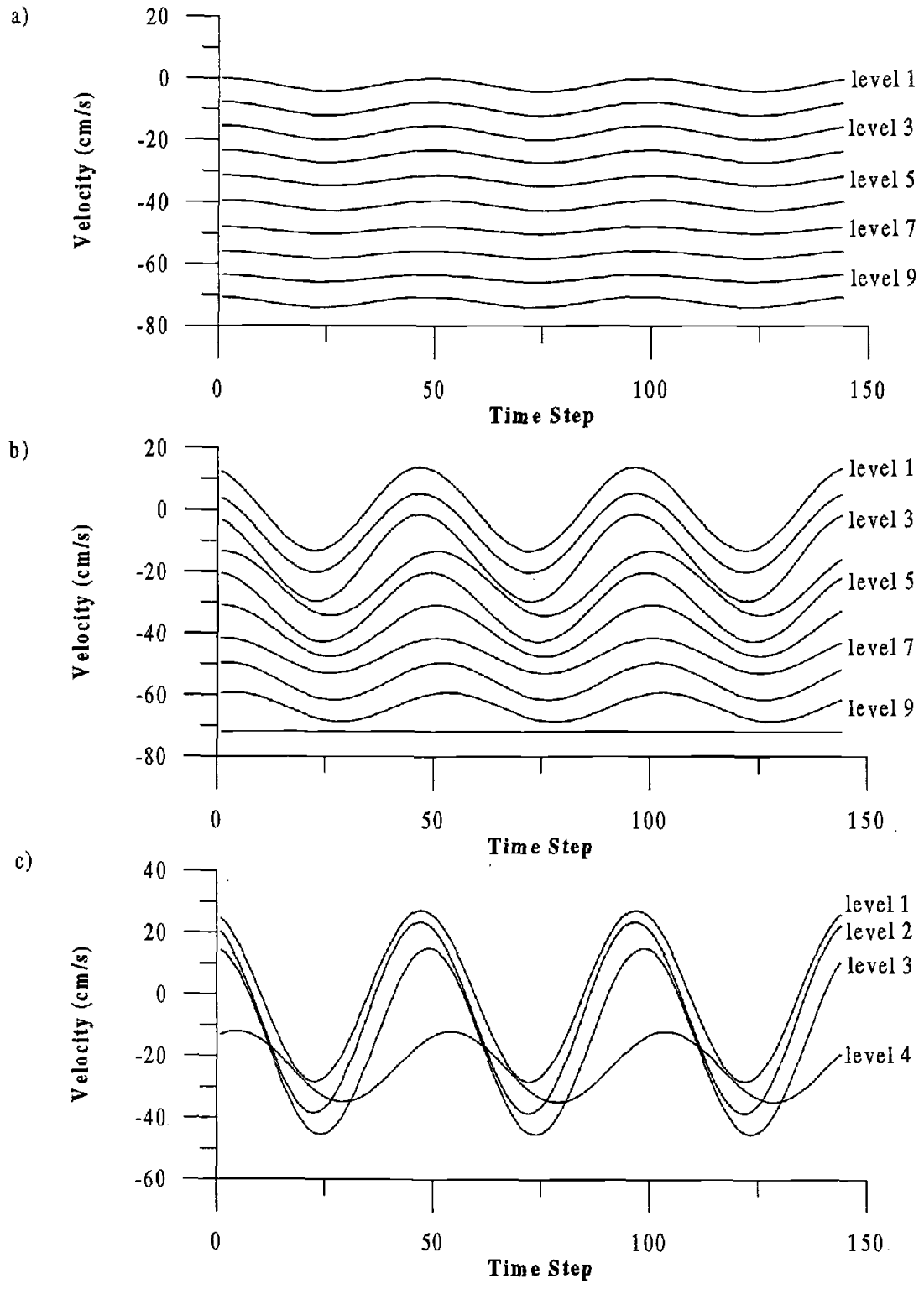

Figure 4.17. Velocity time series (cm s^{-1}) for points (a) A, (b) B, and (c) C shown on figure 4.16a.

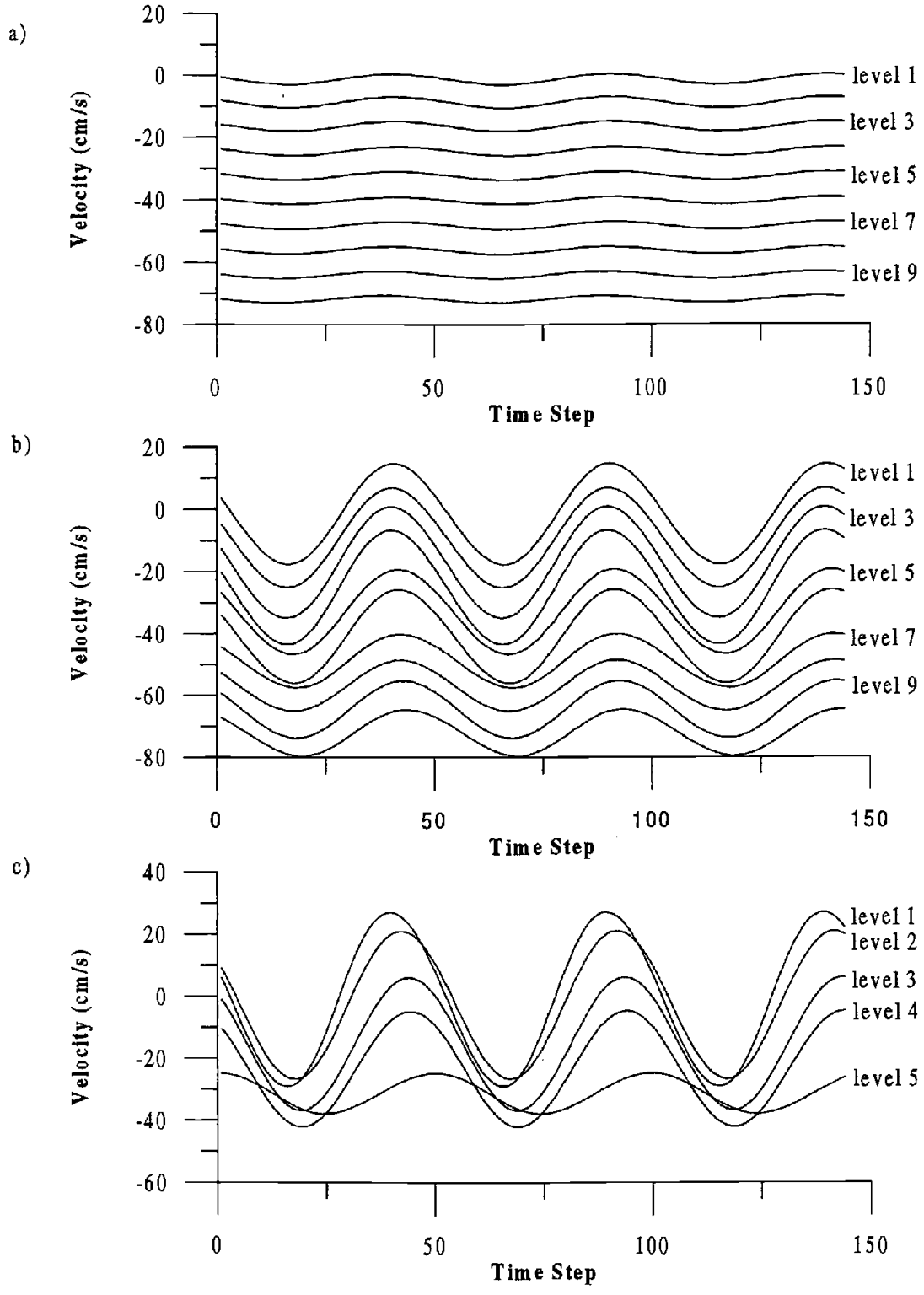

Figure 4.18. Velocity time series (cm s^{-1}) for points (a) D, (b) E, and (c) F shown on figure 4.16b.

$$K_{v,\,nm} = K_{vo} / (1 + (3.3\, Ri_{nm}))^{1/2}. \qquad 4.10$$

where

$$Ri_{nm} = N^2_{nm} / S^2_{nm}. \qquad 4.11$$

A mean value of the vertical diffusivities between layers, $\langle K_{v,nm} \rangle$, was then obtained by averaging over 48 time steps (one M_2 tidal period). Maps of $\langle K_{v,nm} \rangle$ for n=1,...,6 are shown in figure 4.19.

Heat fluxes between model layers, $F_{H,nm}$, were estimated using

$$F_{H,nm} = \rho\, c_p\, \langle K_{v,nm} \rangle\, (\overline{T}_m - \overline{T}_n)/(D_m - D_n), \qquad 4.12$$

where $\rho = 1027.5$ kg m^{-3}, $c_p = 4200.0$ J kg^{-1} K^{-1}, and $\overline{T}_m$ and $\overline{T}_n$ are average layer temperatures (°C). Figure 4.20 shows the heat fluxes for levels n=1,..., 6.

Diffusivities and heat fluxes are clearly associated with topography. Looking at the points shown on figure 4.16a, the vertical diffusivity, $K_{v,34}$, changes from 3 x 10^{-3} m^{2}s^{-1} to 2 x 10^{-7} m^{2}s^{-1} in 54 km (figure 4.21). For the cross section shown figure 4.16b, similar ranges for $K_{v,45}$ exist and are shown in figure 4.21. In general, across the shelf break in the northern Barents Sea, vertical diffusivities are highest on the upper slopes (1 x 10^{-3} m^{2}s^{-1}) and near (and sometimes below) molecular levels in the deep basin (1 x 10^{-9} m^{2}s^{-1}). The molecular thermal diffusivity is about 1 x 10^{-7} m^{2}s^{-1}. The low model vertical diffusivities will be discussed in the next section.

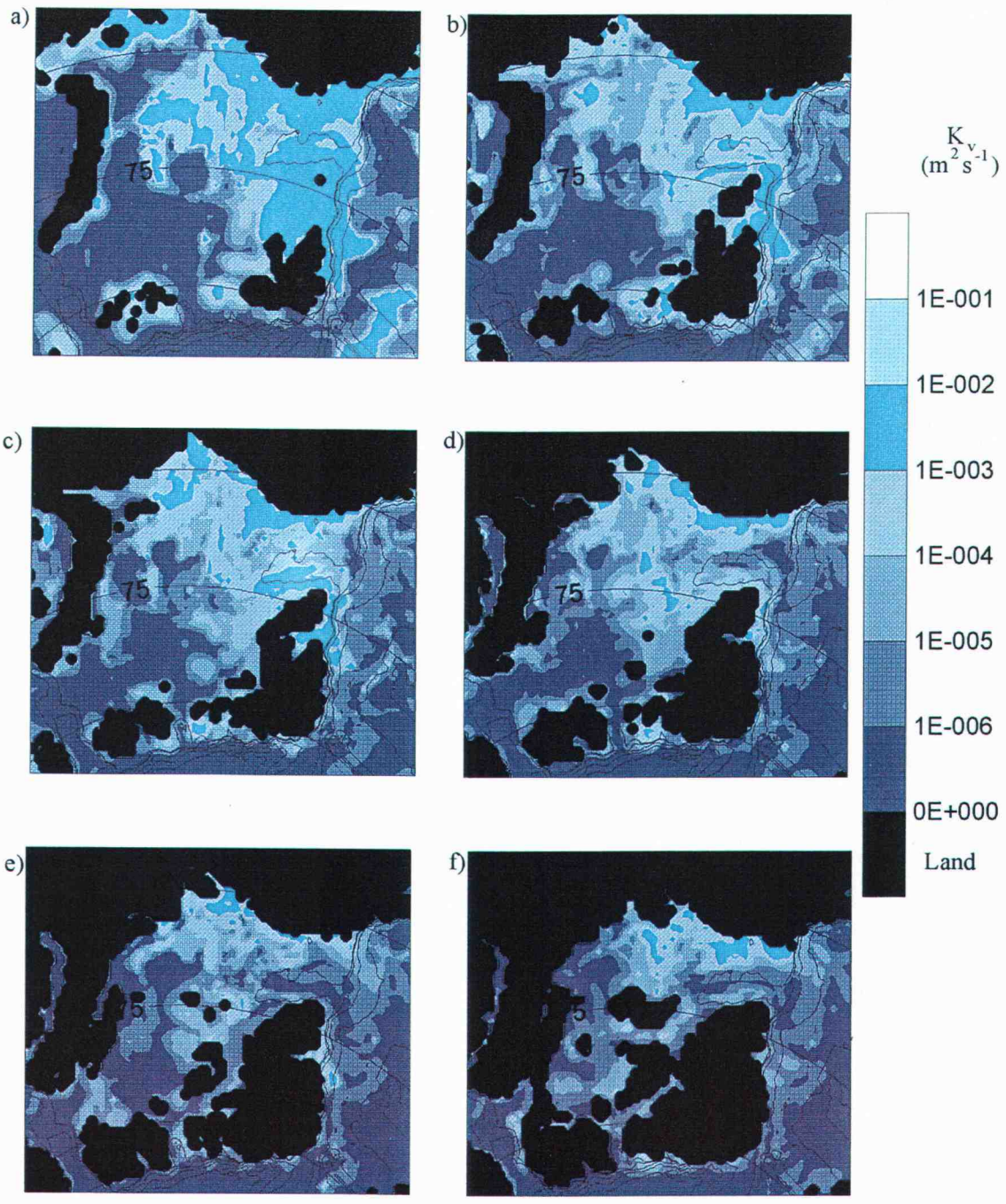

Figure 4.19. Maps of K_v between layers (a)1 and 2, (b) 2 and 3, (c) 3 and 4, (d) 4 and 5, (e) 5 and 6, and (f) 6 and 7.

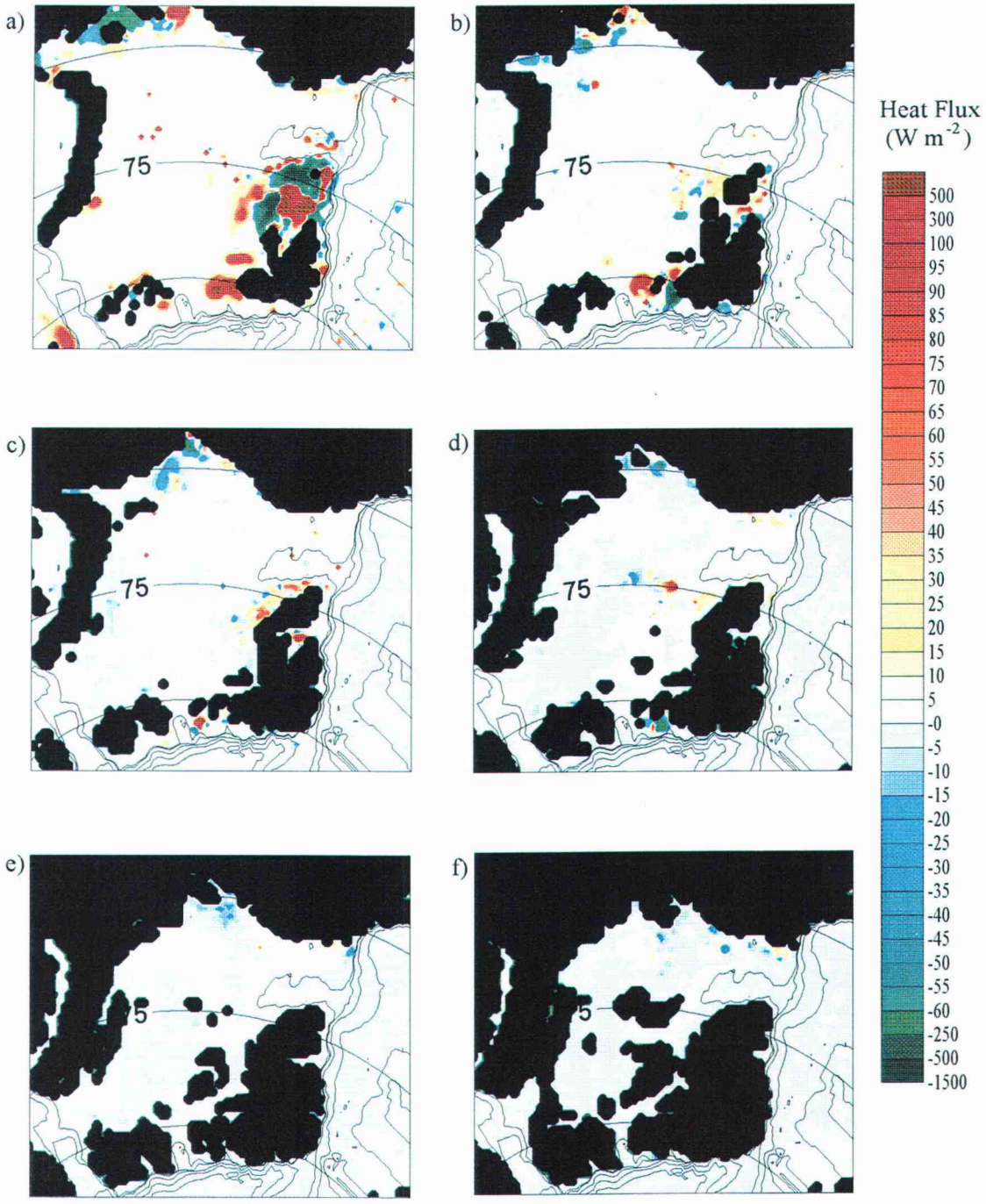

Figure 4.20. Maps of heat flux (W m^{-2}) between layers (a)1 and 2, (b) 2 and 3, (c) 3 and 4, (d) 4 and 5, (e) 5 and 6, and (f) 6 and 7.

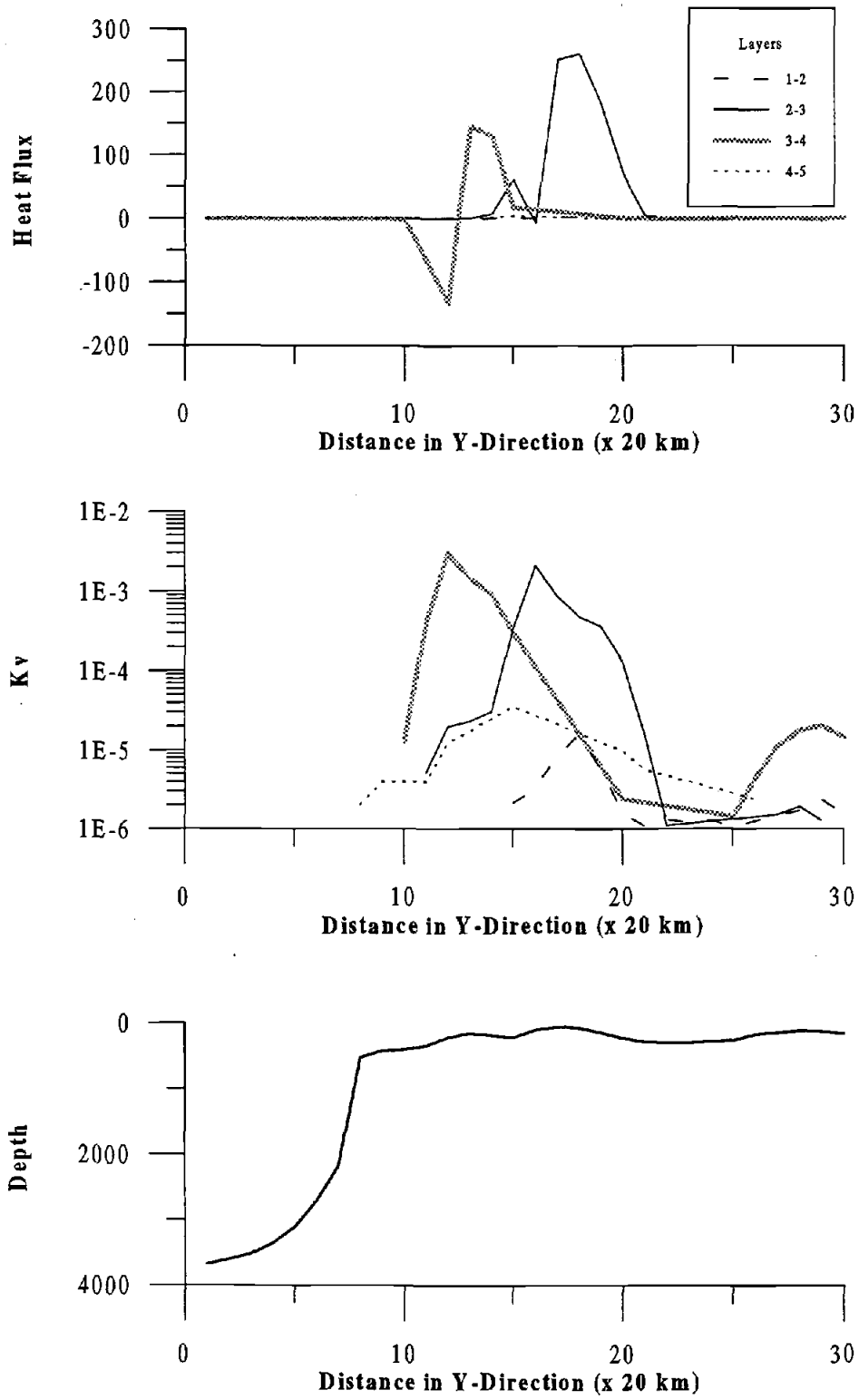

Figure 4.21. Plots of (a) heat flux (W m^{-2}), (b) K_v (m^2s^{-1}), and (c) depth (m) from point A to C in figure 4.16a.

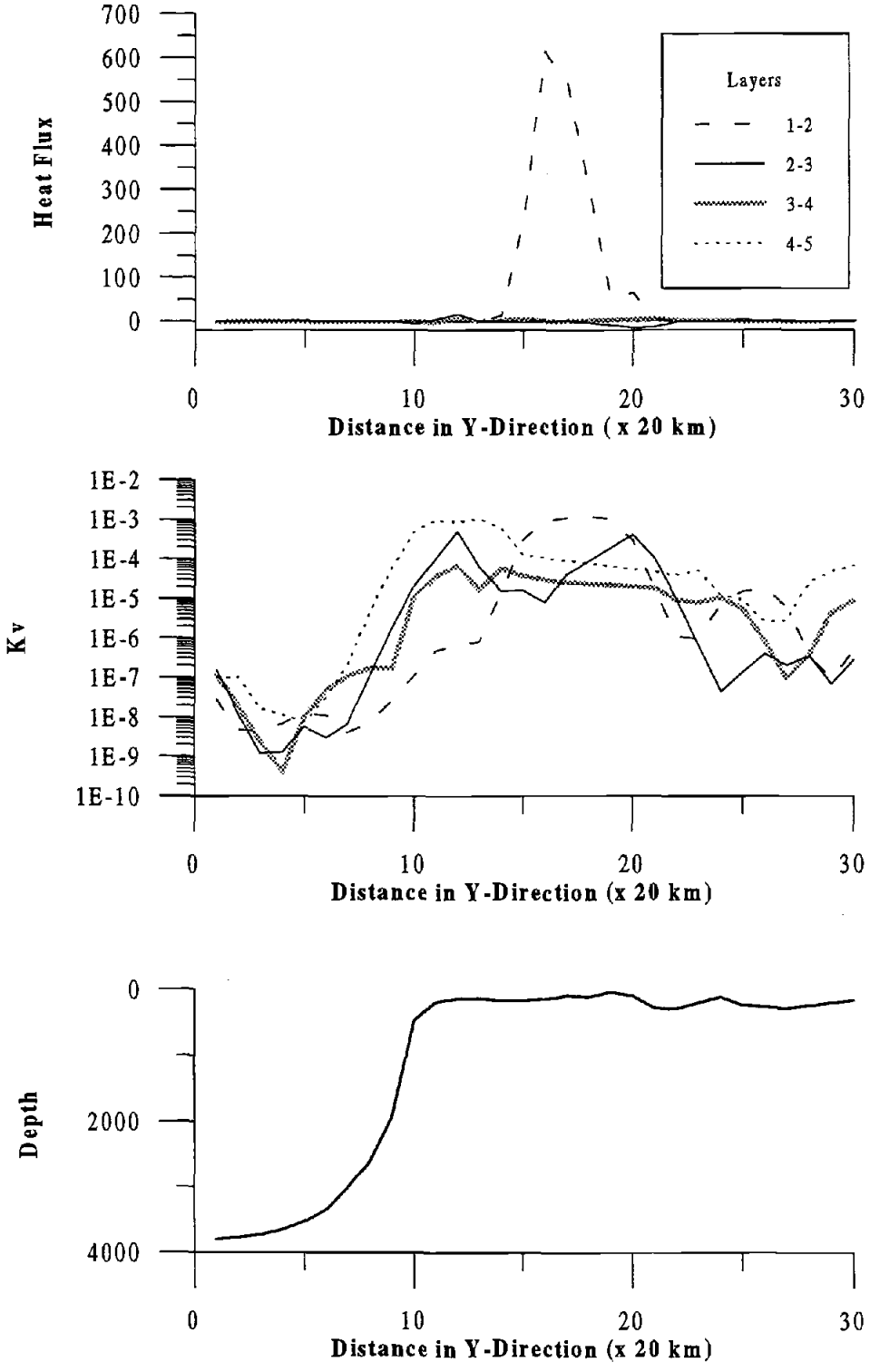

Figure 4.22. Plots of (a) heat flux (W m^{-2}), (b) K_v (m^2s^{-1}), and (c) depth (m) from point D to F in figure 4.16b.

5. DISCUSSION

The analytical models of SS92 and *Baines* [1982], and the numerical model of *Parsons* [1995], indicate that the Barents shelf break region should be an area of strong internal tide generation. To examine the validity of these models, observations are compared to model results; however, the observations were primarily taken around the Yermak Plateau. The SS92 and *Baines* [1982] models can be directly compared to Yermak Plateau measurements; however, the high frequency output from Parsons' model did not include the Yermak Plateau. Because the SS92 and *Baines* [1982] models can be applied to both the Yermak Plateau and the Barents shelf break, we hope that by validating these models with observations made near the Yermak Plateau, we can use these results to help further validate the processes occurring in Parsons' model around the Barents shelf break region. The similarity between the topographical and hydrographic structure of this region and the northern Barents shelf break will partially compensate for the lack of observational data around the latter. The two areas are not identical, however. The tidal constituents between the two regions differ, the Yermak Plateau being dominated by diurnal tides while the Barents shelf break is mainly semi-diurnal (figure 2.7). The shelf break region in the northern Barents Sea is also steeper than the Yermak Plateau and has a shallower shelf which, combined with stronger semi-diurnal tides, is expected to generate more internal tides and therefore increase the mixing rates.

Observations support the idea that the Yermak Plateau is an area of energetic, topographically-generated internal waves, including semidiurnal (near-inertial) waves. Internal waves generated at the seabed will exhibit a downward phase propagation (upward energy propagation) near their generation source. *D'Asaro and Morison* [1992] found upward propagating near-inertial waves in MIZEX 83 data. *Plueddemann* [1992] also found evidence of upward-propagating near-inertial waves. A section of the AEDB velocity time series around the Yermak Plateau is shown in figure 5.1. The internal wave energy level at near-inertial frequencies in this record is significantly greater than over the Nansen Basin. *Plueddemann* [1992] proposed that this increase in near-inertial energy over the Yermak Plateau in AEDB measurements is due to the bottom generation of

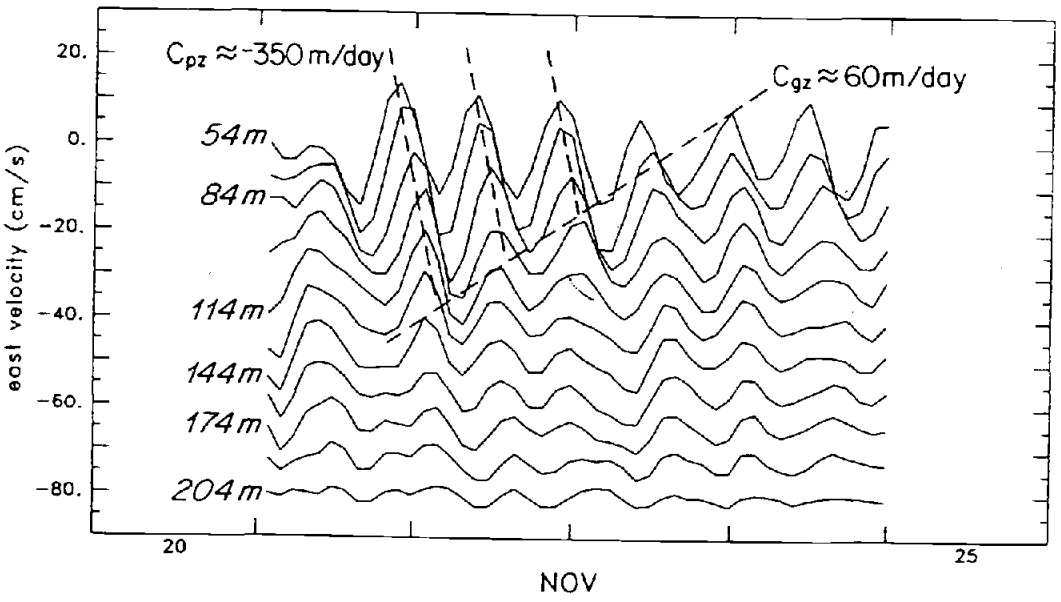

Figure 5.1. Time series of velocity relative to a reference level at 226-m depth for a portion of the Yermak Plateau between November 21 and 24. The uppermost line is at a depth of 54 m. Each successive line is offset by -8 cm s^{-1} and is 15 m deeper (from *Plueddemann* [1992]).

internal tides brought about by the interaction of the barotropic tide with topography, either through scattering from small bottom relief [*Bell*, 1975] or through interaction with large scale topography [*Rattray et al.*, 1969; *Baines*, 1974]. As shown in section 4.3.1, the latter scenario is a likely explanation for these occurrences as well as for occurrences of upward-propagating waves in Parsons' model. From Parsons' model velocity data we see upward-propagating semi-diurnal energy around the shelf break region (figures 4.17c and 4.18c). The results from the analytical models suggest that the upper slope regions are areas of intense internal tide generation and therefore we expect upward-propagating energy there. However, the existence of upward-propagating waves doesn't necessarily mean that the waves are generated at the bottom. Surface generated internal waves will also exhibit the same pattern if they are reflected from the sea-bed. In general, waves can be reflected several times [*New and Pingree*, 1990]. The absence of downward-propagating waves at the shelf break or in the surrounding region in *Parsons'* model [1995] indicate that the waves are not reflected waves, but are generated at the bottom and dissipated in a short horizontal distance (as seen in figures 4.17b and 4.18b).

The problem remains unanswered as to whether the near-inertial waves seen in the observational data around the Yermak Plateau are forced by the M_2 or the S_2 tide (and, potentially, the K_2 and N_2 tides). The non-Eulerian nature of the AEDB and CEAREX "O" camp data precludes resolving the semi-diurnal tidal components since the current meters moved through regions of varying phase and amplitude in the time required to accurately separate the principal components (~15 days). Although the Yermak Plateau is above the critical latitude for the M_2 tide, it is possible that the M_2 internal tide can exist as bottom-trapped or vorticity-trapped mode there. When an internal tide is trapped at the sea-bed, the energy is dissipated close to the bottom. It cannot exist as freely propagating wave, however the M_2 tide still forces energy into the internal wave field. To exist as a vorticity-trapped mode, there must be sufficient negative relative vorticity ($\zeta < 0$) such that the frequency of the M_2 tide is greater than ($\frac{1}{2}\zeta + f$). The M_2 internal tide can then exist as a free wave but is trapped to this region of sufficiently negative relative vorticity [*D'Asaro and Morison*, 1992]. At 82 °N, a negative relative vorticity of 0.00495 cph ($-0.06 f$) is needed to reduce the effective inertial frequency below the frequency of the

M_2 tide (0.0805 cph) [*Plueddemann*, 1992]. *D'Asaro and Morison* [1992] found that the relative vorticity field (-0.15 *f*) in MIZEX 83 measurements was sufficient to allow the existence of freely propagating M_2 internal waves. However, these waves are "trapped" to the region where enough relative vorticity exists to reduce the absolute vorticity ($\frac{1}{2}\zeta + f$) to a frequency below that of the M_2 internal tide. It is important to note that the extremely large negative relative vorticity was seen in a region where a strong current flowed in an anticyclonic direction around a small seamount [*D'Asaro and Morison*, 1992]. We do not generally expect such high relative vorticity fields in other areas. *Plueddemann* [1992] found no evidence for a strong vorticity anomaly in AEDB data. Parsons' model indicates that shear associated with the M_2 tide exists even above the critical latitude; however, in this model, the background relative vorticity is too small for vorticity-trapped modes to occur. Therefore, we assume that the M_2 internal tides occur as bottom-trapped modes in the model. The SS92 and *Baines* [1982] models which include rotation indicate that the S_2 tide alone can generate a significant amount of energy (figure 4.5b and table 4.2). The S_2 tide exists as a freely propagating wave all along the shelf break region. Therefore, one conclusion might be that both components are significant and neither can be disregarded in mixing estimates. The SS92 and *Baines* [1982] models that do not allow for energy flux into the M_2 baroclinic tide north of its critical latitude are under-representing the available velocity shear, and thus energy for mixing in the region. The actual energy flux into internal tides probably lies somewhere in between the two cases. The M_2 barotropic tidal component is the strongest tidal component along the shelf break region and will have the greatest affect on internal tide generation and therefore mixing, even though its affects may be limited very close to its generation site. The trapped nature of the M_2 waves may be a key reason for the large cross-slope variability of mixing seen in both Parsons' model and the CEAREX "O" camp data.

Both the analytical and numerical models have indicated that internal tide generation and associated mixing is strongly aligned with topography. In a short spatial scale, a dramatic difference exists between the deep basin and the shelf break region. To determine the validity of the cross slope variations in mixing predicted by models, we

compare model shears and diffusivities to observations. Shears calculated from AEDB data exhibit cross-slopes variations similar to those calculated from Parsons' model output. Figure 5.2 illustrates the change in shear across the Yermak Plateau calculated from AEDB velocity data. The magnitudes of the AEDB shears were calculated using equation 4.13, where n and m represent consecutive depth bins given in table 3.2. The shear magnitudes were then smoothed using a 48-hour running mean and therefore represent an average shear over several tidal cycles. The averaged magnitude of shears increased from 0.002 s^{-1} to 0.009 s^{-1} as the AEDB drifted from the deep Nansen Basin to the Yermak Plateau. The shears in the data are known to contain not only a semidiurnal signal, but significant higher frequency signals as well [*A. Plueddemann*, pers. comm. 1997]. Parsons' model, with shears almost entirely due to the M_2 tide, contains shear magnitudes as high as AEDB measurements (figure 4.14). Therefore, shears in the Barents shelf break region may be significantly higher than Yermak Plateau values when other tidal and non-tidal components are included.

Diffusivities will be affected by the high shear levels. Several techniques have been employed to estimate the diffusivities around the Yermak Plateau region using velocity and density measurements. *D'Asaro and Morison* [1992], applying the parameterization of *Gregg* [1989] to internal wave shear data from expendable current profilers, found a strong variation of diapycnal diffusivities which closely corresponded to topographic variability. Estimated diapycnal diffusivities ranged from about 1 x 10^{-6} ms^{-2} over the deep Arctic abyssal plains to above 1 x 10^{-4} ms^{-2} over the shallower, rougher topography of the Yermak Plateau. In CEAREX, diffusivity estimates based on microstructure measurements also showed strong variations across the shelf break region [*Padman and Dillon*, 1991]. Shear levels increased as the ice camp drifted over shallower water on the slope of the Yermak Plateau. The highest shear magnitude occurred near the inertial frequency, indicating that the shears could be due to the generation of internal tides. Estimated diffusivities ranged from 2 x 10^{-5} ms^{-2} in deep water to 2 x 10^{-4} ms^{-2} over the central slopes of the Yermak Plateau (figure 5.3). Our conclusion from these observations is that diffusivities exhibit sharp variations with topography in regions where internal tides are generated. Therefore, it is appropriate to use SS92 and Parsons' model to determine

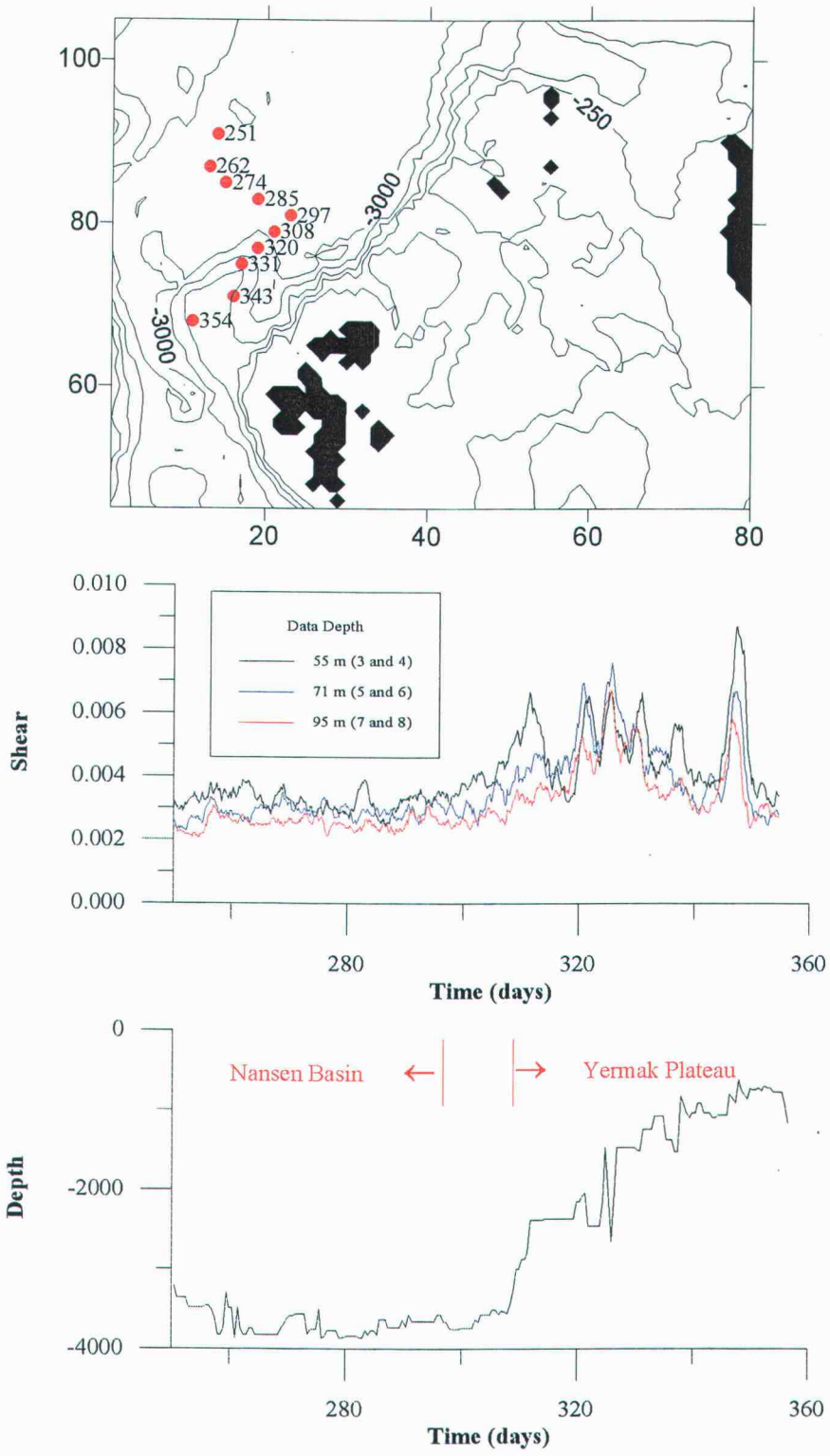

Figure 5.2. (a) Location of AEDB drift track between days 251 and 354. (b) Shear (s^{-1}) between depth bins along drift track. (c) Ocean depth (m) along drift track.

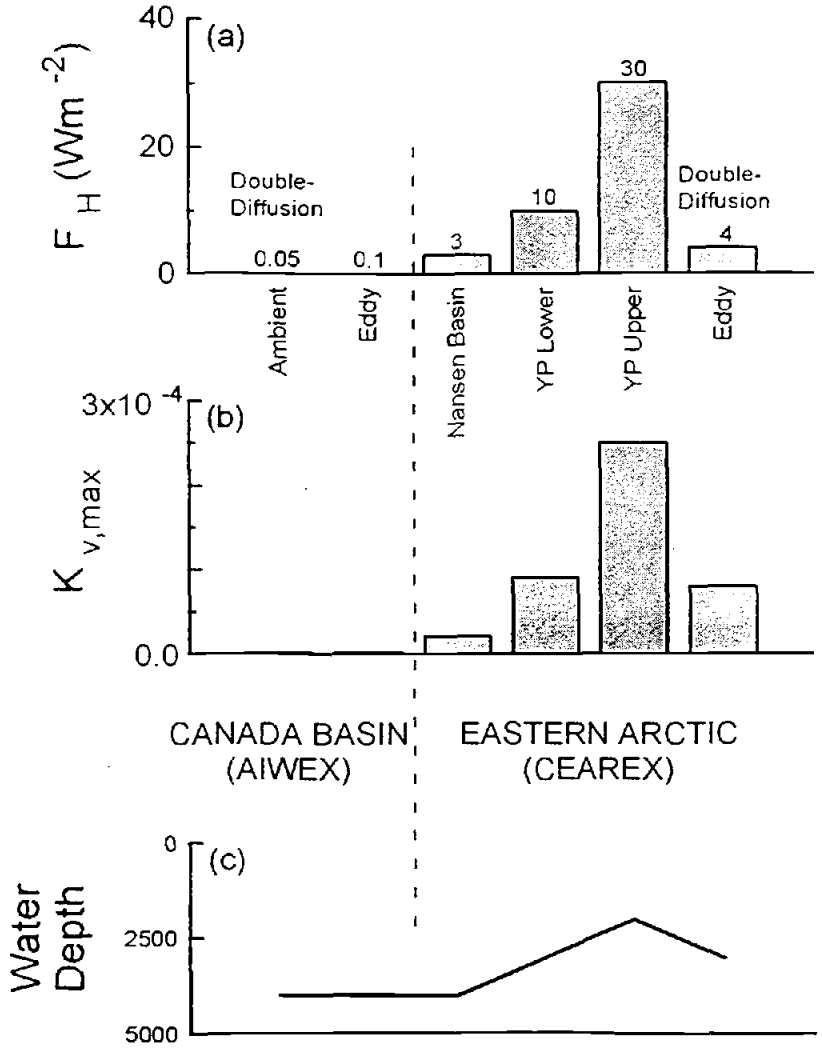

Figure 5.3. Variability of (a) maximum upward heat flux, F_H, from the Atlantic layer and (b) the associated effective vertical diffusivity, $K_{v,max}$. Approximate water depths are shown in (c) (from *Padman* [1995]).

where large variations in diffusivity based on internal tides are expected to occur. Both of these models have indicated that large variations in diffusivity occur around the Barents shelf break (figures 4.19 and 4.7a). Remember that these models only predict diffusivities based on internal tides. Therefore, very low values in the deeper basins are predicted. Other processes, not accounted for by these models, can still produce some mixing throughout the ocean interior.

One problem with diffusivities calculated from the SS92 model is the absence of a wave radiation model. Like SS92, we assume that all the energy put into the internal tides is dissipated within the grid box in which it is generated. With the S_2 tide at least, it is reasonable to assume that the waves might propagate some distance before they are dissipated. The spiky nature of diffusivities and the estimated heat fluxes seen in figures 4.10 and 4.11 is therefore partly an artifact of our method of converting energy fluxes into dissipation. Therefore, a better method for calculating dissipation would include a spatial filter to parameterize wave radiation and laterally smooth the diffusivities.

Diffusivities in Parsons' model were calculated from Richardson number estimates according to equation 4.15. To examine the discrepancy in K_v between model results and observations, the relationship between model vertical diffusivities and Richardson numbers, defined by equation 4.15, is shown in figure 5.4. The relationship between CEAREX vertical diffusivities and Richardson numbers is shown in the same figure. CEAREX diffusivities were estimated from velocity shear microstructure measurements along with conductivity and temperature profiles [*Padman and Dillon*, 1991]. These data, plus ADCP velocity fields, were also used to calculate Richardson numbers [*L. Padman*, personal communication, 1997]. At low Richardson numbers, equation 4.15 closely describes the relationship between Richardson numbers and vertical diffusivities. However, at high Richardson numbers, the parameterization generates much lower values than are found in CEAREX measurements. The initial values for the diffusivity parameterization scheme was deemed appropriate by *Parsons* [1995] because of the large amounts of continental shelves within the model. The shelf break regions, shown in this study to be areas of lower Richardson numbers, are the most important to accurately parameterize when looking at transfer of heat and salt from the Atlantic layer.

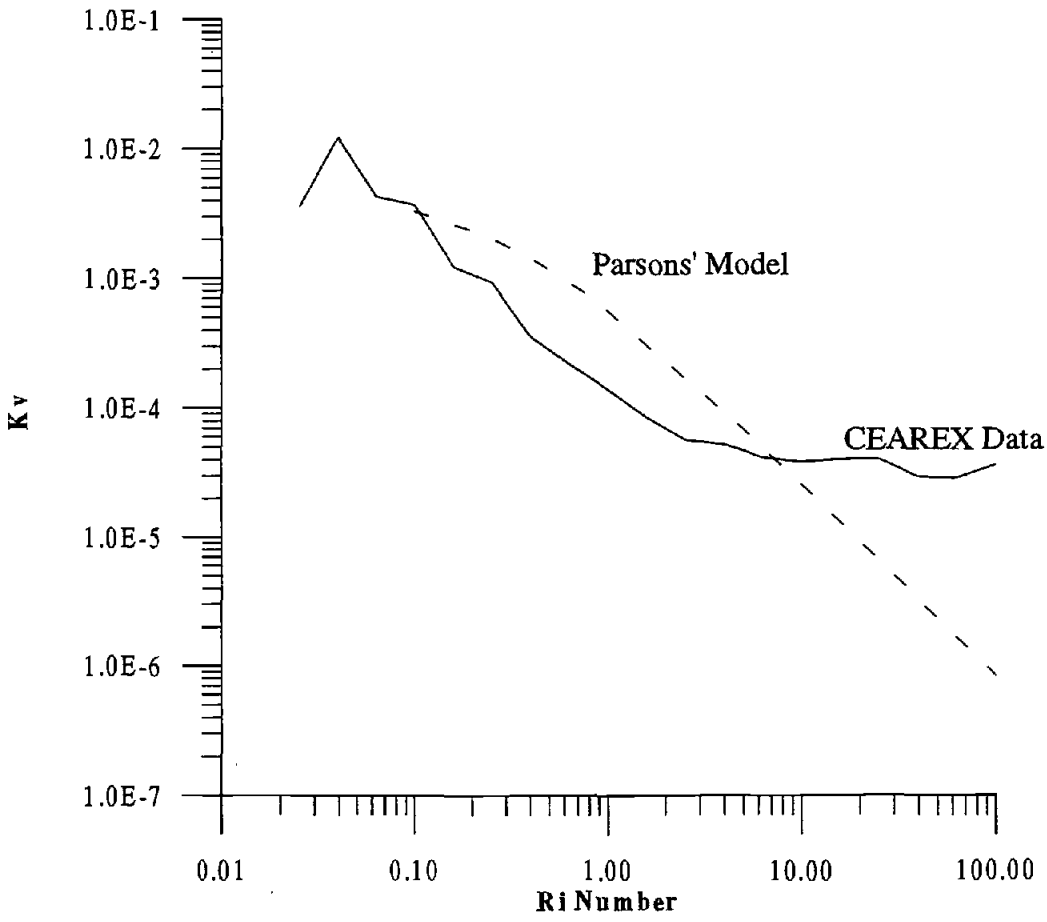

Figure 5.4. The relationship between Richardson number and vertical diffusivity used in Parsons' model (dashed line) and that found from experimental data (solid line) [*Padman*, pers. comm. 1997].

The large variations in diffusivities across the shelf break region predicted by the analytical and numerical models, and validated by the observations, can significantly alter the background circulation in the region via the generation of strong geostrophic velocities. A baroclinic numerical simulation by *Polyakov* [1995] demonstrated how an initial horizontally-homogenous salinity field can be restructured due to spatial variations in tidal mixing. Salinity profiles in slope areas experienced much more mixing than in deeper basins where only weak tidal currents were present (figure 5.5). To examine the possible consequences of such spatially inhomogeneous mixing, a simple model was written to calculate the geostrophic velocities that would develop over time from a typical cross slope variation in K_v as water travels along the northern Barents shelf break from Svalbard towards Franz-Josef Land. The model consisted of two initially identical profiles (figure 2.4) representing a point on the upper slope and a point in the deeper basin near the western edge of northern Barents shelf break. The profile on the upper slope was truncated at 400 m. The two profiles were allowed to diffuse at different rates. For the upper the slope a K_v value of 1×10^{-3} ms^{-2} was used and for the deeper basin a value of 1×10^{-5} ms^{-2} was used. The model was then run for 6 months, a typical transit time of water to flow between Svalbard and Franz-Josef Land (700 km). At each time step, the geostrophic velocity was calculated assuming the points were separated across-slope by 100 km. After 6 months, a geostrophic velocity of 8 cm s^{-1} developed (figure 5.6). Observations in this region [*Aagaard*, 1989] suggest that the alongslope current is approximately 5-15 cm s^{-1} and so is comparable to our simple geostrophic model. The geostrophic velocity created by tide-generated turbulence is significant when compared to the background circulation of ~1-2 cm s^{-1} predicted by coupled ice-ocean general circulation models without tides, such as that of *Häkkinen* and *Mellor* [1992].

The low currents predicted by *Häkkinen* and *Mellor* [1992] model are related to the diffusivity parameterization scheme contained in the model. *Häkkinen* and *Mellor* [1992] use the Princeton Ocean Model (POM) for the ocean component of their coupled model. The POM uses the Mellor-Yamada turbulence closure scheme [*Mellor and Yamada*, 1974, 1982] which determines diffusivity based on the static and dynamic stability of the resolved velocity and hydrographic fields. If a process that produces

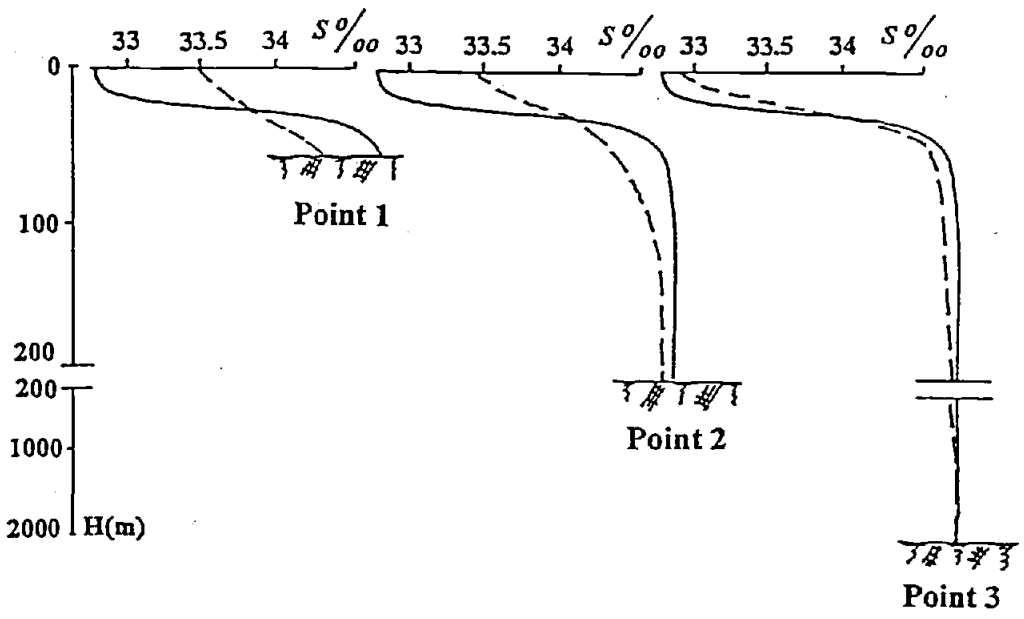

Figure 5.5. Salinity profiles at points at different depths. The solid lines denote the initial salinity profiles, the dashed line represent profiles after model simulation (from *Polyakov* [1995]).

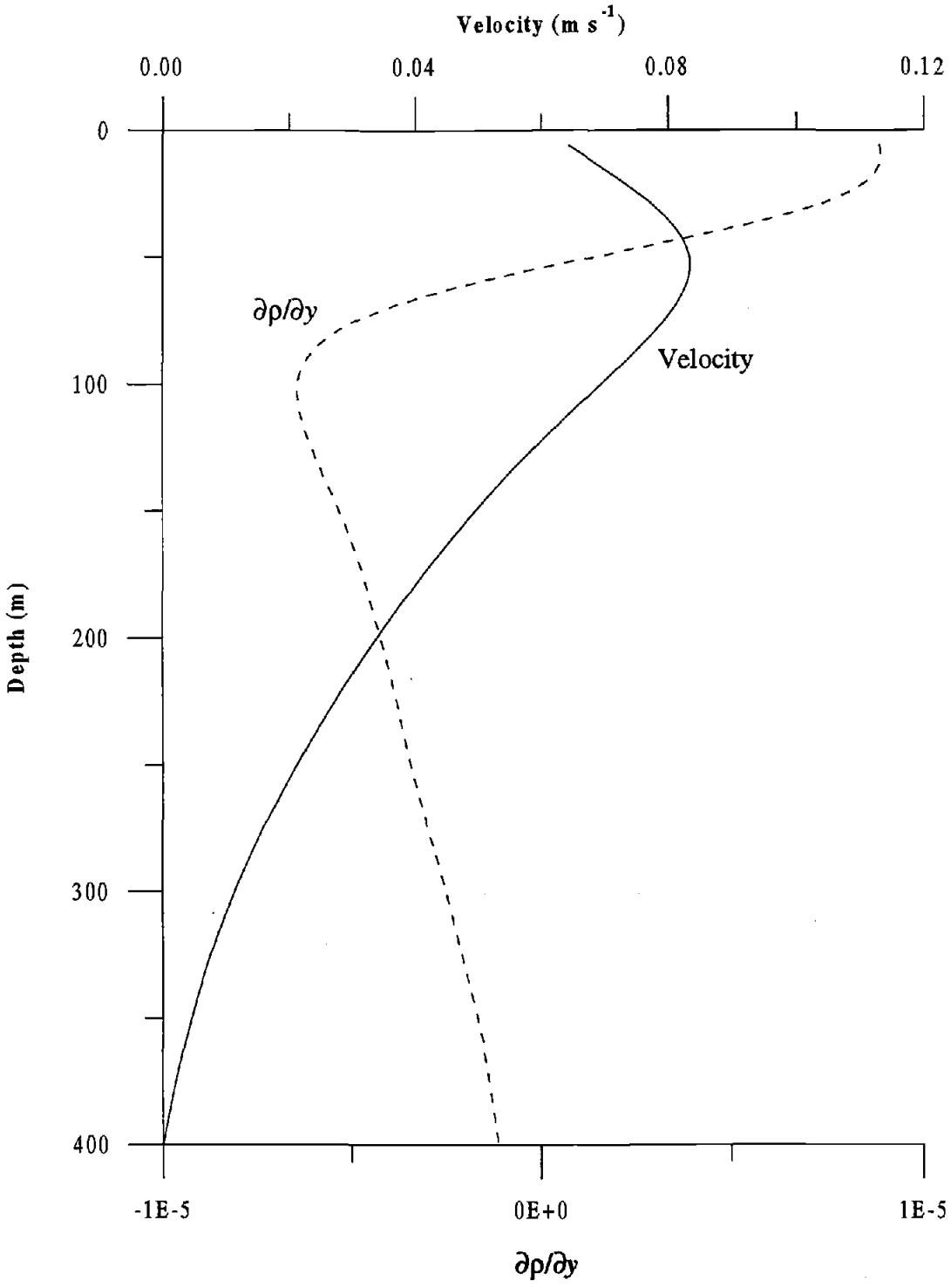

Figure 5.6. Resulting $\partial\rho/\partial y$ and geostrophic velocity after a 6 month model run using an on-slope K_v of 1 x 10^{-3} m^2s^{-1} and an off-slope K_v of 1 x 10^{-5} m^2s^{-1}. The distance separating profiles was 100 km.

mixing, such as internal tides, occurs on smaller scales than the model is able to resolve, the effects of this process will not be accounted for in the model. Therefore, variations in diffusivity that occur at scales smaller than the model resolution will be absent. *Padman* [1995] demonstrated that there was much more variability in K_v from observations than is reproduced in models by this mixing scheme. The absence of tidal forcing in the *Häkkinen* and *Mellor* [1992] model will also limit the modeled current velocities. As was shown in section 4.3, most of the shear in Parsons' model was generated by the M_2 tide (not by the background circulation). Models that neglect tides in this region will predict much lower shears and therefore, using the Richardson number based parameterization, lower diffusivities. The geostrophic addition to the flow which develops due to strong spatial gradients in diffusivities will be absent. The absence of tides combined with the diffusivity parameterization scheme therefore limits the model's ability to reach observed current values.

The large diapycnal diffusivities also imply large heat fluxes. Upward heat fluxes of the order of 100 Wm^{-2} are predicted by both SS92 (no rotation) and Parsons' model along the northern Barents shelf break region (see figures 4.10, 4.11, 4.21, and 4.22). This represents a substantial loss of heat from the Atlantic layer before it ever reaches the Arctic interior. Any attempt at balancing the Arctic heat budget must therefore include the heat loss in this region, and the processes responsible for this loss.

As the AW flows along the Barents shelf break (figure 2.2), upward heat fluxes from the Atlantic Layer could have substantial effects on the ice cover (figure 2.5) in this region. CEAREX measurements showed that the strong diapycnal mixing events over the Yermak Plateau created an upward heat flux of about 20-30 W m^{-2} from the AW. One observed response to this flux was an increase of $(T_{ML} - T_{freeze})$ in the surface layer from about 0.01 °C to 0.04 °C (figure 5.7). As shown in equation 2.31 and discussed in section 2.2.2, the heat flux to the ice cover can be increased by increasing the temperature of the surface mixed layer and/or increasing u_*. This increase in $(T_{ML} - T_{freeze})$, assuming no change in u_*, would increase the heat flux from the surface to sea-ice from 3 to 12 Wm^{-2}. As discussed above, compared to the Yermak Plateau, the Barents shelf break region is probably equally (if not more strongly) influenced by tidal mixing due to internal tides,

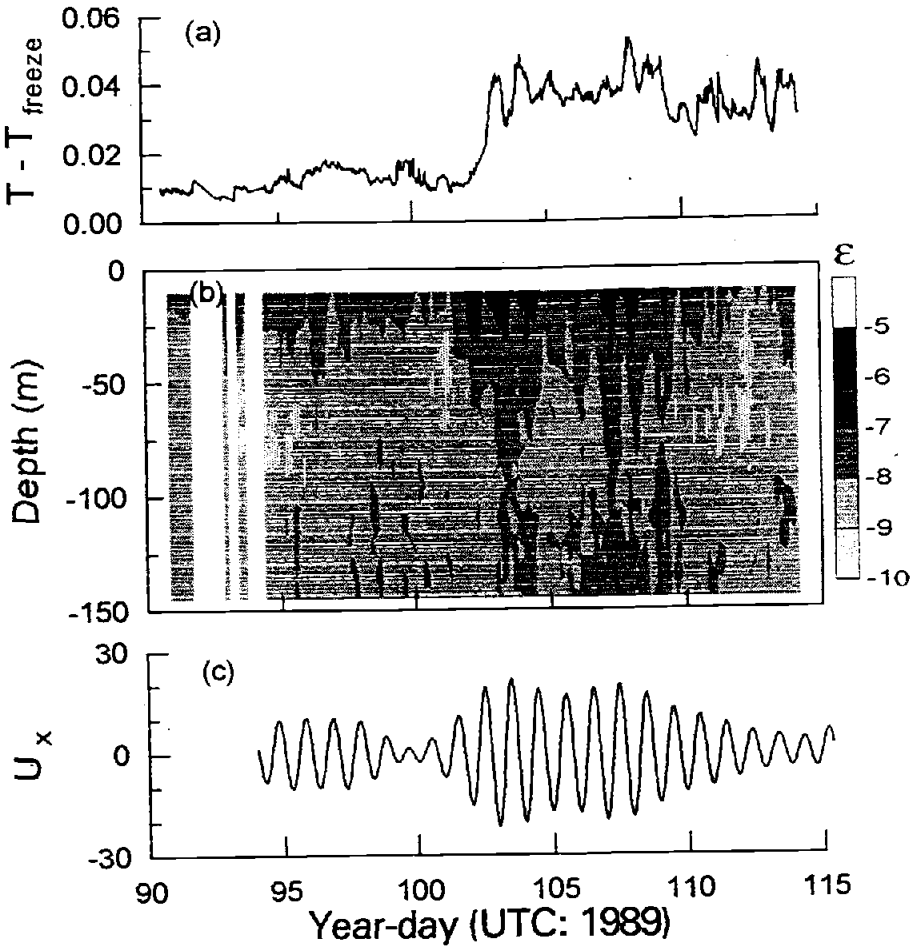

Figure 5.7. Transects of (a) surface mixed layer temperature relative to the freezing point, $T - T_{freeze}$, (b) dissipation rate of turbulent kinetic energy, $\log_{10}\varepsilon$ ($m^2\ s^{-3}$), and (c) cross-slope diurnal tidal current ($cm\ s^{-1}$) at the CEAREX O Camp (from *Padman* [1995], after *Padman and Dillon* [1991]).

which will increase the surface temperature through diapycnal mixing. Shown in figure 2.8, the shelf break region is also a region of stronger tidal currents producing possibly stronger surface stresses which will, therefore, also increase u_*. The Simpson-Hunter calculations, shown in figure 4.1 and discussed in both sections 4.1 and 4.2, also suggest that this region is likely to experience strong mixing from both surface and seabed stresses. Along the Barents shelf break region, the presence of strong diapycnal mixing due to internal tides combined with large surface stresses will increase the heat flux to ice cover.

Buoy data have indicated that multiyear ice is transported along and across the Kara and Barents shelf break region (see figure 2.6) as it flows toward the Fram Strait. The ice, moving at approximately 2 cm s^{-1}, spends about 1 year in this region (figure 2.6). As the ice moves along or across the shelf break region, it could experience substantial melting. In order for an oceanic heat flux (F_w) to melt ice, F_w must exceed the conductive heat flux, Q_C, through the ice to the atmosphere [*Gow and Tucker*, 1990]. On an annual basis, Q_C is about 9 W m^{-2} [*Maykut*, 1985]. Heat flux from the central Arctic Ocean to the ice is about 2 W m^{-2} on an annual basis [*Maykut*, 1985; *Gow and Tucker*, 1990]. The lowest Q_C values (sometimes negative) occur in the summer when the atmospheric temperature is warmest. Assuming a Q_C of 9 W m^{-2}, the net heat flux (heat flux - Q_C) in CEAREX measurements would have jumped from -6 W m^{-2}(indicating freezing) to + 3 Wm^{-2} (indicating melting). We can estimate ice melt rates, w_i, following *Maykut* [1985], using

$$w_i = F_w (\rho_i L_i)^{-1},$$

where ρ_i is the density of ice (~900 kg m^{-3}) and L_i is the heat of fusion, which is about 2.67 x 10^{-5} J kg^{-1} for 7-psu ice at -5 °C. Using a net heat flux of 3 W m^{-2}, w_i is 0.1 cm of ice per day. Over a small spatial scale, therefore, tide-induced mixing was able alter the heat content of the water column enough to shift the ice processes from a freezing regime to a melting one.

If we expect similar heat fluxes along the Barents shelf break, then a substantial amount of fresh water may be added to the water column from ice melt. To estimate

(simply) the fresh water inputs from this process, we assume that a net heat flux of 3 Wm^{-2} occurs along the Barents Sea Shelf break region, which is approximately 100 km wide and 700 km in length. To estimate the volume of fresh water input from melting in this region, we multiply the area (which is assumed to be ice covered) by w_i. Using an area of 7 x 10^{10} m^2 and w_i of 0.1 cm per day, the fresh water input is ~9 x 10^{-4} Sv. Assuming that the ice (approximately 1.5 m thick) is moving at 2 cm s^{-1} along the shelf break region, then 3 x 10^{-3} Sv of ice is transported along this region toward the Fram Strait. Approximately 25% of this ice is, therefore, melted and added to the water column as fresh water. These are only approximate values. The processes involved here are much more complicated than these simple calculations show. Strong seasonal variations exist in the conductive fluxes and ice properties. However, based on these "back-of-the-envelope" calculations, we hypothesize that the upward oceanic heat fluxes produced by tide-induced mixing will significantly modify the oceanic heat content, the hydrographic structure of the water column, and the ice characteristics around the Barents Shelf break.

6. CONCLUSIONS

Using analytical and numerical models, validated with observations, this study has demonstrated that tide-induced mixing is a very important process in the eastern Arctic Ocean. We summarize our principal results below.

1. The barotropic tide, based on the barotropic tidal model of *Kowalik and Proshutinsky* [1994], displays a large amount of spatial variability. Tidal current amplitudes are greatly enhanced around the northern and western Barents Sea shelf break region and in the White Sea. Maximum values in these region are greater than 50 cm s^{-1}. Strong tidal currents lead to large boundary stresses; bottom stress and possibly also surface stress if proper ice conditions are present. Using the Simpson-Hunter parameter [*Simpson and Hunter*, 1974; *Pingree and Griffiths*, 1978], these boundary stresses were determined to be likely to create tidal fronts on the northern Barents shelf break region.

2. The eastern Arctic shelf break region was determined to be an area of strong internal tide generation due to the presence of both strong barotropic tides and steep topography. The SS92 model indicates that the strongest generation of internal tides occurs around the upper slopes of the shelf break. Based on this model, the S_2 barotropic tide can be a significant source of internal tide energy. The internal tide generation model of *Baines* [1982] gives energy fluxes into internal tides similar to those predicted by the SS92 model (with rotation). Evidence for the bottom generation of internal tides at the shelf break region is also found in output from the 3-D baroclinic numerical model of *Parsons* [1995]. Downward-propagating phases near the shelf break region and the lack of upward-propagating phases indicate that these waves are generated at the bottom and are dissipated within a short distance of their generation site. These waves are generated by the M_2 tide, even above the M_2 critical latitude (74° 24' N). Observational evidence from *Plueddemann* [1992] around the Yermak Plateau also indicates that this region is an area of bottom generated near-inertial internal waves. *Padman and Dillon* [1991] found that diurnal tides also interact with topography, producing high frequency waves that appear to be implicated in the occurrence of energetic turbulent mixing events.

3. The combination of boundary mixing and internal mixing created by these tidal processes will have a significant impact on the Arctic environment. Observations from *Padman and Dillon* [1991] and *D'Asaro and Morison* [1992] indicate that strong variations in diffusivities occur in regions where internal tides are generated. These measurements agree with the model results which also predict high diffusivities on the upper slope and lower diffusivities in the deep basin. The strong variation in mixing rates can produce geostrophic currents of several centimeters per second, which are comparable with the alongslope currents measured by *Aagaard* [1989]. Since regions of strong mixing correspond approximately with the dominant pathways of Atlantic Water (as determined by tracing core layer properties), we expect large upward heat fluxes in the shelf break region which will then rapidly reduce the heat content of the Atlantic Layer. These upward heat fluxes may also affect the ice cover in the region. *Padman and Dillon* [1991] observed increased surface layer temperatures as a result of tidal mixing which suggest a significant increase in the transfer of oceanic heat to the ice [*McPhee*, 1992]. If this heat exceeds the loss through the snow cover to the atmosphere, ice will melt. A significant amount of fresh water may be added to the water column by the melting of ice through this process. Thinning of the ice will further alter the ocean to atmosphere heat fluxes.

As indicated by the conclusions above, tidal processes can significantly affect many aspects of the Arctic environment. However, none of the effects will occur in general circulation models if tides are ignored. The inclusion or parameterization of tidal mixing in Arctic Ocean models is therefore critical to accurately modeling the Arctic climate. Our final conclusions, therefore, are as follows.

1. Tides must be included in general circulation models.
2. These models must include the main semi-diurnal and diurnal tidal constituents.
3. Better bathymetry must be incorporated into models for correct topographic generation of waves.

This study was just the first step in understanding the effects of tidal mixing in the eastern Arctic shelf seas. Further work must now be done to more fully understand and quantify these impacts. We conclude that a more sophisticated 3-D baroclinic Arctic

Ocean model is needed to further analyze boundary stresses and internal wave generation on the shelf break region. Process studies near the northern Barents shelf break are also needed to further examine the effects of mixing associated with internal tides in this region. The separation of the S_2 and M_2 baroclinic tidal signals in measurements above the M_2 critical latitude is also important in understanding internal tide dynamics and associated mixing.

REFERENCES

Aagaard, K., A synthesis of the Arctic Ocean circulation, *Rapp. P.-v. Réun. Cons. int. Explor. Mer, 188*, 11-22, 1989.

Aagaard, K., and E. Carmack, The role of sea ice and other fresh water in the Arctic circulation, *J. Geophys. Res., 94,* 14,485-14,498, 1989.

Aagaard, K., and E. Carmack, The Arctic Ocean and climate: a perspective, in *The Polar Oceans and Their Role in Shaping the Global Environment: The Nansen Centennial Volume, Geophys. Monogr. Ser.*, vol. 85, edited by O. Johannessen, R. D. Muench, and J. E. Overland, pp. 137-158, AGU, Washington, D.C., 1994.

Aagaard, K., and L. K. Coachman, Toward an ice-free Arctic Ocean, *EOS, 56,* 484-486, 1975.

Aagaard, K., L. K. Coachman, and E. Carmack, On the halocline of the Arctic Ocean, *Deep Sea Res., 28*, 529-545, 1981.

Aagaard, K., and P. Greisman, Toward new mass and heat budgets for the Arctic Ocean, *J. Geophys. Res., 80,* 3821-3827, 1975.

Altman, D. B., and A. E. Gargett, Differential property transport due to incomplete mixing in a stratified fluid, *Proc. Third Int. Symp. On Stratified Flows*, Pasadena, California Institute of Technology, 1987.

Argote, M. L., A. Amador, M. F. Lavin, and J. R. Hunter, Tidal dissipation and stratification in the Gulf of California, *J. Geophys. Res., 100,* 16,103 - 16,118, 1995.

Baines, P. G., The generation of internal tides by flat bump topography, *Deep Sea Res., 20*, 179 - 205, 1973.

Baines, P. G., On internal tide generation models, *Deep Sea Res., 29*, 307 - 338, 1982.

Bell, T. H., Jr., Topographically generated internal waves in the open ocean, *J. Geophys Res., 80*, 320-327, 1975.

Böning, C. W., and R. G. Budich, Eddy dynamics in a primitive equation model: sensitivity to horizontal resolution and friction, *J. Phys. Oceanogr., 22*, 361-381, 1992.

Bowers, D. G., and J. H. Simpson, Mean position of tidal fronts in European-shelf seas, *Cont. Shelf Res., 7*, 35-44, 1987.

Bowman, M. J., A. C. Kibblewhite, and D. E. Ash, M_2 tidal effects in Greater Cook Strait, New Zealand, *J. Geophys Res., 85*, 2728-2742, 1980.

Boyd, T. J., and E. A. D'Asaro, Cooling in the West Spitsbergen Current: wintertime observations west of Svalbard, *J. Geophys Res., 99*, 22,597-22,618, 1994.

Brooks, D. A., A model study of the buoyancy-driven circulation in the Gulf of Maine, *J. Phys. Oceanogr., 24*, 2387-2412, 1994.

Bryan, K., and M. Cox, An approximate equation of state for numerical models of ocean circulation, *J. Phys. Oceanogr., 2*, 510-514, 1972.

Campbell, W. J., P. Gloersen, and H. J. Zwally, Short- and long-term temporal behavior of polar sea ice covers from satellite passive-microwave observations, in *The Polar Oceans and Their Role in Shaping the Global Environment: The Nansen Centennial Volume, Geophys. Monogr. Ser.*, vol. 85, edited by O. Johannessen, R. D. Muench, and J. E. Overland, pp. 505-520, AGU, Washington, D.C., 1994.

Cartwright, D. E., and B. D. Zetlar, Pelagic tidal constituents, *IAPSO Publication Scientifique No. 33*, Compiled by IAPSO advisory committee on tides and mean sea level, 59 pp., 1985.

Cavalieri, D. J., and S. Martin, The contribution of Alaskan, Siberian, and Canadian coastal polynyas to the cold halocline layer of the Arctic Ocean, *J. Geophys. Res., 99,* 18,343-18,362, 1994.

Cavalieri, D. J., P. Gloerson, and W. J. Campbell, Determination of sea ice parameters with the Nimbus 7 SMMR, *J. Geophys. Res., 89*(C), 5355-5369, 1984.

Comiso, J. C., Characteristics of Arctic winter sea ice from satellite multispectral microwave observations, *J. Geophys. Res., 91*(C1), 975-994, 1986.

Cushman-Roisin, B., *Introduction to Geophysical Fluid Dynamics*, 320 pp., Prentice-Hall, Englewood Cliffs, NJ, 1994.

Czipott, P. V., M. D. Levine, C. A. Paulson, D. Menemenlis, D. M. Farmer, and R. G. Williams, Ice flexure forced by internal wave packets in the Arctic Ocean, *Science, 254*, 832-835, 1991.

D'Asaro, E. A., and J. H. Morison, Internal waves and mixing in the Arctic Ocean, *Deep Sea Res., 39*, S459-S484, 1992.

Emery, W. J., C. Fowler, and J. Maslanik, Arctic sea ice concentrations from special sensor microwave imager and advanced very high resolution radiometer satellite data, *J. Geophys. Res., 99,* 18,329-18,342, 1994.

Endoh, M. C., C. N. K. Mooers, and W. R. Johnson, A coastal upwelling circulation model with eddy viscosity depending upon Richardson Number, in *Coastal Upwelling*, Coastal and Estuarine Sciences, No. 1, edited by F. A. Richards, pp. 203-208, AGU, Washington, D. C., 1981.

Gargett, A. E., and G. Holloway, Sensitivity of the GFDL ocean model to different diffusivities for heat and salt, *J. Phys. Oceanogr., 22* , 1158-1177, 1992.

Garrett, C. J. R., J. R. Keeley, and D. A. Greenberg, Tidal mixing versus thermal stratification in the Bay of Fundy and Gulf of Maine, *Atmosphere-Ocean, 16*, 403-423, 1978.

Gascard J.-C., C. Richez, and C. Rouault, New insights on large-scale oceanography in Fram Strait: the West Spitsbergen Current, in *Arctic Oceanography: Marginal Ice Zones and Continental Shelves*, vol. 49, edited by W. O. Smith and J. M. Grebmeier, pp. 131-182, AGU, Washington, D.C., 1995.

Gill, A. E., *Atmosphere-Ocean Dynamics*, 662 pp., Academic Press, San Diego, Calif., 1982.

Gloersen, P., W. J. Campbell, D. J. Cavalieri, J. C. Comiso, C. L. Parkinson, and H. J. Zwally, *Arctic and Antarctic Sea Ice, 1978-1987: Satellite Passive-Microwave Observations and Analysis*, 290 pp., NASA SP-511, Natl. Aeronaut. and Space Admin., Washington, D. C., 1993.

Gow, A. J., and W. B. Tucker III, Sea ice in the polar regions, in *Polar Oceanography: Part A, Physical Science*, edited by W. O. Smith Jr., pp. 47-122, Academic Press, San Diego, Calif., 1990.

Gregg, M. C., Diapycnal mixing in the thermocline: a review, *J. Geophys. Res., 92*, 5249-5286, 1987.

Gregg, M. C., Scaling turbulent dissipation in the thermocline, *J. Geophys. Res., 94*, 9686-9698, 1989.

Häkkinen, S., and G. L. Mellor, Modeling the seasonal variability of a coupled Arctic ice-ocean system, *J. Geophys. Res., 97*, 20,285-20,304, 1992.

Hanzlick, D., and K. Aagaard, Freshwater and Atlantic Water in the Kara Sea, *J. Geophys. Res., 85*, 4937-4942, 1980.

Hoffman, P. J., Transpolar sea ice drift in the vicinity of the Yermak Plateau as observed by Arctemiz 86 buoys, M.S. thesis, 99 pp., Nav. Postgrad. Sch., Monterey, Calif., 1990.

Hunkins, K., Anomalous diurnal currents on the Yermak Plateau, *J. Mar. Res., 44*, 51-69, 1986.

Huthnance, J. M., Internal tides and waves near the continental shelf edge, *Geophys. Astrophys. Fluid Dynamics, 48*, 81-106, 1989.

Killworth, P. D., D. Stainforth, D. J. Webb, and S. M. Patterson, A free-surface Bryan-Cox-Semtner model, Report No. 270, 163 pp., Institute of Oceanographic Sciences, Deacon Laboratory, Surrey, U. K., 1989.

Kowalik, Z., and A. Y. Proshutinsky, Diurnal tides in the Arctic Ocean, *J. Geophys. Res., 98*, 16,449-16,468, 1993.

Kowalik, Z., and A. Y. Proshutinsky, The Arctic Ocean tides, in *The Polar Oceans and Their Role in Shaping the Global Environment: The Nansen Centennial Volume, Geophys. Monogr. Ser.*, vol. 85, edited by O. Johannessen, R. D. Muench, and J. E. Overland, pp. 137-158, AGU, Washington, D.C., 1994.

Kowalik, Z., and A. Y. Proshutinsky, Topographic enhancement of tidal motion in the western Barents Sea, *J. Geophys. Res., 100*, 2613-2637, 1995.

Kundu, P. K., *Fluid Mechanics*, 638 pp., Academic Press, San Diego, Calif., 1990.

Kunze, E., Near-inertial wave propagation in geostrophic shear, *J. Phys. Oceanogr., 15*, 544-565, 1985.

Lamb, H. H., The climate environment of the Arctic Ocean, in *The Arctic Ocean*, L. Rey, ed., John Wiley & Sons, New York, 135-161, 1982.

LeBlonde, P. H., and L. A. Mysak, *Waves in the Ocean*, 602 pp., Elsevier Ocean Ser. 20, Elsevier, Amsterdam, 1978.

Levitus, S., R. Burgett, and T. Boyer, World Ocean Atlas, 1994: Volume 3, Salinity, NOAA Atlas NESDIS 3, NOAA, Washington, D. C., 1994.

Levitus, S., and T. Boyer, World Ocean Atlas, 1994: Volume 4, Temperature, NOAA Atlas NESDIS 3, NOAA, Washington, D. C., 1994.

Manley, T. O., Branching of Atlantic Water within the Greenland-Spitsbergen passage: an estimate of recirculation, *J. Geophys. Res., 100*, 20,627-20,634, 1995.

Martin, S., and D. J. Cavalieri, Contributions of the Siberian Shelf polynyas to the Arctic Ocean intermediate and deep water, *J. Geophys. Res., 94*, 12,725-12,738, 1989.

Maykut, G. A., Energy exchange over young sea ice in the central Arctic, *J. Geophys Res., 83*, 3646-3658, 1978.

Maykut, G. A., An introduction to ice in the polar oceans, *Tech. Rep. APL-UW 8510*, Applied Physics Lab, University of Washington, Seattle, 1985.

McPhee, M. G., Turbulent heat flux in the upper ocean under sea ice, *J. Geophys Res., 97*, 5365-5379, 1992.

McPhee, M. G., and D. G. Martinson, Turbulent mixing under the drifting ice pack in the Weddell Sea, *Science, 263*, 218-221, 1994.

Mellor, G. L., and S. Häkkinen, A review of coupled ice-ocean models, in *The Polar Oceans and Their Role in Shaping the Global Environment: The Nansen Centennial Volume, Geophys. Monogr. Ser.*, vol. 85, edited by O. Johannessen, R. D. Muench, and J. E. Overland, pp. 137-158, AGU, Washington, D.C., 1994.

Mellor, G. L., and T. Yamada, A hierarchy of turbulence closer models for planetary boundary layers, *J. Atmos. Sci., 31*, 1791-1806, 1974.

Mellor, G. L., and T. Yamada, Development of a turbulence closure model for geophysical fluid problems, *Rev. Geophys., 20*, 851-875, 1982.

Muench, R. D., M. G. McPhee, C. A. Paulson, and J. H. Morison, Winter oceanographic conditions in the Fram Strait-Yermak Plateau region, *J. Geophys. Res., 97*, 3469-3483, 1992.

Munk, W., Internal waves and small-scale processes, *Evolution of Physical Oceanography*, B. Warren and C. Wunsch, Eds., The MIT Press, 623 pp., 1981.

Munk, W. H., and E. R. Anderson, Notes on the theory of the thermocline, *J. Mar. Res., 7*, 276-295, 1948.

Nakamura, N., and A. H. Oort, Atmospheric heat budgets of the polar regions, *J. Geophys Res., 93*, 9510-9524, 1988.

New, A. L., and R. D. Pingree, Large-amplitude internal soliton packets in the central Bay of Biscay, *Deep Sea Res., 37*, 513-524, 1990.

Oakey, N. S., Determination of the rate of dissipation of turbulent energy from simultaneous temperature and velocity shear microstructure measurements, *J. Phys. Oceanogr., 12*, 256-271, 1982.

Orlanski, I., and K. Bryan, Formation of the thermohaline step structure by large-amplitude internal gravity waves, *J. Geophys. Res., 74,* 6975-6983, 1969.

Osborn, T. R., Estimates of the local rate of vertical diffusion from dissipation measurements, *J. Phys. Oceanogr., 10*, 83-89, 1980.

Padman, L., Small-scale physical processes in the Arctic Ocean, in *Arctic Oceanography: Marginal Ice Zones and Continental Shelves*, vol. 49, edited by W. O. Smith and J. M. Grebmeier, pp. 97-129, AGU, Washington, D.C., 1995.

Padman, L., and T. M. Dillon, Turbulent mixing near the Yermak Plateau during the Coordinated Eastern Arctic Experiment, *J. Geophys. Res., 96,* 4769-4782, 1991.

Padman, L., T. M. Dillon, H. W. Wijesekera, M. D. Levine, C. A. Paulson, and R. Pinkel, Internal wave dissipation in a non-Garrett-Munk ocean, *Proceedings of the 'Aha Huliko'a Hawaiian Winter Workshop*, University of Hawaii at Manoa, Honolulu, 1991.

Padman, L., A. J. Plueddemann, R. D. Muench, and R. Pinkel, Diurnal tides near the Yermak Plateau, *J. Geophys. Res., 97,* 12,639-12,652, 1992.

Parkinson, C. L., J. C. Comiso, H. J. Zwally, D. J. Cavalieri, P. Gloersen, and W. J. Campbell, *Arctic Sea Ice, 1973-1976: Satellite Passive-Microwave Observations*, 296 pp., NASA SP-489, Natl. Aeronaut. and Space Admin., Washington, D. C., 1987.

Parsons, A. R., On the Barents Sea Polar Front in summer and the interpretations of the associated regional oceanography using an Arctic Ocean general circulation model, Ph.D. dissertation, 178 pp., Nav. Postgrad. Sch., Monterey, Calif., 1995.

Parsons, A. R., R. H. Burke, R. D. Muench, C. Chiu, J. F. Lynch, J. H. Miller, A. J. Plueddemann, and R. Pawlowicz, The Barents Sea Polar Front in summer, *J. Geophys. Res., 101,* 14,201-14,221, 1996.

Perkins, R.G., and E. L. Lewis, Mixing in the West Spitsbergen Current, *J. Phys. Oceanogr., 14*, 1315-1325, 1984.

Pfirman, S. L., D. Bauch, and T. Gammelsrod, The northern Barents Sea: water mass distribution and modification, in *The Polar Oceans and Their Role in Shaping the Global Environment: The Nansen Centenial Volume, Geophys. Monogr. Ser.*, vol. 85, edited by O. Johannessen, R. D. Muench, and J. E. Overland, pp. 137-158, AGU, Washington, D.C., 1994.

Pingree, R. D., and D. K. Griffiths, Tidal fronts on the shelf seas around the British Isles, *J. Geophys. Res., 83,* 4615-4622, 1978.

Pingree, R. D., P. M. Holligan, and G. T. Mardell, The effect of vertical stability on phytoplankton distributions in the summer on the northwest European shelf, *Deep Sea Res., 32A,* 929-947, 1978.

Plueddemann, A. J., Internal wave observations from the Arctic Environmental Drifting Buoy, *J. Geophys. Res., 97,* 12,619-12,638, 1992.

Polyakov, I. V., Maintenance of the Arctic Ocean large-scale baroclinic structure by the M_2 tide, *Polar Research, 13(2),* 219-232, 1995.

Pond, S., and G. L. Pickard, *Introduction to Dynamical Oceanography,* 329 pp., Pergamon Press, Headington Hill Hall, Oxford, 1983.

Prazuck, C., Anomalous diurnal currents in the vicinity of the Yermak Plateau, Ph.D. dissertation, 125 pp., Nav. Postgrad. Sch., Monterey, Calif., 1991.

Proshutinsky, A. Y., and M. A. Johnson, Two circulation regimes of the wind-driven Arctic Ocean, *J. Geophys. Res., 102,* 12.493-12,514, 1997.

Rattray, M., On the coastal generation of internal tides, *Tellus, 22,* 54-62, 1960.

Rothrock, D. A., The mechanical behavior of pack ice, *Annual Review of Earth Planetary Sciences, 3,* 317-342, 1975.

Rudels, B., E. P. Jones, L. G. Anderson, and G. Kattner, On the intermediate depth waters of the Arctic Ocean, in *The Polar Oceans and Their Role in Shaping the Global Environment: The Nansen Centennial Volume, Geophys. Monogr. Ser.,* vol. 85, edited by O. Johannessen, R. D. Muench, and J. E. Overland, pp. 137-158, AGU, Washington, D.C., 1994.

Schumacher, J. D., T. H. Kinder, D. J. Pashinski, and R. L. Charnell, A structural front over the continental shelf of the eastern Bering Sea, *J. Phys. Oceanogr., 9* , 79 - 87, 1979.

Schwiderski, E. W., *Global Ocean Tides, Part II: The Semidiurnal Principal Lunar Tide (M_2), Atlas of Tidal Charts and Maps,* Naval Surface Weapon Center, Dahlgren, VI 22248, 87 pp., 1979.

Schwiderski, E. W., *Global Ocean Tides, Part III: The Semidiurnal Principal Solar Tide (S_2), Atlas of Tidal Charts and Maps,* Naval Surface Weapon Center, Dahlgren, VI 22248, 96 pp., 1981a.

Schwiderski, E. W., *Global Ocean Tides, Part IV: The Diurnal Luni-Solar Declination Tide (K_1), Atlas of Tidal Charts and Maps,* Naval Surface Weapon Center, Dahlgren, VI 22248, 87 pp., 1981b.

Schwiderski, E. W., *Global Ocean Tides, Part V: The Diurnal Principal Lunar Tide (O_1), Atlas of Tidal Charts and Maps,* Naval Surface Weapon Center, Dahlgren, VI 22248, 85 pp., 1981c.

Semtner, A. J., An oceanic general circulation model with bottom topography, Tech. Rep. 9, 90 pp., Dept. of Meterol., Univ. of Calif., Los Angeles, 1974.

Semtner A. J., And R. M. Chervin, A simulation of the global ocean circulation with resolved eddies, *J. Geophys. Res., 93,* 15,502-15,522, 15,767-15,775, 1988.

Simpson, J. H., and J. R. Hunter, Fronts in the Irish Sea, *Nature, 260,* 404-406, 1974.

Simpson, J. H., C. M. Allen, and N. C. G. Morris, Fronts on the continental shelf, *J. Geophys. Res., 83,* 4607-4614, 1978.

Simpson, J. H., and D. Bowers, Models of stratification and frontal movement in shelf seas, *Deep Sea Res., 28A,* 727-738, 1981.

Sjöberg, B., and A. Stigebrandt, Computations of the geographical distribution of the energy flux to mixing processes via internal tides and the associated vertical circulation in the ocean, *Deep Sea Res., 39,* 269-291, 1992.

Smith, S. D., R. D. Muench, and C. H. Pease, Polynyas and Leads: an overview of physical processes and environment, *J. Geophys. Res., 95,* 9461-9479, 1990.

Steele, M., J. H. Morison, and T. B. Curtin, Halocline water formation in the Barents Sea, *J. Geophys. Res., 100,* 881-894, 1995.

Steffen, K., J. Key, D. J. Cavalieri, J. Comiso, P. Gloersen, K. St. Germain, and I. Rubenstein, The estimation of geophysical parameters using passive microwave algorithms, in *Microwave Remote Sensing of Sea Ice, Geophys. Monogr. Ser.*, vol. 68, edited by F.D. Carsey, pp 201-231, AGU, Washington, D.C., 1992.

Steffen, K., and A. Schweiger, NASA Team Algorithm for sea ice retrieval from Defense Meteorological Satellite Program Special Sensor Microwave Imager: comparison with Landsat satellite imagery, *J. Geophys. Res., 96,* 21,971-21,987, 1991.

Stigebrandt, A., Some aspects of tidal interaction with fjord constriction, *Estuarine and Coastal Marine Science, 11,* 151-166, 1980.

Tennekes, H., and J. L. Lumley, *A First Course in Turbulence*, 300 pp., MIT press, Cambridge, Mass., 1992.

Turner, J. S., *Buoyancy Effects in Fluids*, 368 pp., Cambridge University Press, New York, 1973.

Walsh, J. E., and C. M. Johnson, An analysis of Arctic sea ice fluctuations, 1957-77, *J. Phys. Oceanogr., 9,* 580-591, 1979.

Wunsch, C., Internal tides in the ocean, *Rev. Geophys. and Space Phys., 13*, 167-182, 1975.

Zahel, W., A global hydrodynamic-numerical 1°-model of the ocean tides; the oscillation system of the M_2-tide and its distribution of energy dissipation, *Ann. Geophys., 33*, 31-40, 1977.

APPENDIX

APPENDIX. ELECTRONIC DATA ACCESS

Web Sites:

For additional information regarding selected topics, see web sites below:

Ice Motion Image: http://iabp.apl.washington.edu/isochrone.gif

Model Information:

Kowalik and Proshutinsky [1994]: http://www.ims.alaska.edu:8000/tide.html

Parsons [1995]: http://vislab-www.nps.navy.mil/~braccio/maslowski/arctic.html

SSMI Data: http://www-nsidc.colorado.edu

Ftp Sites

Data was obtained from the following anonymous ftp sites:

Arctic Bathymetry: summit.ims.alaska.edu

Output from the model of *Kowalik and Proshutinsky* [1995]: summit.ims.alaska.edu

SSMI ice concentration data: sidads.colorado.edu